

**A NAVIGATION SYSTEM FOR FREE DESCENT-ASCENT
AUTONOMOUS UNDERWATER VEHICLES**

By

Jesús R. Torrado Díaz

A thesis submitted in partial fulfillment of the requirements for the degree of

MASTER OF SCIENCE

in

COMPUTER ENGINEERING

UNIVERSITY OF PUERTO RICO
MAYAGÜEZ CAMPUS

May, 2017

Approved by:

Manuel Jiménez, Ph.D.
Chairman, Graduate Committee

Date

Wilford Schmidt, Ph.D.
Member, Graduate Committee

Date

Domingo Rodríguez, Ph.D.
Member, Graduate Committee

Date

Ismael Pagán Trinidad, M.S.
Graduate Studies Representative

Date

José Colom, Ph.D.
Department Chairperson

Date

Abstract of Thesis Presented to the Graduate School
of the University of Puerto Rico in Partial Fulfillment of the
Requirements for the Degree of Master of Science

**A NAVIGATION SYSTEM FOR FREE DESCENT-ASCENT
AUTONOMOUS UNDERWATER VEHICLES**

By

Jesús R. Torrado Díaz

May 2017

Chair: Dr. Manuel Jiménez

Department: Electrical and Computer Engineering Department

Free vehicles are buoyant platforms designed to freely descend through the water column when ballasted. A free vehicle gathers samples from the water column or the ocean bed. Once done sampling, the vehicle releases its ballast, surfaces, and signals for recovery. Free vehicles are flexible, low cost, tools for marine research and are designed with an interchangeable payload and full ocean depth deployment capability. This thesis presents the development of a post-processing navigation system based on geomagnetic navigation algorithms, suitable for free vehicles. A navigation solution for free vehicles can facilitate research efforts, by enabling the correlation of the samples gathered, to its location. Traditional underwater navigation solutions based on sonar technology can hinder a free vehicle's payload capabilities or introduce prohibitive costs. Geomagnetic navigation is a technique that uses magnetic maps and a strap down compass to determine a vehicle's position. The technique works by correlating the vehicle's path and corresponding magnetic readings to a magnetic map. The developed system was tested and its navigation performance estimated by a simulation framework developed for this purpose. The simulation framework consists of sensor model, a trajectory generator and performance measurements. The

developed navigation system demonstrated good potential as a navigation solution and its recommended configuration and sensor performance is presented.

Resumen de tesis presentado a la Escuela Graduada
de la Universidad de Puerto Rico como requisito parcial de los
requerimientos para el grado de Maestría en Ciencias

UN SISTEMA DE NAVEGACIÓN PARA VEHÍCULOS DE CAÍDA Y ACENSO LIBRE

Por

Jesús R. Torrado Díaz

mayo 2017

Consejero: Dr. Manuel Jiménez

Departamento: Ingeniería Eléctrica y Computadoras

Los vehículos de descenso y acenso libre son plataformas flotantes diseñadas para descender libremente través de la columna de agua cuando son lastrados. Un vehículo de descenso y acenso libre recoge muestras de la columna de agua o del suelo oceánico. Una vez hecho el muestreo, el vehículo libera su lastre, sube a la superficie y envía señales para su recuperación. Estos vehículos son herramientas flexibles, de bajo costo, para la investigación marina y están diseñados con una carga de sensores intercambiable y la capacidad de llegar a los océanos más profundos. Esta tesis presenta el desarrollo de un sistema de navegación de post-procesamiento basado en algoritmos de navegación geomagnética, apto para vehículos de descenso y acenso libre. Una solución de navegación para estos vehículos puede facilitar los esfuerzos de investigación, permitiendo la capacidad de asociar una muestra con la localización donde fue tomada. Las soluciones tradicionales de navegación submarinas basadas en la tecnología sonar pueden limitar las capacidades de llevar carga útil de un de un vehículo de descenso y caída libre o introducir costos prohibitivos. La navegación geomagnética es una técnica que usa mapas de contornos magnéticos, y una compas para determinar la posición de un vehículo. La técnica funciona correlacionando la trayectoria del vehículo y lecturas magnéticas correspondientes a un mapa magnético.

El sistema desarrollado fue probado y su desempeño de navegación estimado por un marco de simulación desarrollado para este propósito. El marco de simulación consiste de modelos de sensores, un generador de trayectoria y medidas de rendimiento. El sistema de navegación desarrollado demostró un buen potencial como solución de navegación y su configuración recomendada y su rendimiento esperado se presenta.

Contents

List of Abbreviations	ix
1 Introduction	1
2 Theoretical Background	4
2.1 Strap-Down Inertial Navigation	4
2.1.1 Coordinate Frames	5
2.1.2 Subscripts and Superscripts	5
2.1.3 Inertial Measurement Unit (IMU)	6
2.1.4 Attitude Equations	7
2.1.5 Motion Equations	10
2.1.6 INS Limitations	11
2.1.7 INS Aiding	15
2.2 AUV Depth Estimate	15
2.2.1 Total Pressure Field	16
2.2.2 Pressure Sensor Model	17
2.2.3 Pressure Measurement Model	18
2.3 Geomagnetic Navigation	18
2.3.1 Earth's Magnetic Field	20
2.3.2 Magnetometer	21
2.3.3 Geomagnetic Navigation Algorithms	23
3 Previous Work: AUV INS Aiding	25
3.0.1 Acoustic Time-of-Flight Navigation	25
3.0.2 Doppler Navigation	27
3.0.3 Geophysical Navigation	28

3.0.4	Model-Aided Inertial Navigation	38
3.1	Inertial Navigation Aiding Scheme Summary	41
4	Problem Statement & Hypothesis	44
5	Objectives	45
5.1	General Objectives	45
5.2	Specific Objectives	45
6	Methodology	46
6.1	System Overview	46
6.2	Trajectory Generator	47
6.3	Sensor Models	52
6.4	Inertial Navigation Computer	53
6.4.1	Inertial Attitude Computer	53
6.4.2	Inertial Position Computer	54
6.5	Magnetic Computer	55
6.6	State Estimators	55
6.6.1	Attitude Estimator	55
6.6.2	Position Estimator	62
6.7	Experimental Setup	76
6.7.1	Attitude Complementary Filter Test Setup	76
6.7.2	Horizontal Position Particle Filter Test Setup	79
6.7.3	Depth Particle Filter Tests Setup	80
7	Results and Analysis	81
7.1	Attitude Complementary Filter Test	81
7.1.1	Attitude Complementary Filter Tests With Simulated Data Sets	81
7.2	Horizontal Position Particle Filter (HPPF) Tests	93
7.2.1	HPPF Tests With Simulated Data Sets	93

7.3	Depth Particle Filter Tests	112
7.3.1	DPF Test With Simulated Data	112
7.4	Creation of a Physically Constraint Model	120
7.4.1	PCM Development	120
7.4.2	HPPF Test with Simulated Data	127
7.4.3	HPPF Results and Analysis of Field Data	135
7.4.4	PCM Summary	143
7.5	Results and Analysis Summary	145
8	Conclusions and Future Work	147
8.1	Conclusions	147
8.2	Future Work	148
9	Contributions	149
	Bibliography	150

List of Abbreviations

ADCM	Acoustic Doppler Current Meter
AUV	Autonomous Underwater Vehicle
DPF	Depth Particle Filter
DCM	Direction Cosine Matrix
DCT	Downward Continuation Techniques
EMAG2	Earth Magnetic Anomaly Grid (2-arc minute resolution)
FV	Free Vehicle
EMF	Earth Magnetic Field
ESS	Expected Sample Size
FOGMA	First-Order Gauss-Markov Acceleration model
FOGMP	First-Order Gauss-Markov Process
GC	Geomagnetic Computer
HPPF	Horizontal Position Particle Filter
IMU	Inertial Measurement Unit
INC	Inertial Navigation Computer
INS	Inertial Navigation System
PFM	Physical Constraint Model
UPRM	University of Puerto Rico at Mayagüez

Chapter 1

Introduction

Untethered free-descent/ascent vehicles (free vehicles) are buoyant platforms designed to freely descend through the water column when sufficiently ballasted. Internal instruments and external scientific payload sample at regular intervals and the ballast is released by internal logic triggering of burn-wires, or by external galvanic releases. Upon surfacing, they signal a vessel or ground station for retrieval and are recovered by surface ships. Designed with an interchangeable payload and full ocean depth deployment capability, free vehicles are flexible tools for marine research.

A navigation system suitable for free vehicles can facilitate research efforts by enabling the correlation of the samples gathered, to the location where they were taken. Traditional solutions like GPS signals cannot penetrate the ocean's surface and navigation solutions based on sonar technology hinder the free vehicle's payload capabilities, require periodic positioned reference and introduce prohibitive costs. Inertial Navigation Systems (INS) are self-contained navigation solutions that use strap down accelerometer and gyroscopes with dead reckoning techniques to provide estimates of position, parting from a given initial position and initial velocity. Ideal INS systems provide error free trajectory estimates, however, inherent sensor noise and other non-ideal characteristics cause estimation errors that grow unbounded with time. INSs require an external navigation reference to limit their error propagation. Geomagnetic navigation is a technique that uses magnetic maps, strap down compass and INS outputs to determine a vehicle's position. The technique works by correlating

the vehicle's path information and corresponding magnetic readings to the magnetic map. The result of the correlation process will yield the vehicle's position estimate.

In this thesis we present the theoretical foundation and considerations necessary for INS and geomagnetic navigation. The development and testing of a post-processing geomagnetic navigation framework is given. The final navigation solution is based on a particle filter framework that fuses state information from an INS, magnetometer, pressure sensor, and geomagnetic map to produce an estimate location of a free vehicle. To test and evaluate the expected performance of the navigation system a platform for simulated test was developed. The simulation platform consists of different sensor models, free vehicle trajectory simulators and means of estimating the positioning performance of a navigation solution. The trajectory generator will simulate free vehicle trajectories. The sensor models simulate the output of real sensor models by incorporating the characteristic errors of each sensor. The simulation test platform is capable of varying the sensor error model performance parameters, sensor sampling rates, vehicle trajectories, map resolution, deployment time and deployment area in an effort with the objective of testing the navigation system's feasibility and provide insight of expected navigation. The tests, results and analysis of the simulation test performed on the direct configurations of the navigation system are also given. Finally the recommended navigation system configuration, for free vehicle position estimation, is presented with its the expected navigation performance evaluate and some additional considerations for its implementation implementation.

The rest of this thesis is organized as follows. Chapter 2 provides the required theoretical background necessary for inertial system navigation and geomagnetic navigation. Chapter 2 presents the recent work done by others in the fields of underwater navigation. The problem statement and objectives of this work are presented in Chapters 4 and 5. The methodology followed in this research is discussed in Chapter 6. The test and results performed on the developed navigation system are given in

Chapter 7. Finally, chapters and presents the contribution and conclusion made in this research.

Chapter 2

Theoretical Background

This Chapter discusses the fundamental concepts of Inertial and Geomagnetic Navigation, discussing strengths, limitations, and applications in autonomous under water vehicles (AUVs).

2.1 Strap-Down Inertial Navigation

Strap-down Inertial Navigation is a process that uses information from gyroscopes and accelerometers to determine the velocity and position of the vehicle they are mounted on [1]. The navigation process relies on Newton's Law of Motion, given a measure of the acceleration in a body, it is possible to calculate its velocity and position by successive integration. The navigation process relies on Newton's Law of Motion, which states that given a measure of the acceleration in a body, it is possible to calculate its velocity and position by successive integration. Accelerometers can determine the accelerations exerted on them or a body they are attached to. If a vehicle is allowed to rotate freely within a navigation frame it becomes necessary to keep track of the vehicle's attitude (or orientation) with respect to said navigation frame. In order to enable the projection of the body accelerations, measured by the accelerometer, to the navigation frame. After which they are integrated successively to estimate the system's velocity and position with respect to the navigation frame. Vehicle attitude can be estimated using strap-down gyroscopes. These devices are capable of measuring the rotation of a body with respect to an inertial frame. Inertial

navigation systems are self contained navigation solutions, in that they do not rely on an external signal, outside the system, for navigation [1].

2.1.1 Coordinate Frames

A fundamental aspect of inertial navigation is the definition of coordinate reference frames. Such frames are used estimate and describe the navigation system's position. It is necessary that these coordinate frames have a physical significance to make terrestrial navigation feasible [1]. Below are some of the most commonly used reference frames for terrestrial navigation.

- *The body frame* (b-frame) is an axis set rigidly attached to a vehicle's body, defined by the vehicle's geometry and application [1].
- *The inertial frame* (i-frame) its origin is at the center of the Earth and its axes are fixed to the stars (non-rotating). Its axes are defined by $O_{x_i}, O_{y_i}, O_{z_i}$, where O_{z_i} coincides with the Earth's polar axis.
- *The Earth frame* (e-frame) its origin is at the center of Earth and its axes rotate with the Earth (axes are fixed to the Earth) and are defined as $O_{x_e}, O_{y_e}, O_{z_e}$, where O_{z_e} coincides with the Earth's polar axis, O_{x_e} lies along the Earth's equatorial plane where it intersects the Prime meridian and O_{y_e} completes the right handed coordinate system [1].
- *Local Geodetic Frame* (n-frame) is a geodetic spacial reference frame, whose origin is located at the position of the navigation system. Its axes are aligned with the directions of north, east and vertical down [1].

The n-frame is chosen as the navigation frame to describe the free vehicle's velocity and position.

2.1.2 Subscripts and Superscripts

Throughout this document the use of superscripts and subscripts on variables will be used to denote certain variable attributes. Superscripts will mostly be used

to describe the coordinate system in which a variable is expressed in. The subscript's meaning on a variable will depend on what the variable is describing, see below:

- *Velocity* v_j^i represents a velocity measurement in respect the j^{th} frame and expressed in the i^{th} frame.
- *Angular Rates* $\omega_{j_i}^i$ represents the angular rate of the i^{th} frame of reference in respect to the j^{th} frame of reference, expressed in the i^{th} coordinate frame.
- *Rotation Matrix* C_j^i represents the relative orientation of the j^{th} frame with respect to the i^{th} frame, in rotation matrix form.
- *Quaternion Attitude Representation* q_j^i represents the relative orientation of the j^{th} frame with respect to the i^{th} , in quaternion form.

2.1.3 Inertial Measurement Unit (IMU)

Inertial Measurement Units, or IMUs, consists of a three-axis accelerometer and a three-axis gyroscope. Together an IMU and a computer, that uses the sensor data to produce a navigation estimate yield an Inertial Navigation System (INS).

Accelerometers

Accelerometers measure the specific force (f) exerted on themselves or on a body they are attached to. Specific force is the difference between true body accelerations in the i-frame and accelerations due to gravity [1]. It is important to note that accelerometer readings are relative to inertial (non-accelerating) space. When used in non-inertial space, the readings have to be compensated for apparent forces or fictitious forces that arise due to the accelerations of the non-inertial reference frame.

$$f = a - g \tag{2.1}$$

where a represents the body accelerations and g is the gravity vector.

Gyroscopes

Gyroscopes are sensors used to measure the orientation (or attitude) of sensors themselves, or, a body attached to them, with in respect to inertial frame. The sensor output can be in the form of angular displacement (from its starting point) or an angular rate. In case of the latter, the sensor attitude can be calculated by integrating the sensor's signal from a known initial attitude of the sensor. The equations necessary for the attitude tracking using the rotation rates from a gyroscope are presented below.

2.1.4 Attitude Equations

In order track the position of an object that able to freely rotate in the navigation frame, it is necessary to track the object's relative orientation with respect to the navigation frame. The motion equations then use this information to estimate the vehicle's velocity and position in respect to the navigation frame.

The attitude of a vehicle with respect to a navigation frame is tracked using the turn rate measurements provided by the vehicle's on-board gyroscopes. For this discussion, positive axis rotations are said to follow the right hand rule, looking from the axis toward the origin, counter-clockwise rotations are positive and clockwise rotations are negative. It is important to keep in mind that the attitude of an INS is not only a function of the angles at which each axis rotates, but also the order in which these rotations take place, meaning that individual axis rotations are non-commutative.

The attitude of an INS with respect to another coordinate frame can be represented as a set of numbers for which various mathematical representations could be used, such as Euler angles, quaternions or direction cosines matrices (DCM). For this application the quaternion attitude representation will be used.

The quaternion Attitude representation is based on Eulers Rotational Theorem, which states that any two coordinate systems with the same origin are related by a

single rotation about a fixed axis [2]. A quaternions q is a four parameter attitude representation as shown in equation 2.2

$$q = [q_1 \ q_2 \ q_3 \ q_4]^T = \left[\cos \frac{\theta}{2} \quad v_x \sin \frac{\theta}{2} \quad v_y \sin \frac{\theta}{2} \quad v_z \sin \frac{\theta}{2} \right]^T \quad (2.2)$$

where $v = [v_x \ v_y \ v_z]^T$ is a unit vector that represents the axis of rotation, θ is the angle of rotation and the superscript T denotes the transpose operator.

Quaternions are not just a mathematical abstraction for attitude representation, but a whole number system complete, with a wide and complex mathematical theory [2]. This discussion will be limited to the mathematical operations necessary for quaternion attitude representation. The reader is referred to the work of Yoon, *et al.*, Valenti, *et al.*, or Chi for a more detailed discussion of the subject [2] [3] [4],

Quaternion Operators

Quaternion Norm: is denoted as $|q|$ and is calculated as:

$$q = \sqrt{q_1^2 + q_2^2 + q_3^2 + q_4^2} \quad (2.3)$$

Quaternion Normalization: q is normalized by dividing each of its elements by its norm:

$$\|q\| = \frac{q}{|q|} \quad (2.4)$$

where $\|q\|$ has a unit length and thus provides a definition for a unit quaternion.

Quaternion Conjugate: denoted as q^* , and is calculated by inverting the sign of a quaternion's vector elements:

$$q^* = [q_1 - q_2 - q_3 - q_4]^T \quad (2.5)$$

Quaternion Inverse: denoted as q^{-1} , and calculated by dividing a conjugate of a quaternion by its norm:

$$q^{-1} = \frac{q^*}{|q|} \quad (2.6)$$

Note the the inverse of a unit quaternion q_u is its conjugate q_u^* because of its unit norm.

Quaternion Multiplication: The multiplication of quaternions p and q denoted as $q \otimes p$, calculated as:

$$q \otimes p = \begin{bmatrix} q_1 p_1 - q_2 p_2 - q_3 p_3 - q_4 p_4 \\ q_1 p_2 + q_2 p_1 + q_3 p_4 - q_4 p_3 \\ q_1 p_3 - q_2 p_4 + q_3 p_1 + q_4 p_2 \\ q_1 p_4 + q_2 p_3 - q_3 p_2 + q_4 p_1 \end{bmatrix} \quad (2.7)$$

It is evident from equation 2.7 that quaternion multiplication is non-commutative. But quaternion multiplication is associative [4].

Rotation Matrix from Quaternion: it is possible to derive an equivalent DCM expression from a quaternion using the following equation:

$$C = R(q) = \begin{bmatrix} q_0^2 + q_1^2 - q_2^2 - q_3^2 & 2(q_1 q_2 - q_0 q_3) & 2(q_1 q_3 + q_0 q_2) \\ 2(q_1 q_2 + q_0 q_3) & q_0^2 - q_1^2 + q_2^2 - q_3^2 & 2(q_2 q_3 - q_0 q_1) \\ 2(q_1 q_3 - q_0 q_2) & 2(q_2 q_3 + q_0 q_1) & q_0^2 - q_1^2 - q_2^2 + q_3^2 \end{bmatrix} \quad (2.8)$$

Quaternion Attitude Representation

The quaternion representation of the body-frame attitude of the with respect to the navigation-frame is parameterized in the quaternion q_b^n . It is possible to track q_b^n as the vehicle rotates using equation 2.9 [1].

$$\dot{q}_b^n = \frac{1}{2} q_b^n \otimes q_{nb}^b \quad (2.9)$$

where $q_{nb}^b = [0\omega_{nb}^b]^T$ and ω_{nb}^b represents the body frame rate with respect to the navigation frame. ω_{nb}^b can be estimated from the rotation rate provided by on-board gyroscopes ω_{ib}^b using the following equation:

$$\omega_{nb}^b = \omega_{ib}^b - (\omega_{ie}^b + \omega_{en}^b) \quad (2.10)$$

where ω_{ie}^b represents the e-frame rate with respect to the i-frame and ω_{en}^b is derived from the INS's velocity estimate and represent the n-frame turn rates with respect to the e-frame.

A full derivation of equations 2.9 and 2.10 can be found in [1] and [4].

Use of Quaternion for Vector Coordinate Frame Transformation

A vector quantity defined in the b-frame, like a measure of specific force $f^b = [f_x^b \ f_y^b \ f_z^b]^T$, can be transformed into the n-frame using quaternions. First, a vector quaternion is created from the original body frame vector $q_{fb} = [0\ f^b]^T$, then we use equation 2.11 to transform the vector into the n-frame:

$$q_{fn} = q_b^n \otimes q_b^{n*}, \quad (2.11)$$

or alternatively equation 2.8 can be used as follows

$$f^n = R(q_b^n) f^b \quad (2.12)$$

For a full derivation and explanation as how quaternion multiplication performs vector transformation, please, refer to [4].

2.1.5 Motion Equations

For our navigation application we have chosen to use the Local Geodetic Frame (n-frame) to describe the vehicle's velocity (v_3^n) and position (r). In the n-frame position and velocity are described in latitude L , longitude l , height h , northern

velocity V_N , southern velocity V_S and downward (local vertical) velocity V_D .

$$r^n = [L \ l \ h]^T \quad (2.13)$$

$$v_e^n = [V_N \ V_S \ V_D]^T \quad (2.14)$$

The motion of the vehicle over the Earth in the n-frame is described by kinematic equations 2.15 and 2.16 [1]. These are also referred to as navigation equations.

$$\dot{v}_e^n = C_b^n f^b - (2\omega_{ie}^n + \omega_{en}^n) \times v_e^n + g_l^n \quad (2.15)$$

$$\dot{r}^n = \begin{bmatrix} \frac{1}{R+h} & 0 & 0 \\ 0 & \frac{1}{(R+h)\cos(L)} & 0 \\ 0 & 0 & -1 \end{bmatrix} \begin{bmatrix} V_N \\ V_E \\ V_D \end{bmatrix} \quad (2.16)$$

where f^b is the three-axis specific force measurement provided by onboard strap-down accelerometers; C_b^n is the direction cosine matrix attitude representation from equation 2.8; ω_{ie}^n is the Earth's rotation rate with respect to the inertial frame, expressed in n-frame coordinates; ω_{en}^n is the rotation rate of the n-frame with respect to the Earth, also referred to as the transport rate; and g_l^n is the local gravity vector expressed in navigation frame coordinates. The navigation equations expressed here are derived and explained in further detail in the literature [1].

2.1.6 INS Limitations

This section explores the inherent errors of INS systems and their effect on navigation performance. Figure 2.1 show a simplified diagram of an INS system. This diagram will be used in the analysis and discussion of INS system errors. A simplified diagram facilitates the analysis and interpretation of results.

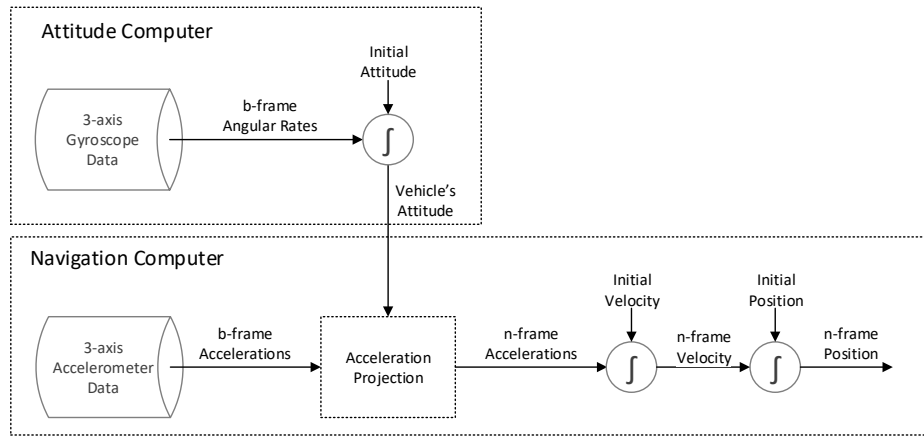


Figure 2.1 : Simplified three-axis INS system diagram.

MEMS Accelerometer and Gyroscope Error Characteristics

This section presents the error characteristics inherent to MEMS gyroscopes and MEMS accelerometer. MEMS sensors are built using silicon micro-machining and as a result they can be inexpensive to manufacture, small in size, low weight, require low power, reliable, low maintenance and have a wide temperature operating range. The disadvantage of MEMS sensor is their accuracy. The purpose of this discussion is to shed some light on how typical MEM IMU sensor errors manifest themselves in INS error. A more detailed discussion of the effect of IMU errors on INS estimates can be found in [1] and [5].

Constant Bias. The constant bias of an IMU sensor is the average idle sensor readout, when it is not rotation or accelerating [5]. A constant bias in gyroscopic outputs results in an orientation error that, as a result of the integration process, grows linearly with time. A constant bias in the accelerometer outputs results in velocity errors that grow linearly with time and position errors with the square of time, as a result of the single and double integration process necessary to solve the navigation equations. This type of error is trivial to compensate, by subtracting the

known bias from the output of the sensor. This bias can be estimated by averaging of the sensor outputs while it sits idle.

White Noise. Thermo-mechanical noise with frequency spectrum greater than the sampling rate of the sensor gives rise to a white noise manifestation, which perturbs the sensor output. White noise sequence is a zero-mean uncorrelated random phenomena with finite variance.

When white noise is integrated once, it results in a first-order random walk sequence with zero mean and its variance grows linearly with time. When white noise is integrated a second time, it creates a second order random walk sequence with zero mean and a variance that grows with time to the third power [5], meaning that attitude and velocity estimates will be perturbed by a first-order random walk error sequence and position estimates will be perturbed by a second-order random walk error sequence.

Bias Instability The bias in MEMS sensor varies over time due to flicker noise arising from its electronic components. The frequency spectrum of flicker noise is $1/f$, thus its effects are most noticeable at low frequencies. This error is usually modeled as a band limited random walk, which describes how the bias of a sensor may change over time. If we assume the error can be modeled as a random walk process, then bias instability error causes a second order random walk error sequence in INS estimates of attitude and velocity and a third order random walk error sequence in the INS estimates of position.

Temperature Effects. Environmental temperature fluctuations cause drift on the sensors output biases. As discussed before any remaining sensor bias would cause estimate errors that grow linearly or with the square of time, depending on the number integrations performed. The problem with temperature effects is that the relationship between the sensor bias and temperature is highly non-linear, making characterization necessary for every sensor in order to compensate for such effects [5].

Scale Factor. Scale factor errors is the ratio relationship between input stimuli and output readout. If a sensor is stimulated at 50% of its input range the expected sensor readout is 50%. But in reality the output is a function of the input but scaled linearly. For example if the input stimuli to a gyroscope is $5^\circ/s$ and there is a 2% scale factor then the output measurement is $5.1^\circ/s$

Orthogonality Errors. Error resulting from the three sensitive sensor axes not being completely orthogonal to one other. Usually compensated through the calibration process.

Axis Asymmetry. Refers to the difference in sensor readout when a stimuli is applied to the positive direction of a sensor axis and when the same stimuli is applied to the negative direction of the same axis. Usually compensated through the calibration process.

Alignment Errors

Inertial navigation estimates depend greatly on correct initial estimates of orientation, velocity, and position. These estimates are obtained through an alignment process. Alignment varies with the navigation application. Incorrect attitude alignment results in a constant attitude error output and incorrect projections of measured acceleration, which causes errors when they are integrated twice to solve navigation equations.

Open Loop Operation

The limiting factors of an INS are not just the errors associated with the sensor measurements, but also because they estimate the system velocity and position without a direct measurement of these system states (open-loop operation). By accumulating small errors, from the sensors, over each iteration the INS estimates of vehicle state can quickly diverge substantially from the real state, even with sensor error compensation [6]. If left uncorrected, there would be no limit on how large

the divergence can become. A possible solution for this problem would be acquiring more accurate sensors. This alternative would not only raises costs, but also sensors cannot be made arbitrarily accurate [1]. To tackle this problem, engineers have adopted a technique known as aiding, which essentially provides feedback information to the INS, via external measurements of the vehicle position and/or velocity. With feedback information, errors from the INS can be corrected or constrained [7] [8].

2.1.7 INS Aiding

An INS has six degrees of motion freedom: surge, sway, heave, roll, pitch and yaw, as depicted in Figure 2.2 . Modern INSs can obtain accurate external attitude estimates (roll, pitch and yaw) by utilizing a magnetic compass as an aiding sensor to correct the INS estimates of orientation [7] [9]. Through the employment of a pressure sensor or barometer, and using the physical properties of the traveling medium (air or water), the heave axis estimates of position and velocity can be easily corrected [8]. The surge and sway are the only degrees of freedom left un-aided, a potential aiding scheme is the Global Positioning System, which provides estimates of position on the Earth and Earth relative velocities. But GPS cannot be used in underwater navigation applications, thus aiding the surge and sway of an INS for underwater applications has become the challenge of modern underwater navigation. Chapter 3 discusses some of the aiding schemes used today for AUV navigation.

2.2 AUV Depth Estimate

As mentioned previously an AUV's depth can be estimated directly from a measurement of a pressure. This section presents a brief background theory and some of the consideration needed to obtain a depth estimate from a pressure measurement.

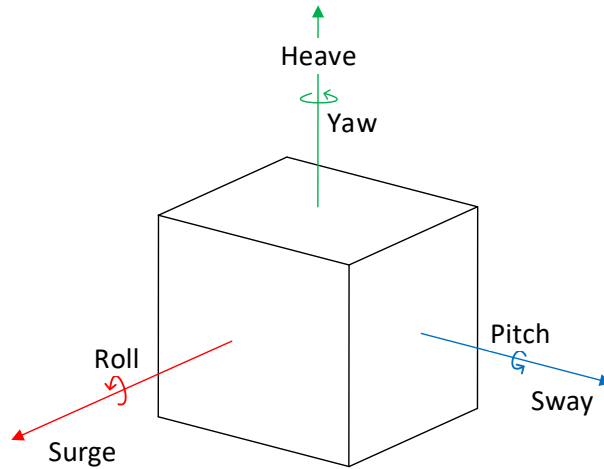


Figure 2.2 : A standard vehicle degrees of motion freedom

2.2.1 Total Pressure Field

The total pressure field sensed in a underwater environment is the sum of the hydrostatic pressure of the water column, atmospheric column and the dynamic surface-wave-induced pressure field. In the hydrostatic pressure of the water column can be calculated using the hydrostatic pressure model, Equation 2.17.

$$p = \rho_{seawater}gd \quad (2.17)$$

where p is pressure, d is depth and $\rho_{seawater}$ is the density of sea water.

The challenge in using Equation 2.17 is that $\rho_{seawater}$ is not constant. Variations in $\rho_{seawater}$ are mostly driven by depth, due to the compressibility of sea water at high pressure, and other factors are the properties of temperature and salinity of the sea water [10]. The United Nations Educational, Scientific and Cultural Organization (UNESCO) has provided an empirical standard formula for of conversion from hydrostatic pressure to depth. The equation considers the compressibility of sea water with depth, shown in Equation 2.18 [11].

$$d = \frac{c_1 p + c_2 p^2 + c_3 p^3 + c_4 p^4}{g(Lat) + \frac{1}{2} \Upsilon p} + \frac{\Delta D}{9.8} \quad (2.18)$$

where $g(Lat)$ is the gravity at the ocean surface in m/s^2 and expressed as:

$$g(Lat) = 9.780318(1.0 + 5.2788e-3 \sin^2(Lat) + 2.36e-5 \sin^4(Lat)) \quad (2.19)$$

d is depth in meters, p is in decibars, c_1, c_2, c_3 , and c_4 are constant equal to 9.72659, $-2.25121e-5$, $2.279e-10$, and $-1.82e-15$, respectively. Υ is the mean vertical gradient of gravity, equal to $2.184E - 6$ in $m/s^2/decibar$.

The first term in Equation 2.18 is the depth estimate from a hydrostatic pressure measurement of a standard ocean water column. A standard ocean is defined to have 35 practical units of salinity (psu) and a temperature of $35^\circ C$. The second term is a correction calculated from the difference between the water column actual density and the density of the standard ocean. The correction term is captured in ΔD , called geopotential anomaly and is expressed in J/kg . $\Delta D/9.8$ is usually less than 2 meters [11]. Equation 2.18 found is accurate to 0.1m over the pressure range of 0 – 1000 decibars.

The effect of the dynamic surface-wave-induced pressure field is proportional to the surface elevation from the mean sea level directly above the pressure sensor. The amplitude of the pressure field is dampened with depth, depending on the wavelength of the incoming wave, longer waves are less damped than shorter waves [12]. The effects of atmospheric pressure can be considered constant for a period of a few hours, depending on the weather, and are usually measured at the surface and added as a correcting factor to the depth estimate.

2.2.2 Pressure Sensor Model

A pressure sensor may be modeled as: [13]

$$p_{mea} = \alpha p + b + \omega_{press} \quad (2.20)$$

where p is the real pressure, p_{mea} is the measured pressure provided by the sensor, α is a gain factor, b is a constant offset and ω_{press} Gaussian measurement noise.

Calibrated underwater pressure sensor have a reported accuracies of 0.1% to 0.01% of their full sensing scale [8]. Attaining these accuracy levels require the calibration procedure to estimate for the thermal dependencies of α and b of the sensor model.

2.2.3 Pressure Measurement Model

Now that the measurement environment, pressure to depth equation, and pressure sensor models have been presented it is possible to establish a measurement model, relating vehicle depth to the pressure measured:

$$p = P(d, 0, 35) + \frac{\Delta D}{9.8} + \omega_{press} \quad (2.21)$$

where $P(d, 0, 35)$ is the expected pressure of a standard ocean water column at depth d . $\frac{\Delta D}{9.8}$ is the pressure difference between in densities of the water column above the sensor and the density of a standard-ocean water column. ω_{press} is the measurement noise from the sensors output.

The effects of the dynamic surface-wave-induce pressure field was not considered in the measurement model since its effects are mostly noticeable in shallow waters and negligible at the typical depth of FV operation. The pressure resulting from the local atmospheric condition were also not considered as these are assumed to be nearly constant.

2.3 Geomagnetic Navigation

The Earth's magnetic field (EMF) is a vector field with discernable properties that can be considered as a source of positional navigation information [14]. EMF

maps and models can be used for reliable navigation on 98% of the Earth's surface. These maps are periodically updated because of their military and commercial applications [15]. Using the EMF as a navigation source has the benefits of: being an entirely passive self-contained navigation solution, requiring no external signal and offering guaranteed bounded position error [16]. Geomagnetic Navigation process, consist of correlating a geomagnetic profile, sampled by the an on-board magnetometer and correlating it to a location on a pre-stored geomagnetic map.

A geomagnetic navigation system is composed of: 1) an INS; 2) a magnetometer; 3) a pre-stored magnetic map; 4) a geomagnetic algorithm; and 5) an optimal estimator [17]. Figure 2.3 depicts the architecture of a generic geomagnetic navigation system.

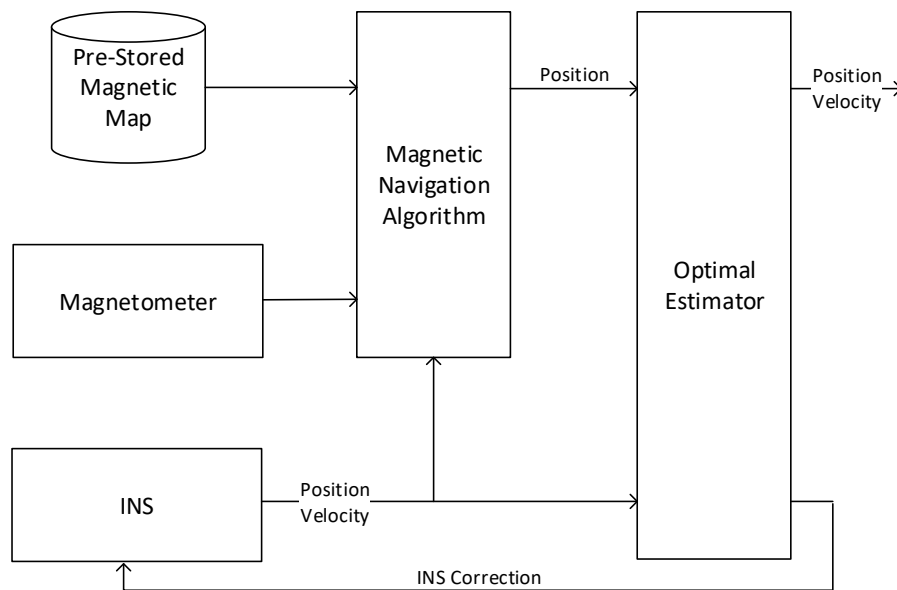


Figure 2.3 : Components of Geomagnetic Field

The magnetometer is periodically sampled during vehicle operation and is used to build the magnetic profile of the vehicle's track. The INS provides independent estimates of vehicle attitude, velocity, and position; this information is used to estimate where magnetic samples are taken from, as part of the magnetic profile. Potential

vehicle track data are then extracted from the pre-stored magnetic map and using geomagnetic navigation algorithms they are correlated to the measured magnetic profile, in an effort to obtain an estimate of vehicle position. Both position estimates, from the INS and geomagnetic navigation solution, are then fused to produce an optimal position solution. Common estimators like a Kalman Filter can provide online corrections to the INS, to amend for accumulated errors.

The following sections elaborate more on the aspects of geomagnetic navigation and are Section 2.3.1 discusses the constituents of the Earth’s magnetic field (EMF) and its different components. Section 2.3.2 discusses the properties of a magnetometer sensor, its measurement model and special considerations when deployed in the field. The different algorithms used for magnetic navigation are then discussed in section 2.3.3.

2.3.1 Earth’s Magnetic Field

The EMF is complex and the result of a sum multiple contributors like the Earth’s main magnetic field (caused by its conducting fluid inner core), magnetized crustal rocks and currents flowing in the ionosphere and magnetosphere [17]. The EMF can be modeled by the following equation: [18]

$$H(r, t) = H_m(r, t) + H_a(r) + H_c(r, t) \quad (2.22)$$

where r represents a position on the Earth and t represents time. The dominating constituent of the EMF is the Earth’s main magnetic field ($H_m(r, t)$). Its behavior varies slowly in time and is predictable by models, like the the World Magnetic Model. Magnetic fields arising from currents in the ionosphere and magnetosphere ($H_c(r, t)$) contribute around 1% of the total field intensity. Its behavior varies on a daily basis and is also dependent on the Earth relative position, but its is also predictable by models. $H_a(r)$ arises from magnetized crustal rocks and behavior

can be considered constant in time but variable in space [19]. The term anomaly field is used to refer to $H_a(t)$ in literature and this document. The anomaly field is the most common magnetic field used for navigation because of its non-changing, distinguishable features [19].

Being a vector field, the EMF possesses different features like total field intensity $|H|$, north component H_n , east component H_e , vertical component H_v , declination D and inclination I , as shown in Figure 2.4.

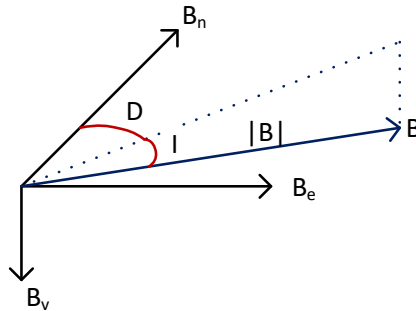


Figure 2.4 : Components of a generic geomagnetic navigation system

Even though the EMF has different components most maps used for navigation only map total field intensity.

2.3.2 Magnetometer

A three-axis Magnetometer is an instrument that can measure the magnitude and direction of magnetic fields in its environment. This includes the EMF and fields that may arise from surrounding ferromagnetic objects, cabling, electric currents, motors, or batteries. Since most vehicle structures include ferromagnetic materials and/or electrical components, obtaining accurate samples of the EMF with an on-board magnetometer can be a challenging task. These unwanted magnetic fields distort any samples of the EMF unless they are calibrated for. These distortions can be classified

into hard-iron and soft-iron effects [15]. Hard-iron effects manifest in magnetometer readings as constant biases and are caused by materials like permanent magnets and constant electrical currents. Soft-iron effects manifests themselves as changing biases, depending on the relative orientation of the vehicles with respect to the local EMF. Soft-iron effects are caused by materials that generate their own magnetic fields in response to underlying magnetic fields [20]. Magnetometers also suffer from scale-factor, bias, and cross coupling errors but these are indistinguishable from hard/soft iron effects.

Taking into account the different noise manifestations a magnetometer can exhibit, a measurement model can be established, like equation 2.23 [20].

$$H_{measured} = Sm^b + h + \varepsilon, \quad (2.23)$$

where m^b is the local magnetic vector in the sensor frame. S is the soft-iron effects, h is the hard iron effects, and ε is gaussian noise with $N(0, \sigma^2)$ distribution. In a homogenous magnetic field, magnetometer measurements can be visualized as a sphere centered at the origin of the sensor frame [21]. Hard-iron effects offset the measurement sphere from the origin. Soft-iron effects stretch and distort the measurement sphere into an ellipsoid.

Magnetometer calibration is the process by which S and h are estimated. Practical magnetometer calibration schemes take advantage of the constant magnitude of magnetometer measurements when in a homogenous magnetic field. The process consists of fitting the magnetometer ellipsoidal response into a sphere centered at the origin of the sensor frame [20] [21]. Because magnetometers are so sensitive to the magnetic environment, careful calibration might be necessary before each deployment [21].

2.3.3 Geomagnetic Navigation Algorithms

There are two types of algorithms that can be implemented to for geomagnetic navigation: geomagnetic matching and geomagnetic filtering.

In geomagnetic matching, as the vehicle operates on a reference area it periodically samples the geomagnetic field and estimates the position of the measurement using data from the on-board INS [19]. Let $x_k = (x_0, x_1, \dots, x_n)$ represent the sequence of position estimate produced by an INS, where each magnetic sample $M_k = (M_0, M_1, \dots, M_n)$ was taken. The M_k samples are then correlated to magnetic data sets $M(i, j)_k$ derived from the on-board geomagnetic map. The method by which potential vehicle magnetic tracks are chosen is called the searching strategy. Conventional searching strategies locate the center of the search field at x_0 and the size of it as $3\sigma_{x_0}$, where σ_{x_0} is the standard deviation of the initial position error of x_0 . Each point inside the searching area is considered a candidate point for x_0 real location. The relative path of the INS is overlaid on each candidate point, creating multiple paths with the same trajectory as x_k but different origins. Then the magnetic data from the map is sampled for each potential path at the corresponding location where M_k was sampled, creating a set of potential vehicle magnetic tracks $M(i, j)_k$. Here i and j represent the horizontal and vertical offsets from x_0 and are inside the search field. Then, every potential magnetic track in $M(i, j)_k$ is then compared to M_k using correlation analysis algorithms like Mean Average Difference (MAD), as shown in equation 2.24 [19].

$$MAD(i, j) = \frac{1}{n} \sum_{k=0}^n [M(i, j)_k - M_k] \quad (2.24)$$

where n is the number of magnetic samples taken in a given path, also know as correlation length. The potential magnetic track with the minimum MAD result in equation 2.24 is the position result of the algorithm. The longer the correlation length, the better the chance of building a unique magnetic profile, increasing the chances

of obtaining a good match in the navigation algorithm. However the resulting INS trajectory would have accumulated more error, causing distortions in the estimated INS position. The correlation length is usually selected based on the relative contours of the operating area of the vehicle and expected INS performance [19].

Some limitations of the magnetic matching algorithm are its precision, limited by the accuracy of the onboard EMF samples, and the accuracy of the map grid [17].

The anomaly field intensity can be thought of as being a function of the sampling location (position). Geomagnetic filtering consists of the creation of a field intensity model for the local anomaly field around the deployment area. Common filtering methods are then used to obtain a position, velocity, and attitude estimates based on INS information, magnetic model, and actual measurements from the magnetometer.

Geomagnetic models can be created using fitting algorithms like spline methods and can be applied to real magnetometer data samples or maps [14]. The process starts by obtaining a predicted state of the system from INS information. This information is fed into the local geomagnetic model to obtain a predicted magnetometer measurement which is later compared to the actual magnetometer sample, when it becomes available. The difference between the two is then used to estimate the true state of the system using optimal estimator [14]. The Extended Kalman Filter (EKF) is a common filtering method used for geomagnetic filtering since models of local geomagnetic intensity tend to be non-linear functions of system position. The EKF works by linearizing the system equation and magnetic model around the current operating point of the system, thus minimizing the effect of linearization errors.

Since geomagnetic filtering is not a batch process, like geomagnetic matching, it offers comparable navigation accuracy at less computational burden. But it still requires accurate samples of the EMF aboard a vehicle and an accurate model of the local geomagnetic field.

Chapter 3

Previous Work: AUV INS Aiding

A standard AUV has six degrees of motion freedom surge, sway, heave, roll, pitch and yaw, as depicted in Figure 2.2 . AUVs can obtain accurate external attitude estimates (roll, pitch and yaw) by utilizing magnetometer and accelerometer as aiding sensors to correct for the gyroscopic attitude estimates from the INS [9]. With a pressure-meter and the physical properties of water, the heave axis position estimates can be corrected [8]. The surge and sway are the only degrees of freedom left un-aided, becoming the challenge in modern underwater navigation systems [7].

The rest parts of this Chapter presents different aiding schemes developed for, or applicable to, AUV navigation. The fundamental concepts of operation, performance, and if applicable, implementations are discussed for each aiding scheme. Section ?? presents the observed FV dynamics during a deployment at the Puerto Rico Trench and Section 3.1 is a summary of all the navigation schemes presented.

3.0.1 Acoustic Time-of-Flight Navigation

Acoustic time-of-flight navigation is a technique pioneered in the 1960's and 1970's, that is still used today for precise underwater tracking and navigation. The technique relies on a measure of distance and direction from the AUV to the known beacon location [8].

Long Base Line (LBL) is an acoustic navigation technique in which an AUV's position is triangulated using acoustic distances from the AUV to a framework of marooned transponder beacons [7]. The marooned transponders have to be deployed and

their locations recorded before being used for navigation. As part of the navigation scheme, the AUV possesses a transceiver device that broadcasts a ping. Listening beacons then reply with identifying information. By estimating the travel time of the replying messages and the sound velocity of the surrounding water, it is possible to estimate the vehicle distance from each of the replying beacons, subsequently triangulating the vehicle position within the beacon framework [7].

The operating range, precision, and update rate of LBL systems depend on the carrier frequency used by the beacon framework and the number of beacons in the AUV operating area. The higher the carrier frequency of the beacon framework, the more accurate the position estimate of the navigation scheme, but the carrier frequency is limited by the rapid attenuation of high-frequency sound in water [8]. In a work presented by Allen *et al.*, the REMUS AUV achieved autonomous underwater navigation with accuracies of 20 m or less using only two transponder beacons and onboard INS [22]. The authors note that the precision of the reported navigation accuracy could be enhanced by increasing the number of beacons and by using a more accurate methods of calibrating beacon location.

The main source of error in acoustic navigation is in estimating the local water sound speed. Since sound speed is dependant on the physical characteristics of the surrounding water, which can change over time, and might not be homogenous. Presently LBL is the best method for obtaining sub-meter position accuracy [23]. Even though LBL offers the best navigation accuracy it is quickly being replaced by other navigation schemes like Ultra Short Base Line (USBL) due to the higher cost and preparation overhead of the beacon framework.

USBL is similar in operating principles to LBL, but instead of using a framework of multiple moored transponder beacons, a cluster of beacons is attached to the hull of a ship. The ship then acts as a moving beacon for the AUV by tracking the ships

position via Global Positioning System (GPS) [8]. The cluster of transponders is then used to estimate the AUVs distance and direction from the ship.

Jalving *et al.* developed a USBL navigation solution for the HUGIN 4500 series AUV [24]. The navigation system was capable of obtaining horizontal navigation accuracies in the order of 2m and 4m at depths of 1300 m and 2100 m respectively. The average operating range of USBL system is 4 km, limited by the attenuation of high frequency sound in water. The operating rang of USBL enables it to be a prime candidate for many underwater navigation applications but inadequate for depths that exceed 4 km.

3.0.2 Doppler Navigation

The development of high frequency multi-beam sonar technology has enabled accurate measurements water velocity, 0.3% or less of the total measured velocity [8]. These accurate estimates of underwater velocities have been used by researchers as a source of navigation information to aid INS for underwater navigation. This strategy is named Doppler navigation and is adopted, researched, and implemented by many underwater navigation system designers, granting the technique great navigation accuracies.

A Doppler Velocity Log (DVL) is an oceanographic instrument capable of measuring its velocity relative to the ocean floor, though it requires near floor operation for accurate measurements. Modern DLVs also employ a three-axis compass to track the sensor's orientation in time, in order to accurately interpret the direction of velocity estimates. The Earth relative velocity estimates provided by the DVL sensor are then used as a feedback mechanism to correct INS estimates of surge and sway velocities.

Grenson, *et al.*, described and analyzed the performance achieved by the Morpheos AUV which incorporated a mid-range INS, magnetometer, GPS and DVL data

asynchronously [25]. The asynchronous fusion of INS, DVL and GPS navigation information was achieved using an Extended Kalman Filter. The navigation system was capable of around 1% (70 m) positioning accuracy of the total distance traveled of 7500m. Jalvin, *et al.*, reported navigation accuracies of 6 m utilizing a DVL-aided INS and periodic surface GPS fixes for the HUGIN 4500 AUV [24].

A limiting factor in doppler-aided navigation systems is that the navigation solution will gradually drift in due to remaining DVL biases, requiring additional periodic aiding sources, like GPS fixes. Other sources of error include accurate knowledge of local water sound velocity and estimates of the instruments orientation over the course of deployment. The requirement of needing a DVL can considerably reduce the payload capacity for small AUVs. In addition, if sensor environment is not optimal for accurate measurements, or is too far from the ocean floor, the sensor may not be capable of producing a measurement [6] [25], considerably affecting its navigation accuracy.

3.0.3 Geophysical Navigation

Geophysical or terrain navigation uses unique near Earth observable features and maps of these features to obtain an estimate of an AUV position. The goal of this navigation technique while underwater is to provide performance similar to GPS without relying on the presence of the GPS electromagnetic signal. The success of any geophysical navigation system is highly dependent on the presence of identifiable features, the ability to accurately measure them, and availability of feature maps [7] [26] [15]. The un-jammable nature and lack of an external reference signals make any navigation solution based on geophysical fields reliable and robust. Figure 3.1 depicts a generic geophysical navigation system. It consists of an INS, a geofield map, and a set of geofield sensors. The navigation computer uses an approximate position from the INS, as input, to determine its approximate position on the geofield map based on the data provided by the geofield sensor. There are three geophysical fields

used for navigation today: the Earth’s magnetic field, the Earth’s gravity field and terrain topography.

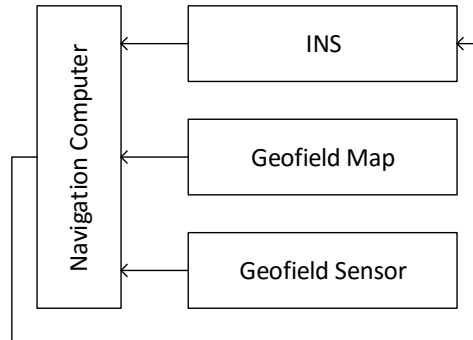


Figure 3.1 : Block diagram of a generic geophysical navigation system

Geomagnetic Navigation

An introduction to the concept of geomagnetic navigation, considerations and error sources was discussed in Section 2.3. Thus this discussion will be limited to reporting on the work done by others in the field.

Feng, *et al.*, developed a magnetic navigation system based on magnetic matching using Iterative Closest Contour Point (ICCP) as the matching algorithm [27]. ICCP is derived from Iterated Closest Point (ICP), an algorithm used to minimize the difference between two data sets. The process is based on the assumption that the vehicle actual location is consistent, or close to, the corresponding magnetic contours of the magnetic profile measured during vehicle operation. The path with the shortest distance between the INS estimate position and the corresponding magnetic contours are chosen as the output of the algorithm. The potential paths are obtained by rigid transformation of the INS track. The proposed navigation platform was verified via simulation using the models for a medium grade INS, a compass model with a measurement variance of 2 nT and Beijing’s geomagnetic anomaly field map. The results showed that position accuracies of 200 m could be achieved in a flight path

of 25 km in both magnetically rough and smooth paths. Ren, *et al.*, reported on a simulation study of navigation performance and formulation of an ICCP algorithm [28]. The study found that an ICCP formulation based on Menq’s algorithm had improved position estimation accuracies of 20 m or when compared to traditional ICCP formulation.

Zhao, *et al.*, tested and proved a marine geomagnetic matching navigation system based on ICCP and MSD by field experimentation [17]. They utilized a survey vessel with marine magnetometer and GPS to create a 10 km by 20 km local geomagnetic anomaly map. The same vessel was used as the testing platform for the field experiments. The vessel did not have an on-board INS but was simulated by adding expected INS error into the known vessel known. The INS model parameter used corresponded to a medium grade INS and the marine magnetometer with a measurement accuracy of 2.73 nT. The results showed that both matching algorithms based on ICCP or MSD were suitable for position accuracies of less than 100 m, with high stability. The authors noted that an ICCP algorithm was more suitable for real-time applications because of its lighter computational burden.

In the simulation work by Caifa, *et al.*, the use of real geomagnetic field data for the navigation requirements of an autonomous aerial vehicle were presented and evaluated [14]. The objective was to evaluate and compare the performance of geomagnetic matching against geomagnetic filtering. The simulation components consisted of an INS, geomagnetic maps and simulated magnetometer readings. The performance of both algorithms was evaluated over paths with magnetically rough and smooth topography. Their results show that both algorithms could fulfil the task of flight navigation with positional accuracies of around 100 m. Geomagnetic matching was the most efficient and accurate when dealing with larger initial position errors, if the navigation path contained rough magnetic topography. Geomagnetic filtering demonstrated better performance in flight paths with less magnetic information as

long as the initial condition errors were within 1.5 km and magnetic noise was below 100 nT.

The simulation work by Liu, *et al.*, presented the performance of a geomagnetic aiding navigation system that used both matching and filtering techniques for AUV applications [19]. The magnetic matching algorithm used by the authors was presented by Ren [28]. Matching algorithms were used for the first 100 s of deployment, geomagnetic filtering was then used for the remainder of the vehicle deployment. The filtering scheme used was that of a linear nearest point-based Kalman filter (NPKF), in which the highest probability was assigned to the nearest point on the map to the INS position estimate that would match the magnetic signature measured. The simulation parameters consisted of using a medium grade INS, a compass with 10 nT of measurement accuracy and geomagnetic maps with grids of 100 m x 100 m and 50 m x 50 m through paths of both rough and smooth magnetic topography. The simulation results demonstrated that the NPKF did not accumulate error over time and were able to achieve position accuracies within one map grid in both rough and smooth contour paths.

Quintas *et al.* proposed a geophysical navigation method that used bathymetric-based terrain-aided navigation with geomagnetic-based geophysical navigation for small affordable AUVs [29]. The authors used a particle filter framework to fuse the navigation estimates from both systems. The proposed system was tested aboard the Autonomous Surface Vehicle (ASV) Medusa on a shallow water lake. The ASV was equipped with a medium grade INS, a magnetometer with 0.2 nT measurement accuracy, a bathymetric navigation system, and GPS. GPS measurements from the ASV were only used to evaluate the navigation system performance. First, a geomagnetic anomaly map of the area was constructed by scouting the area using magnetometer and GPS information. Later, a field test was performed and the navigation system demonstrated position error within 5 m, even in areas with smooth terrain features.

Liu *et al.* modeled INS error as affine transformations (translation, rotation and zooming) of the real path of an UAV, assuming attitude errors remain constant between update intervals [30]. Based on these assumptions, the authors proposed a multi-level geomagnetic matching algorithm to estimate an UAV position. The first-level obtained potential starting points for path candidates using a contour constraint strategy [31]. The paths with the best fit, from the first-level, pass on to the second-level where the paths are subjected to rotation and zooming transformations at a coarse level. The paths with the best fit, then move on the third-level, where they are subjected to a round of fine rotation and zooming transformations. After the third-level of transformations the path with the best geomagnetic fit between the measured geomagnetic profile and the magnetic profile sampled from the geomagnetic map, was chosen as the output of the algorithm. The algorithm was verified via simulation using geomagnetic anomaly maps from the United States Geological Survey, a model of a medium grade INS, and simulated compass measurements with 50 nT measurement variance. The results showed position estimates within 500 m of error. Later the algorithm was tested using data from a aerial geological survey. The aircraft was equipped with a navigation-grade INS, a high performance magnetometer, and a GPS. The GPS data was used to measure the error performance of the algorithms. The results showed a horizontal position error within 50 m.

Kauffman and Raquet (2014) developed a geomagnetic matching navigation system using a particle filter [32]. Their navigation platform was tested and validated with field tests. The tests consisted of driving a van equipped with a medium grade INS, GPS, and magnetometer around a target road. Some of the trips were used to create a local geomagnetic map using the magnetometer and GPS data. One of the trips was used as a navigation test, using only INS and magnetometer data. The system was able to provide position accuracies within 30 m of the true position using 50,000 particles in the filter.

Liu *et al.* tackled the problem of geomagnetic navigation without a prior magnetic map given the geomagnetic signature of the target area where the AUV was expected to navigate to [33]. The problem was approached by proposing a genetic search algorithm where an AUV would select a random heading and travel a predetermined distance. At the new location, the AUV samples the geomagnetic signature of the local area, then compares it to the target signature previously determined. If the local signature was closer to the target signature, the current heading is given extra weight compared to other potential headings for the algorithm's next iteration. If the local signature was further from the target signature, then the current heading is given a relatively low weight for the next iteration. The process was repeated until the local magnetic signature matched the target magnetic signature within a specified margin. The algorithm was verified to reach its target location via simulation experiments using the World Magnetic Model, but the simulation did not include the effects of water currents or other environmental parameter that might affect the navigation system performance.

Teixeira and Pascoal (2013) also tackled the problem of geomagnetic navigation without a map. Their approach was based on potential field inversion, where the AUV was capable of estimating its distance from surrounding magnetic dipoles, providing a relative position estimate [34]. The navigation solution consisted of a high accuracy magnetometer with a measurement accuracy in the order of 1 nT or less, and a magnetic gradiometer capable of taking differential measurements of the local magnetic field. The navigation system was verified via simulation where a real magnetic map was used as the testing environment. The algorithm demonstrated a relative horizontal position accuracy of less than 50 m. This system could be combined with other navigation sources like INS to provide a global positional estimate since its error characteristics were bounded in time.

Djapic *et al.* explored the applications of a geomagnetic navigation on a fleet AUV of gliders equipped with medium grade IMU sensors and magnetometers of 1×10^{-11} T measurement accuracy [35]. The distributed navigation solution presented was cooperative in the sense that an AUV position estimate was based on its own estimate and the estimates of its neighbors. The algorithm was based on a distributed Kalman filter framework that took in consideration the communication delay between the AUV. Although the algorithm was presented with great detail the authors did not report performing experiments to evaluate performance.

The previously mentioned geomagnetic navigation strategies relied on a magnetometer, or geomagnetic field model, with measurement noise below 50 nT. This level of was necessary to adequately sample the local geomagnetic anomaly field. Researchers like Kok *et al.* explored the application of low-cost MEMS magnetometer and IMU sensors for geomagnetic navigation [36]. Their experiment consisted in navigating in the vicinity of a magnetic field generated by a coil using only low-cost MEMS IMU and magnetometer. Since the field generated by a magnetic coil can be analytically modeled with high accuracy, their magnetic navigation solution was capable of obtaining sub-centimeter navigation accuracy when operating in the vicinity of the coil. Li *et al.* developed and tested a geomagnetic navigation solution for pedestrian indoor navigation using low cost MEMS-based IMUs and magnetometers commonly found in consumer cell phones [37]. The strategy was to exploit the abundant magnetic disturbances found in indoor structures and using pedestrian dead reckoning techniques. Their results demonstrated indoor position accuracies of around 10 m. The key to the algorithm accuracy was its ability to mitigate the impact of magnetic matching errors using distance threshold strategies and Adaptive Kalman Filter structures.

Solin *et al.* performed a similar study on the use of cell phone IMU and magnetometer sensors for indoor pedestrian navigation applications in [38]. Their approach

was based on a particle filter framework that fused pedestrian dead reckoning estimates and traditional terrain magnetic matching position estimates (see Section 2.3.3). The proposed system was tested at the Alto University Campus in Espoo after the magnetic field of the area was mapped. The system demonstrated position accuracies of 40 m. The work presented in [36], [37] and [38] demonstrates the usage of low grade MEMS-based sensors for geomagnetic navigation. Their approach relies on the presence of magnetic fields discernable by the low-cost magnetometer sensors. This strategy is feasible for indoor environments where magnetic anomalies are abundant but it is inadequate for navigation using Earth’s magnetic anomaly field, where measurement accuracies within 50 nT are required. The strategy also works because pedestrian dead-reckoning strategies, like step counting, are meant to mitigate the errors from low-cost IMU position estimates. These dead reckoning strategies are not adequate for AUV navigation.

Geomagnetic navigation is a self-contained passive navigation solution with no impact on FV weight or power consumption, and little to no impact on the FV physical layout and has an error characteristic bounded in time. The tradeoffs of this navigation strategy are: its dependance on the existence of magnetic maps, map resolution, obtaining accurate EMF samples, and the cost of a high grade magnetometer and IMU.

Gravity Gradient Navigation

A gravity aiding navigation scheme is similar in operation to geomagnetic navigation aiding. The process consists on correlating a vehicle’s readings of local gravity to a known gravity anomaly map to find the best fit between the sensor readings and a potential position on the map [39]. These position updates are then used to correct INS position errors. This navigation scheme requires a gravimeter and a gravity anomaly map.

The main driver behind gravimeters technology has been natural resource exploration [39]. As a consequence, gravimeters have achieved great sensitivity, 1 part per billions. But due to their sensitivity, gravimeters are susceptible to noise from the environment, including vehicle movement, temperature, magnetic noise, and humidity [40]. To isolate sensor readings from ambient noise gravimeters are mounted on specialized stabilizing platforms located inside controlled environment chambers.

In the simulation work by Zhang, *et al.*, presented and evaluated the performance of a gravity gradient navigation scheme for an AUV [26]. The navigation scheme consisted on using a matching algorithm where the vehicle was deployed and scouted the area for a gravity signature match. Once a good match was located, N-parallel Kalman filters would use a linear model of the local gravity field to sample around the INS location and compare the result to the gravity measurements. The best fit from the filters was then used as the estimate of the vehicle location. The simulation components consisted of INS, gravity gradient maps, and simulated gravimeter outputs. Their simulated navigation system achieved navigation accuracies of 50 m during the course of 40 simulated deployments.

Li, *et al.* performed a simulated study on AUV gravity filter-aided navigation [41], the method is similar to geomagnetic filtering. Their simulation utilized existing gravity anomaly maps measured by satellite with a resolution of 2 mi². To compensate for the low resolution of available gravity anomaly maps, the researchers used fractal interpolation to increase the map resolution and provide a more adequate map for the simulation. The simulation results demonstrated a 400 m navigation accuracy, surpassing the resolution from available gravity anomaly maps.

Shinohara, *et al.* developed an underwater gravimeter enclosure, suitable for mineral deposit exploration, for AUV applications [40]. The implementation utilized a Micro-g LaCoste S-174 gravity sensor. The sensor was mounted on a gimbal mechanism kept stable by fiber optic gyroscopes. Temperature and humidity control systems

were employed to maintain a controlled environment. The final system then was enclosed in a titanium sphere, rated for 4200m of depth. The system was then mounted to the URASHIMA AUV where it scouted the ocean floor. Their work showed the extensive accommodations necessary to prepare a gravimeter for underwater use.

Gravity-aided navigation has the advantages of providing a navigation solution with bounded error without depending on external signals. But the extensive accommodations necessary to employ a gravimeter on a AUV make this an impracticable approach for a low cost navigation solutions.

Terrain Navigation

Traditional terrain navigation is a scheme based on perceptual sensing of distinguishable features in the environment, like landmarks or topography, to estimate AUV position using a map [42]. The main task of terrain navigation systems is the recognition of distinguishable features and estimation of the distance from the recognized feature. Both of these task are non-trivial, on the ocean floor where underwater features do not have predictable patterns nor are they always distinguishable. Similar to other geophysical navigation schemes, terrain navigation depends on the existence a map and resolution. Simultaneous Localization and Mapping (SLAM) is a terrain navigation algorithm that dose not depend on the existence of a maps and reduces the burden of underwater recognition of structures. SLAM focuses on near floor underwater navigation that applies view-based scan matching techniques. By configuring the AUV path to be partially overlapped, the AUV can estimate its relative position by recognizing overlapping feature on its path.

Eustice, *et al.* used a calibrated camera to augment an existing INS and DVL navigation system for a SeaBED AUV [43]. Their methodology complimented the existing navigation scheme with a SLAM navigation system. The result was a navigation system with errors that did not accumulate in time on overlapping paths. By bounding time dependent errors of the INS-DVL navigation system, researchers

increased the operational time of the AUV. They also achieved a navigation accuracy of about 4m in horizontal positioning. The authors noted the importance of lighting for acceptable algorithm performance and the effects it has on the AUV power supply.

Roman (2005) utilized a Doppler bathymetry sensor to develop a SLAM navigation system [42]. The implementation consisted of having the AUV initially scout the deployment area while simultaneously creating a bathymetry map. Once the map was formed, the AUV could successfully navigate the scouted area with errors less than 10 m on the horizontal.

The advantages of terrain navigation include position accuracies below 10 m and error characteristics that do not grow with time. The tradeoffs include: the requirement of an AUV to control its movements via actuators or propellers, and Doppler sensors. If a visual approach is used instead, specialized cameras that must be calibrated and mounted on the vehicle hull. In addition, the vehicle must also carry power for the required cameras and potential lighting sources. For these reasons, terrain navigation is best suited for large scale AUV which posses appropriate payload and/or power capabilities.

3.0.4 Model-Aided Inertial Navigation

In situations where external navigation references cannot be obtained or are not available, researchers have suggested the use of vehicle dynamic models and real-time measurements of environmental factors to aid navigation systems [6] [9]. Dynamic models use external inputs from the environment (currents), or actuator control signals to predict the AUV response. Models are derived from the navigation medium (water) dynamics, the AUV profile, and relevant environmental factors. Model coefficients are extracted from simulation or controlled experiments on the vehicle body or profile. Modeling of vehicle dynamics is not a trivial task, even when considering a rigid body, due to the underlying infinite-dimensional dynamics of the surrounding

fluid [44]. Practical model derivations are made using finite-dimensional approximations and partial differential equations. The basic concept of using a dynamic vehicle model in a navigation system is to treat model outputs as external sensor estimates of velocity, as depicted in Figure 2.1 .

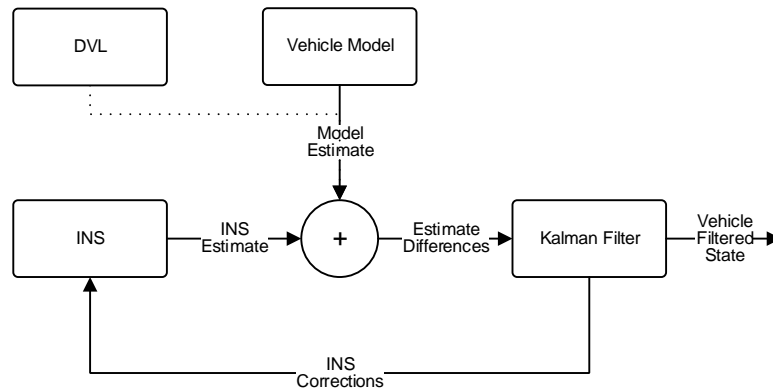


Figure 3.2 : Generic Model Aided INS

Hegreanaes, *et Al.*, reported the methodology used in deriving a dynamic model for the HUGIN 4500 AUV [44]. The derived model was validated using uncorrelated data gathered from a controlled experimental deployment. The test procedure was as follows the AUV was deployed for 60 minutes using USBL for navigation, after which USBL updates were disabled. At this time the AUV operated for 30 minutes utilizing the derived dynamic model as a navigation source. The results showed a maximum of 6 m in position error over 30 min. Further research on the HUGIN AUV dynamic model by Hengreanaes and Hallingstad reported sub-centimeter precision navigation by fusing model-aiding with USBL and DLV data [45]. The team also reported on the long term performance of their vehicle dynamic model and obtained a position error of 20 m in a 119 min deployment.

Montgomery and Polzin developed a dynamic model for a profiling FV in order to obtain accurate estimates of surrounding water current during descent and ascent [9]. The model was developed in an effort to improve current meter estimates since

these are designed as Eulerian instruments. Researchers derived a model empirically based on the AUV cylindrical profile and mass distribution. The AUV was then fitted with a three axis accelerometer to estimate the accelerations exerted on it during deployments. With the model and accelerations, the researchers were able to obtain improved accuracy on current estimates by factoring out the profiling vehicle's dynamics.

Schmidt and Siegel (2011) reported on an FV descent dynamics during a 8350 m descent on the Puerto Rico Trench [46]. The FV payload was an Aquadopp DW acoustic-Doppler current meter (ADCM), with onboard compass and pressure meter. The ADCM's heading data showed a continuous counter clock wise rotation during the whole descent, with an average rotation rate of 0.029 s^{-1} . The pressure data showed a decreasing trend of FV descent velocity, from about 0.94 m/s at the surface to about 0.87 m/s at the trench floor. The horizontal current measurements, which include ambient current plus the FV horizontal displacement and rotation dynamics, were used to analyze the FV horizontal displacement. A peak in the horizontal current data of 8 cm/s was observed during the FV descent and a peak ambient current of 5 cm/s was measured at the trench floor. By integrating the horizontal current data with respect to time the authors estimated the horizontal displacement of the FV with respect to the deployment location (a from of doppler navigation). The landing location was estimated to be within 30 m of the deployment location and the descent trajectory exhibited a spiral-like nature. The authors noted that the nature of the descent was mostly due to the FV geometry and fluid dynamics rather than ambient current or Coriolis deflection. A challenge of of using ADCM at abyssal or hadal depths is the reduction in the availability of scatter material. Lower levels of scatter material decreases the instruments current measurement accuracy and can even introduce biases. The ADCM was demonstrated to operate with low bias and measurement accuracies of 4 cm/s standard deviation (STD) in ambient where the

signal to noise ratio (SNR) is 6 [47]. SNRs of 6 or greater were observed for depth of 7000m or less (most of the descent), only measurement at greater depth might have suffered from low SNR problems. Unfortunately only data of the vehicle’s descent was available for analysis. Although this research did not derive any dynamic models for the FV, it remains one of the only studies made on FV dynamics and data from it was used in this research effort.

In the implementations previously mentioned, the vehicle profiles are relatively smooth and simple (cylindrical), greatly simplifying the modeling of vehicle dynamics. This limits the development of dynamic models for vehicles with rough or variable profiles as they present a greater challenge in determining model parameters. Vehicle dynamics are highly dependent on environmental factors such as currents, so for prolonged operation these factors have to be either measured or estimated accurately. This can be achieved with little impact on vehicle weight and profile by measuring ocean currents indirectly using electromagnetic techniques [48] [49]. But the creation of a vehicle dynamic model remains the most challenging aspect of model-aided INS.

3.1 Inertial Navigation Aiding Scheme Summary

Table 3.1 summarizes the AUV navigation schemes reviewed and their relevant impact on AUV characteristics. Most of the navigation schemes discussed in the proceeding section were designed to be used on large underwater vehicles. These usually have less stringent constraints on final weight, cost and physical layout. Furthermore none of the strategies have been implemented or designed in a FV.

Most of the navigation schemes discussed in the proceeding sections were also designed to work in real-time on the AUV embedded processor. Algorithms required to execute in real-time on embedded systems have certain constraints: execution power, run time, program memory, and random access memory memory. These constraints on algorithm implementation sometime result in the implementation of the algorithm with degraded performance. Based on the recent developments in the

field of underwater navigation presented in this Chapter, there is still a need for a low-cost navigation solution that meets the payload, power, cost and physical constraints of a FV.

The constrained and tightly coupled environment of embedded systems generally results in inflexible, suboptimal, algorithm implementations. Thus with the objective of developing a single tool for a variety of navigation tasks Gade *et al.*, developed a post-processing navigation solution, called NavLab [50]. The tool was developed to produce optimal estimates of position, increasing its accuracy and integrity. Improved estimates of position are obtained by using a optimal smoothing of the navigation system outputs. Optimal smoothing produces statistically optimal estimations by considering both past and future measurements. The flexibility of the NavLab platform results from its two components: a simulator and a estimator. The simulator outputs a set of simulated sensor measurement based on a given trajectory and a list of desired sensors. The estimator is a flexible navigation system that produces filtered and smoothed optimal estimates of position, velocity and orientation; based on available measurements. NavLab has been used to post-process navigation data for the HUGIN AUV [24]. NavLab post-processed estimates of position reduced navigation errors by 50% when compared the real-time estimates produced by the AUV.

Table 3.1 : Summary of AUV navigation schemes

Navigation Scheme	Implementaiton	Weight	Error Characteristics	Costs	Payload Requirements
Acoustic Navigation	LBL [8]	AUV's transducer	Bounded	- AUV' stransducer - Beacon framework - Framework deployment	AUV's transducer
	USBL [8]	AUV's transducer	Bounded	- AUV's transducer - Ship's positioning system - Ship's transceiver	AUV's transducer
Doppler Navigation	DVL [22] [24] [46]	DVL Sensor	Time Dependent	- DVL - GPS	DVL sensor
	Magnetic [19] [14]	Compass	Bounded	Compass	N/A
Geophysical Navigation	Gravity [26]- [41]	Gravimeter	Bounded	- Gravimeter - Stationary platform	- Stationary Platform
	Terrain Doppler [43]	Topography Doppler sensor	Bounded	Topography Doppler sensor	Topography sensor
	Terrain visual [42]	- Camera - Lighting equipment	Bounded	- Camera - Lighting equipment	- Camera - Lighting equipment
Model Aided Navigation	Dynamic model [9] [44] [45]	N/A	Time dependent	Model development	N/A

Chapter 4

Problem Statement & Hypothesis

Conventional aiding schemes used for underwater navigation are comprised of an inertial navigation systems (INS), magnetic compass, pressure sensors and some form of negative feedback on the vehicle navigation state. [7]. Popular aiding methods used today include Doppler velocity logs, current meters, and acoustic beacons. But cost constraints, weight limitations, and payload capabilities in a low-cost FV render most of these solutions unfeasible. Thus, the problem being addressed in this thesis is that of how to develop a position tracking system able to satisfy the cost, weight, and payload capability constraints within the FV physical limitations.

Our research question is: *Can we develop a low cost, self-contained navigation solution with satisfactory accuracy that does not hinder the payload capabilities of a free vehicle?*

Our hypothesis is: A post processing navigation framework based on geomagnetic aiding can provide a low-cost trajectory estimate solution with acceptable accuracy without having a significant impact on the vehicle's payload capabilities while minimizing costs.

Chapter 5

Objectives

5.1 General Objectives

The main objective perused in this project is developing a post processing inertial navigation framework based on geomagnetic data capable of simulating vehicle deployments, estimate navigation performance, and process low-cost FV sensor information to estimate trajectory and bottom location after deployment.

5.2 Specific Objectives

- To develop a descent and ascent trajectory simulator for FV.
- To simulate non-ideal sensor outputs for accelerometer, gyroscope, magnetometer and pressure gauge devices.
- To develop a post processing INS computer with geomagnetic-aiding and an algorithm capable of combining both position estimates from INS and geomagnetic data.
- To assess sensor parameters for the accelerometer, gyroscope, and magnetometer that have a significant effect on navigation performance.
- To recommend accelerometer, gyroscope, pressure, and magnetometer sensors able to satisfy that navigation parameters determined and integrate them into the FV.
- Analysis of the effect that FV dynamics have on the navigation strategies presented.

Chapter 6

Methodology

This chapter starts by presenting a system diagram of the implemented post-processing navigation systems, in Section 6.1. The following sections then proceed to present the implementation details of every composing block in the system diagram. Finally, the chapter concludes by presenting the test cases used to verify and validate the post-processing navigation system.

6.1 System Overview

Figure 6.2 shows a block diagram of the proposed post-processing geomagnetic navigation system. The system can be separated into three layers based on the roles of the composing blocks: the sensor layer, the data processing layer and the data fusion layer. The sensor layer, composed of a three-axis accelerometer, three-axis gyroscope, three-axis magnetometer, pressure sensor, and geomagnetic anomaly maps. The benefit of establishing this layer is that data provided by each sensor can be either obtained from a sensor log or simulated sensor outputs based on sensor models. Having the flexibility of using real or simulated sensor data enables the possibility of evaluating system performance under different circumstances or different sensor performance models, in addition to providing a navigation solution for actual FV deployments. The data processing layer is composed by an inertial navigation computer (INC) and a geomagnetic computer (GC). The INC uses the outputs from the accelerometer and gyroscope to solve Equations 2.9, 2.15, and 2.16 to produce an estimate of system state. The GC processes magnetometer readings and correlates

them to a location on the geomagnetic map, as discussed in Section 2.3, to produce an estimate of the vehicle position. The estimation layer is solely composed of estimators, responsible of combining the INS and GC output to produce an estimate of the system state. The state output from the estimator is returned to the INC to correct for accumulated errors.

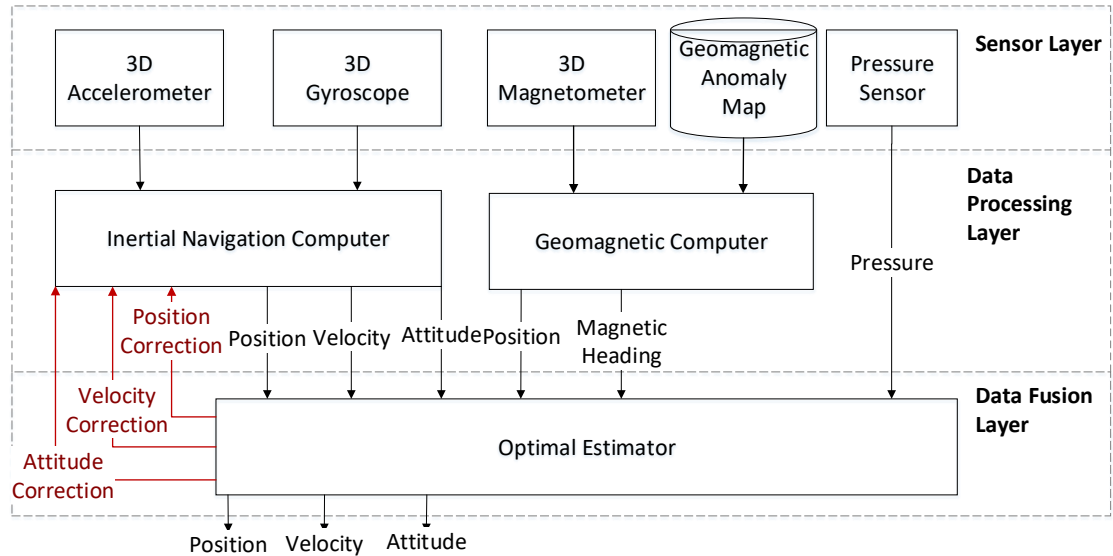


Figure 6.1 : System diagram of the post-processing navigation system

6.2 Trajectory Generator

The objective of the FV trajectory generator is to simulate the vehicle trajectory when deployed. The trajectory is described by a sequence of periodic vehicle positions, velocities, and accelerations with respect to the n-frame. The FV attitude during the trajectory is described by a sequence of periodic quaternions, attitude is described with respect to the n-frame. The trajectory generator is based on observed FV dynamics during multiple deployments. The expected FV dynamics are: a constant terminal descent and ascent velocities of about 1 m/s, a vertical rotation rate of about 4.17^{-3} revolutions/min and a random horizontal displacement of around 10m north or east, for every 1000s of descent or ascent [51]. The FV dynamics are then

divided and modeled in three areas: vertical displacement, horizontal displacement, and vehicle attitude.

The FV vertical displacement was simulated based on a constant vertical velocity model in Equation 6.1. This exponential behavior of the model is meant to simulate the rate at which the terminal velocities are reached.

$$v_d(t) = \begin{cases} V_{DES}(1 - e^{-\frac{t}{\tau_{DES}}}), & \text{if } 0 \leq t < t_{LND} \\ V_{DES}e^{-\frac{t}{\tau_{LND}}}, & \text{if } t_{LND} \leq t < t_{REL} \\ -V_{ASC}(1 - e^{-\frac{t}{\tau_{ASC}}}), & \text{if } t_{REL} \leq t < t_{END}, \end{cases} \quad (6.1)$$

where t_{LND} , t_{REL} , and t_{END} refer to the time instances when the vehicle landed, released its ballast, and surfaced, respectively. V_{DES} and V_{ASC} are the user specified terminal velocities for the descent and ascent of the FV. τ_{DES} , τ_{LND} , and τ_{ASC} are user specified quantities. τ_{DES} controls the rate at which the FV accelerates up to V_{DES} when deployed. τ_{LND} controls the rate at which the FV decelerates to a stop when it lands on the ocean floor. τ_{ASC} controls the rate at which the FV accelerates to V_{ASC} when it releases its ballast.

Modeling vehicle accelerations with exponential models is not ideal, but since the dynamics of these events are short lived, replacing them with a more accurate acceleration model would not have much effect on the final FV vertical displacement. Finally, the FV vertical velocity estimate, $V_d(t)$, is numerically integrated and derived to simulate the FV depth and vertical acceleration.

Since the north and east displacements of the FV are random, we chose to model them as a random walks in both directions. The model is presented below:

$$r_{N,k} = r_{N,k-1} + stp_N \quad \text{where } stp_N \text{ is } N(0, \sigma_N^2) \quad (6.2)$$

$$r_{E,k} = r_{E,k-1} + stp_E \quad \text{where } stp_E \text{ is } N(0, \sigma_E^2) \quad (6.3)$$

$r_{N,k}$ and $r_{E,k}$ are the north and east displacements for the time instance t_k , in meters. $r_{N,k-1}$ and $r_{E,k-1}$ are the north and east displacement from the previous time step, stp_N and stp_E are the independent steps taken each time step in the north and east directions respectively, and σ_N^2 and σ_E^2 are user specified variances of the Gaussian distributions from which the steps are sampled.

The random walk sequences $r_{N,k}$ and $r_{E,k}$ are then numerically differentiated twice, once for estimating the vehicle horizontal velocities (m/s) and the second time to estimate the vehicle accelerations (m/s^2). Both horizontal velocities and accelerations are given with respect to the n-frame. Finally, $r_{N,k}$ and $r_{E,k}$ are converted to displacements in latitude and longitude and added to the FV initial position, specified by the user, using the following equations:

$$Lat_k = \left(\frac{r_{N,k}}{R - d_k} \right) \left(\frac{180}{\pi} \right) + Lat_0 \quad (6.4)$$

$$Lon_k = \left(\frac{r_{E,k}}{(R - d_k) \cos(Lat_k)} \right) \left(\frac{180}{\pi} \right) + Lon_0 \quad (6.5)$$

where Lat_k and Lon_k are the estimated latitude and longitude for times step k ; Lat_0 and Lon_0 are the FV initial n-frame position coordinates; $R = 6378137.0m$ and represents the radius of the Earth; d_k is the simulated depth of the vehicle for time step k .

The FV attitude with respect to the n-frame is simulated based on the vehicle observed vertical rotation rate. The output quaternions are created using the inertial attitude computer, with the body rates set to:

$$\omega_{nb}^b(t) = \begin{cases} [0 \ 0 \ \omega_{z,DES}]^T, & \text{if } 0 \leq t < t_{LND} \\ [0 \ 0 \ 0]^T, & \text{if } t_{LND} \leq t < t_{REL} \\ [0 \ 0 \ \omega_{z,ASC}]^T, & \text{otherwise;} \end{cases} \quad (6.6)$$

where $\omega_{z,DES}$ and $\omega_{z,ASC}$ are user specified constant vertical rotation rate for the FV descent and ascent. The FV is assumed to be aligned with the n-frame at the start of the trajectory simulation.

The FV trajectory simulator was implemented as a Matlab function with the following signature $[SysPathDescript\ q] = FVTrajectorySim(PathParams)$. *PathParams* is a compound structure of the control parameters used for each of the FV dynamic models, that together simulate the FV trajectory. The *PathParams* structure has the following members:

- *InitialCond*: is structure containing the initial latitude, longitude and depth where the FV was deployed. Initial velocities and accelerations are assumed to be zero. The members of the structure are:
 - *Lat*: initial FV latitude in degrees.
 - *Lon*: initial FV longitude in degrees.
 - *d*: initial FV depth in meters.
- *TimingParams*: is a structure containing the timing parameter used to create the output time series trajectory description *SysPathDescript*. The structure also contains the timing parameters used for trajectory models. The members of the structure are:
 - *samp_p*: represents the sampling period used to describe the FV trajectory, in seconds.
 - *start_t*: represents the start time for the simulation, in Matlab *datenum* format.
 - *lnd_t*: represents the relative time instant, in seconds, after *start_t* when the vehicle lands.
 - *res_t*: represents the relative time instant, in seconds, after *lnd_t* when the vehicle releases its ballast.

Note that no end time for the simulation is provided, t_{END} this is estimated based on distance traveled in the descent and terminal ascend velocity.

- *VerticalParams*: is a structure that contains the control parameters of the vertical displacement model, Equation 6.1. The structure contains members:
 - *des_v*: specified m/s, it represents the terminal descent velocity V_{DES} .
 - *asc_v*: specified m/s, it represents the terminal ascent velocity V_{ASC} .
 - *tau_des*: specified s, represents τ_{DES} .
 - *tau_lnd*: specified s, represents τ_{LND} .
 - *tau_res*: specified s, represents τ_{ASC} .
- *HorizontalRW*: is a structure that contains the control parameters for the horizontal displacement model, Equation 6.2. The structure has the following members:
 - *var_n*: represents σ_N^2 in the model.
 - *var_e*: represents σ_E^2 in the model.
- *Att*: is a structure that contains the control parameters for the attitude model in Equation 6.6. Att structure has the following members:
 - *w_des*: specified in 1/s, represents $\omega_{z,DES}$.
 - *w_asc*: specified in 1/s, represents $\omega_{z,ASC}$.

SysPathDescript is a time series collection that describes the simulated FV trajectory, with the following members:

- *FVPos*: is a time series object that describes the FV position in the n-frame, with the form $[Latitude\ Longitude\ Depth]^T$.
- *FVVel*: is a time series object that describes the FV velocity with respect to the n-frame with the form $[V_N\ V_E\ V_d]^T$ in *m/s*
- *FVAcc*: is a time series object that describes the FV acceleration with respect to the n-frame, with the form $[a_N\ a_E\ a_D]^T$.
- *FVAcc_b*: is a time series object that describes the FV accelerations with respect to the body frame $[a_X\ a_Y\ a_Z]^T$. This time series is estimated by projecting the acceleration on the n-frame to the b-frame using the FV simulated attitude. It represents the ideal accelerations exerted on the onboard accelerometer.

q is a time series object of the quaternion that describes the vehicles attitude with respect to the n-frame in time.

6.3 Sensor Models

As mentioned in Section 2.1.6, inertial sensors measurements are corrupted by multiple sources. Common sensor models use to simulate sensor output include a constant bias error component, a moving bias error component and a source of random noise [1], [5], [32], [52]. These error sources are added to ideal sensor readings to simulate gyroscope and accelerometer sensor outputs. The constant bias error is simulated by adding a constant offset to the ideal sensor readings. A moving bias is simulated by a first order gauss Markov process (FOGMP) [52]. Finally the random noise is simulated by white Gaussian noise. Thus the sensor model used to for accelerometer readings was:

$$f = f_{ideal} + b_a + \omega_a + c_a \quad (6.7)$$

Where $f = [f_x \ f_y \ f_z]^T$ is the resulting simulated specific force output from a three axis accelerometer. $f_{ideal} = [f_{x,ideal} \ f_{y,ideal} \ f_{z,ideal}]^T$ is the ideal specific forced sampled by on a three axis accelerometer. $\omega_a = [\omega_{x,a} \ \omega_{y,a} \ \omega_{z,a}]^T$ is a vector of white Gaussian noise. $c_a = [c_{x,a} \ c_{y,a} \ c_{z,a}]^T$ is constant value vector that simulates a constant bias on the sensor readings

The sensor model for the gyroscope is identical to accelerometer model and is given by:

$$g = g_{ideal} + b_g + \omega_g + c_g \quad (6.8)$$

The sensor models were implemented as a Matlab function with the following signature: $[s_sim] = IMUSenseMdl(s, SensParams)$. Here s is a $3 \times m$ matrix where each column is an ideal sample from a three axis sensor. Each column is assumed to have the form $[s_x \ s_y \ s_z]^T$, where s_x , s_y and s_z represent ideal sensor samples form

the x , y , and z axis of the sensors. *SensParams* is a structure that contains the parameters for the sensor model and has the following members:

- *samp_p*: a scalar value that represents the sampling period of the data in s , in seconds.
- *fogm_tau*: is a 3×1 vector, representing time constant for the FOGMP, in seconds.
- *fogm_std*: is a 3×1 vector, representing the standard deviation the Gaussian noise that drives the FOGMP of each axis.
- *fogm_init*: is a 3×1 vector, representing the initial values for the FOGMP.
- *omega_std*: is a 3×1 vector, representing the standard deviation for the white Gaussian noise source ω_a or ω_g .

s_sim is a $3 \times m$ matrix representing the simulated sensor output, where each column represents a three axis sensor sample.

6.4 Inertial Navigation Computer

This section presents the implementation of the INS attitude and position computer. Both implementations are based on the INS theoretical background presented in Chapter 2. The following section presents the implementation of the intertidal attitude computer and Section 6.4.2 presents the implementation of the inertial position computer.

6.4.1 Inertial Attitude Computer

The inertial attitude computer, which estimates the attitude of the b-frame with respect to the n-frame, was implemented as a Matlab function. The functions approximates the solution to Equation 2.9 using Euler's Method, as in Equation 6.9.

$$q_{b,\omega,t_k}^n = q_{b,t_{k-1}}^n + \Delta t \dot{q}_{b,\omega,t_k}^n \quad (6.9)$$

where:

- q_{b,ω,t_k}^n is the inertial attitude estimate for the time instant t_k

- $q_{b,t_{k-1}}^n$ is the attitude estimate from the previous time step t_{k-1}
- q_{b,ω,t_k}^n is a vector quaternion created using the body rate angular velocity vector provided by the onboard gyroscope for the current time instant $\omega_{nb,k-1}^b$
- $\Delta t = t_k - t_{k-1}$ is the period between estimation cycles

The Inertial Attitude Computer is implemented as a Matlab function, with the following signature $[q_pred] = Qpred(q_prev, w, dt)$, where q_prev represents the $q_{b,t_{k-1}}^n$, the parameter w represents $\omega_{nb,k}^b$, and dt is Δt in Equation 6.9.

6.4.2 Inertial Position Computer

The inertial position computer, estimates the vehicles velocity and position with respect to the n-frame, was implemented as a Matlab function. The functions approximates the solution to Equations 2.15 and 2.16 using Euler's Method as in Equations XX and YY respectively.

$$v_{e,t_k}^n = v_{e,t_{k-1}}^n + \Delta t \dot{v}_{e,t_{k-1}}^n \quad (6.10)$$

$$r_{t_k}^n = r_{t_{k-1}}^n + \Delta t \dot{r}_{t_{k-1}}^n \quad (6.11)$$

where

- v_{e,t_k}^n is the inertial velocity estimate for time instant t_k
- $v_{e,t_{k-1}}^n$ is the velocity estimate from the previous time step t_{k-1}
- \dot{v}_{e,t_k}^n is the evaluation of Equation 2.15 using data from the accelerometer, initial velocity estimates from t_{k-1}
- $\Delta t = t_k - t_{k-1}$ is the period between estimation cycles
- $r_{t_k}^n$ is the inertial position estimate for t_k
- $r_{t_{k-1}}^n$ is the position estimate from t_{k-1}
- $\dot{r}_{t_{k-1}}^n$ is the evaluation of Equation 2.16 using the $v_{e,t_{k-1}}^n$.

The initial position computer function has the following signature, $[ins_st] = IN-NavEq(prev_ins_st, f, gl, dt)$ where:

6.5 Magnetic Computer

The geomagnetic navigation algorithm used for the FV post-processing navigation system was based on a modified magnetic matching algorithm presented in Section 2.3.3. Because the FV horizontal displacements are not expected to be very large [46], instead of using a track of magnetic samples, the algorithm uses a single magnetic sample when the magnetic measurement period expires. The implementation of the magnetic matching algorithm is specified in the measurement update section of the position optimal estimator, Section 6.6.2, because of the way in which the optimal estimator produces its results.

6.6 State Estimators

6.6.1 Attitude Estimator

A complementary filter was chosen as the estimation technique to fuse the attitude measurements from the attitude computer, accelerometer, and magnetometer into the system attitude estimate. A complementary filter was chosen because of its simpler structure and compelling results when compared to other attitude estimation alternatives, like the kalman filter and the extended kalman filter [3].

The Complementary Filter and Its Applications in Attitude Estimation

The complementary filter is a simple estimation technique used to combine measurements of a state of interest [53]. Figure 6.2 shows the basic structure of a complementary filter, where X and Y are noisy measurements of a state Z , and \hat{Z} is the filter estimate of Z . Assuming that the noise in X is mostly low frequency, the noise in Y is mostly high frequency, and the cut-off frequency for both filters in Figure 6.2 is the same then, \hat{Z} would, in theory, be a noise free, all pass, estimate of Z . Note that no statistical description of the noise corrupting the measurements X or Y , is considered in the complementary filter, only a simple analysis in the frequency

domain [53]. Figure 6.2 (B) depicts an alternate mechanization of the complementary filter. In this form, the complementary filter operates on the difference between the measurements $Y - X$ and the filter is chosen based on the frequency spectrum of $X - Y$.

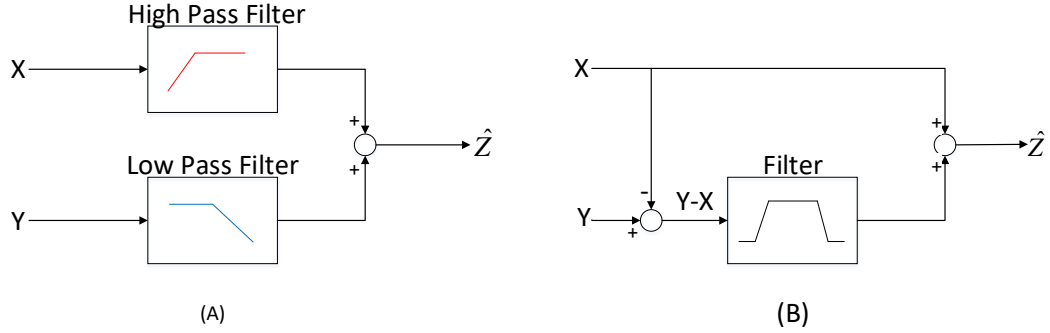


Figure 6.2 : (A) The basic structure of a complementary filter. (B) Alternate mechanization of the complementary filter.

In estimating attitude from an IMU and a magnetometer, the complementary filter is implemented to be a high-pass filter on the attitude estimates from the attitude computer and a low-pass filter on the attitude derived from accelerometer and magnetometer readings. A high-pass filter is applied to gyroscopic estimates of attitude because of the slow bias variations in its measurements which, once integrated, become the main cause of gyroscopic attitude estimate drift [5]. Because accelerometer and magnetometer measurements are not integrated with respect to time, the primary source of error in their measurements is the high-frequency electromechanical noise from the sensors. For this reason, attitude estimates derived from accelerometer and magnetometer measurements are low-pass filtered. Care must be taken when selecting the cut-off frequency for the complementary filter, as it is the scale by which the filter assigns weight on its input measurements. An initial selection is usually based on sensor performance parameters and expected system dynamics but final values are most commonly found by experimentation [3]. A final note on estimating attitude from, IMU sensors, is the effect of external accelerations and perturbing

magnetic fields, as these sway our estimates of local vertical and north headings. If these dynamics are short-lived their effects are mitigated by the low-pass filtering but they must be considered if their presence is persistent.

Complementary Filter Mechanization

The implementation of the attitude complementary filter is based on the work presented by Valenti, *et al.*, in [3]. Figure 6.3 shows a system diagram of the implemented complementary filter. The process starts by obtaining an estimate of the systems attitude from the inertial attitude computer $q_{b,\omega}^n$ (t_k omitted for clarity). a^b is the accelerometer output, assumed to be a measurement of the n-frame vertical axis in the body frame. a^b is normalized and projected onto the n-frame using $q_{b,\omega}^n$ via Equation 2.8. The result is an estimate of the direction of n-frame z-axis or local vertical, g^m . g^m is then compared to the expected direction of the local vertical $g^n = [0\ 0\ 1]^T$ and the difference between the two is used to calculate Δq_{vert} . Δq_{vert} is the correction in pitch and roll angles of $q_{b,\omega}^n$. Note that Δq_{vert} provides no correction in yaw. This is expected because the direction of local vertical provides an estimate of the horizontal North-East plane of the n-frame but no information of its yaw orientation [3]. Δq_{vert} suffers from high frequency noise emerging from a^b , thus a low-pass filter is applied to the estimate, producing $\Delta q'_{vert}$. Section 6.6.1 specifies the details related to the formulation and filtering of Δq_{vert} . $\Delta q'_{vert}$ is then applied to $q_{b,\omega}^n$, via quaternion product $q_b^m = \Delta q'_{vert} \otimes q_{b,\omega}^n$. Resulting in a estimate of system attitude, corrected for divergence in global horizontal plane q_b^m .

q_b^m is then used to project the measurements from the magnetometer, m^b , onto the n-frame to obtain a predicted magnetic heading h^m . h^m is then compared to the n-frame's half North-Down-plane, where the North axis is positive, to obtain a heading quaternion correction, Δq_{yaw} with respect to the local magnetic north. Δq_{yaw} is then filtered with a low-pass filter to produce $\Delta q'_{yaw}$. The process of calculating and filtering of Δq_{yaw} is presented in Section 6.6.1. $\Delta q'_{yaw}$ is then applied to q_b^m , via

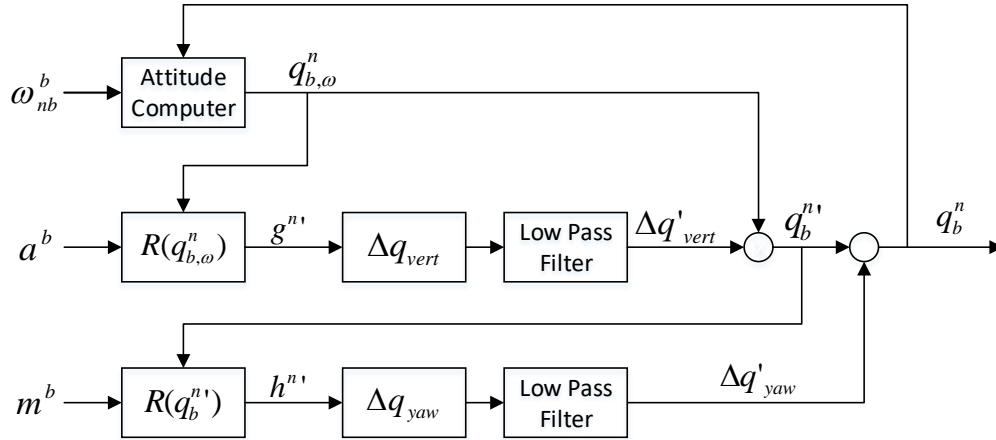


Figure 6.3 : System diagram of the attitude complementary filter

quaternion product, to obtain the final estimate of vehicle orientation q_b^n corrected for drifts in the roll, pitch, and yaw. The final step involves feeding back q_b^n to the attitude computer as the estimate of vehicle orientation of the previous time step.

Estimation and Filtering of Δq_{vert} : In this section we present the formulation of q_{vert} , the formulation is derived from the work by Valenti, *et al.*, in [3]. First an estimate of the local vertical $g^{n'}$ is obtained using $q_{b,w}^n$ and a^b via Equation 6.12

$$R(q_{b,w}^n)a^b = g^{n'} \quad (6.12)$$

Since $g^{n'}$ will diverge from the local vertical g^n by a small amount, Δq_{vert} is the attitude correction that will rotate $g^{n'}$ into g^n . Δq_{vert} is calculated by solving Equation 6.13

$$R^T(\Delta q_{vert})g^{n'} = g^n, \quad (6.13)$$

where

$$g^{n'} = [g_x \ g_y \ g_z]^T, \quad g^n = [0 \ 0 \ 1]^T$$

The solution to Equation 6.13 is presented below, [3]

$$q_{vert} = \left[\sqrt{\frac{g_z+1}{2}} \quad \frac{g_y}{\sqrt{2(g_z+1)}} \quad -\frac{g_x}{\sqrt{2(g_z+1)}} \quad 0 \right]^T \quad (6.14)$$

As mentioned before q_{vert} is affected by the high frequency noise in a^b , thus it is scaled down (or low-pass filtered) before being applied to $q_{b,w}^n$. The scaling of q_{vert} is done by spherical linear interpolation (SLERP) [54] between q_{vert} and the identity quaternion $q_I = [1 \ 0 \ 0 \ 0]^T$, via the following Equation: [3]

$$\Delta q_{vert} = \frac{\sin([1 - \alpha]\theta)}{\sin(\theta)} q_I + \frac{\sin(\alpha\theta)}{\sin(\theta)} \Delta q_{vert} \quad (6.15)$$

where θ is the angle between q_I and q_{vert} , estimated by calculating the dot product of both quaternions. $\alpha \in [0, 1]$ is the gain that characterized the cut-off frequency of the filter.

Finally the $q_{b,w}^n$ is multiplied by Δq_{vert} resulting in q_b^m , an attitude estimate corrected for drifts in the roll and pitch components:

$$q_b^m = \Delta q'_{vert} \otimes q_b^n \quad (6.16)$$

Estimation and Filtering of q_{yaw} . q_{yaw} is derived from the magnetic heading provided by the on-board magnetometer and provides q_b^m with drift corrections in the yaw component. The formulation and filtering of q_{yaw} is similar to Δq_{vert} and is also based on the work of Valenti, *et al.*, [3]. The process begins by first normalizing the measurement from the magnetometer m^b then transforming its representation from the b-frame m^b to the n-frame, with q_b^m , as follows:

$$R(q_b^m) m^b = h^m \quad (6.17)$$

h^m estimates the direction of the local magnetic north. Next, q_{yaw} is calculated as the rotation needed to place h^m in the half-plane formed by the n-frame magnetic north and local vertical, where the resulting vector is pointing in the positive north

direction. The formulation of q_{yaw} is presented in Equation 6.18 [3].

$$R(\Delta q_{yaw}) \begin{bmatrix} h_x \\ h_y \\ h_z \end{bmatrix} = \begin{bmatrix} \sqrt{h_x^2 + h_y^2} \\ 0 \\ l_z \end{bmatrix} \quad (6.18)$$

Note that Equation 6.18 represents a rotation about the global z-axis and aligns the horizontal components of h^b to the positive magnetic north direction. The benefit of this formulation is that the components of pitch are not affected by any perturbations that might be present in m^b , limiting their influence to the yaw angle only [3]. Based on the above discussion Δq_{yaw} will have the following form:

$$\Delta q_{yaw} = \begin{bmatrix} q_{0yaw} & 0 & 0 & q_{3yaw} \end{bmatrix}^T \quad (6.19)$$

which represents a rotation about the z-axis.

The solution to Equation 6.19 is given below [3]:

$$\Delta q_{yaw} = \begin{bmatrix} \frac{\sqrt{T+h_x\sqrt{T}}}{\sqrt{2T}} & 0 & 0 & -\frac{h_y}{\sqrt{2}\sqrt{T+h_x\sqrt{T}}} \end{bmatrix} \quad (6.20)$$

where

$$T = h_x^2 + h_y^2 \quad (6.21)$$

As with Δq_{vert} , Δq_{yaw} is affected by the high frequency noise of the magnetometer measurements m^b . Thus a similar filtering procedure as with Δq_{vert} was adopted for Δq_{yaw} . Since each Δq_{vert} and Δq_{yaw} are independent and each is related to a particular sensor (accelerometer or magnetometer) they may be affected by noise with different frequency spectrums. The complementary filter mechanization used allows for different gains to be assigned to the filters of Δq_{vert} and Δq_{yaw} such that they are tuned to the noise frequency spectrum their corresponding sensor. Thus the filtering of Δq_{vert} was the same as for the SLERP in Equations 6.15 but the gain α is replaced by a second gain β . Finally the output of the filter was obtained by applying

the Δq_{yaw} correction to q_b^m via equation 6.22

$$q_b^n = \Delta q'_{yaw} \otimes q_b^m; \quad (6.22)$$

Attitude Quaternion Initialization

As mentioned in Chapter 2.1 attitude inertial estimates depend on known initial conditions. This subsection explains how the attitude quaternions q_b^n were initialized. The process was proposed by Valenti, *et al.*, [3] and uses the orientation estimates from the accelerometer and magnetometer to estimate the initial attitude of the system $q_{b,0}^n$. First $q_{b,0}^n$ is decomposed into two auxiliary quaternions $q_{vert,0}$ and $q_{yaw,0}$:

$$q_{b,0}^n = q_{yaw,0} \otimes q_{vert,0} \quad (6.23)$$

where $q_{vert,0}$ is calculated via Equation 6.24

$$q_{vert,0} = \begin{cases} \left[\begin{array}{cccc} \sqrt{\frac{a_z+1}{2}} & \frac{a_y}{\sqrt{2(a_z+1)}} & -\frac{a_x}{\sqrt{2(a_z+1)}} & 0 \end{array} \right]^T, & a_x \geq 0 \\ \left[\begin{array}{cccc} -\frac{a_y}{\sqrt{2(1-a_z)}} & \sqrt{\frac{1-a_z}{2}} & 0 & -\frac{a_x}{\sqrt{2(1-a_z)}} \end{array} \right]^T, & a_x < 0. \end{cases} \quad (6.24)$$

$q_{yaw,0}$ is estimated by first projecting the normalized magnetometer estimates of north heading onto the horizontal n-frame (with arbitrary yaw) via Equation 2.12, resulting in l . l is then used in Equation 6.25 to estimate $q_{yaw,0}$ as:

$$q_{yaw,0} = \begin{cases} \left[\begin{array}{cccc} \frac{\sqrt{T+l_x\sqrt{T}}}{2T} & 0 & 0 & -\frac{l_y}{\sqrt{2}\sqrt{T+l_x\sqrt{T}}} \end{array} \right]^T, & l_x \geq 0 \\ \left[\begin{array}{cccc} \frac{l_y}{\sqrt{2}\sqrt{T+l_x\sqrt{T}}} & 0 & 0 & -\frac{\sqrt{T+l_x\sqrt{T}}}{2T} \end{array} \right]^T, & l_x < 0. \end{cases} \quad (6.25)$$

Note the Equations 6.24 and 6.25 are similar to Equations 6.14 and 6.20 presented earlier. Equation 6.24 is an augmented version of Equation 6.14 that avoids the singularity event when $ax = -1$. In a similar fashion Equation 6.25 is an augmented version of Equation 6.20 that avoids the singularity event when lx is negative and

$ly = 0$. Now that $q_{vert,0}$ and $q_{yaw,0}$ are calculated, $q_{b,0}^n$ can be estimated using Equation 6.23.

Complementary Filter: Matlab Implementation

The attitude complementary filter was implemented in Matlab as a set of functions. The function signatures along with a description for each function is provided below:

- $[q_pred] = Qpred(q_prev, w, dt)$: computes the attitude estimate from the inertial attitude computer, see Section 6.4.1.
- $[q_corr] = QaccCorrect(q_pred, a)$: estimates Δq_{vert} via Equation 6.14, where q_pred is $q_{b,\omega}^n$ and a is the accelerometer read out.
- $[q] = QyawCorrect(q_corr, m)$: estimates Δq_{yaw} via Equation 6.20, where q_corr is q_b^m and m is m^b of Equation 6.17.
- $[q] = ScaleQuat(q, gain)$: scales the quaternion q via Equation 6.15, where $gain$ represents α .
- $[q] = Qinit(a, m)$: estimates the vehicles initial attitude $q_{b,0}^n$ via Equations 6.23, 6.24, and 6.25. Where a is a in Equation 6.24, m is magnetometer's estimate of magnetic north, and the output q is $q_{b,0}^n$

6.6.2 Position Estimator

The particle filter was chosen as the estimator for the vehicle position because it does not impose a linearity restriction on the systems models and no restriction on the error characteristics in either the system or measurement updates, providing a flexible framework for this research and any future enhancements. As mentioned in Section 6.1, the FV depth estimate is based on measurement updates from a pressure sensor. The horizontal position estimate was derived from the magnetic matching algorithms. For this reason the position estimator for the vehicle was divided into two filters, a depth particle filter (DPF) and a horizontal position particle filter (HPPF).

The remaining subsections provide a brief introduction to the particle filter (Section 6.6.2), the implementation of the DPF (Section 6.6.2), and the implementation of the HPPF (Section 6.6.2).

Particle Filter Introduction

The goal of a particle filter is to estimate the state of a system as it evolves over time. A particle filter describes the system state as a changing probability distribution (pdf) function based on available information [55]. In lieu of an analytical expression, the particle filter describes the state-pdf with a set of samples taken from the distribution. Each sample of the pdf is composed of a system state estimate x , called a particle, and a corresponding weight w , that describes a particle's relevance.

Let X represent the collection of particles and W the collection of corresponding particle weights as:

$$X = [x_1 \ x_2 \ \dots \ x_P]^T \quad P \text{ is the number of particles} \quad (6.26)$$

$$W = [w_1 \ w_2 \ \dots \ w_P]^T \quad (6.27)$$

where

$$\sum_{i=1}^P w_i = 1$$

Now the state estimate and state pdf can be described in terms of X_{t_k} and W_{t_k} for the time instant t_k . Let z_{t_k} represent a state measurement from the sensory systems and let Z_{t_k} represent the measurement history up until the time instant t_k .

A particle filter, like the Kalman Filter, operates in two phases: a prediction phase and an update phase. In the prediction phase the state of each particle is propagated forward in time from the previous cycle to the moment just before a measurement update, via a system model. In the update phase the weight of each particle is re-evaluated based the most recent measurement z_{t_k} [56]. More formally, at some time instant t_k the particle filter will have the state-pdf from the previous

time cycle (t_{k-1}) and a measurement update z_{t_k} for t_k . The goal of the filter is to estimate the state-pdf for t_k , called the posteriorPDF, based on $X_{t_{k-1}}$, $W_{t_{k-1}}$ and z_{t_k} .

The Filter process starts by propagating the state estimate from $X_{t_{k-1}}$ to the current time instant t_k (prediction phase) via a system model $f(x, \epsilon)$. $f(x, \epsilon)$ is based on dynamic models of the system, like Equation 2.15, these models describe how the system state changes based on a set of controlled inputs. In addition, $f(x, \epsilon)$ is augmented by adding some noise to the state propagation that models the effect of the expected input noise ϵ on the control inputs and/or system. $\hat{X}_{t_k} = [\hat{x}_{1,t_k} \hat{x}_{2,t_k} \dots \hat{x}_{P,t_k}]^T$ is used to represent the set of filter predicted states.

The next step is to estimate how likely are the predicted particle states \hat{X}_{t_k} based on the latest measurement update z_{t_k} . This is accomplished by using a measurement model $h(x_{t_k})$ and a likelihood function $L(\cdot)$. $h(x_{t_k})$ expresses the relationship between a sensor measurement and system state. It is used to obtain a set of predicted measurements $\hat{Z}_{t_k} = [\hat{z}_{1,t_k} \hat{z}_{2,t_k} \dots \hat{z}_{P,t_k}]^T$ from \hat{X}_{t_k} . $L(\cdot)$ is used to estimate how well each predicted measurement \hat{z}_{i,t_k} correlates to z_{t_k} , based on an estimate of measurement variance σ_z^2 . Equation 6.28 is a generalized Gaussian likelihood function for a single measurement update [56]

$$L(\hat{x}_{t_k} | z_{t_k}, \sigma_z^2) = \frac{1}{2\pi\sigma_z^2} \exp\left(-\frac{(z(t_k) - \hat{z}(t_k))^2}{2\sigma_z^2}\right) \quad (6.28)$$

Note that the likelihood equation does not have to be Gaussian, it is chosen based on the error characteristics of the measurement model, here a Gaussian likelihood is used as an example.

Now that the likelihood of each independent propagated state has been determined, the posteriorPDF can be estimated. The process starts by re-evaluating the particle weights W_{t_k} based on $W_{t_{k-1}}$ and the likelihood of each propagated state. This is done by combining the information of both the likelihood estimates and $W_{t_{k-1}}$, via

Equation 6.29 [56].

$$\begin{aligned}
 W_{t_k} &= [w_1 \ w_2 \ \dots \ w_P]^T \\
 w_{i,t_k} &= \frac{L(\hat{x}_{i,t_k} | z_{t_k}, \sigma_z^2) w_{i,t_{k-1}}}{\sum_{i=1}^P L(\hat{x}_{i,t_k} | z_{t_k}, \sigma_z^2) w_{i,t_{k-1}}} \\
 \sum_{i=1}^P w_{i,t_k} &= 1
 \end{aligned} \tag{6.29}$$

Note that the denominator in Equation 6.29 serves as a normalizing factor, that forces the sum of W_{t_k} to equal one. Now the posteriorPDF is represented by the set of independently propagated states $X_{t_k} = [x_1 \ x_2 \ \dots \ x_P]^T$ and their corresponding updated weights W_{t_k} . Now the state estimate \bar{X}_{t_k} of the filter and weighted covariance P_{t_k} can be calculated via the Equations 6.30 and 6.31.

$$\bar{X}_{t_k} = E[X_{t_k}] = \sum_{i=1}^P w_i x_i \tag{6.30}$$

$$P_{t_k} = E[(x_i - \bar{X})(x_i - \bar{X})^T] = \sum_{i=1}^P w_i [x_i - \bar{X}][x_i - \bar{X}]^T \tag{6.31}$$

As a final note, it is possible in the particle filter for a few particles to account for most of the weight in W and the majority of the other particle to have near zero weights. This condition is known as particle starvation [55]. This problem, if left unattended, could drastically reduce the filter estimation performance. Particle re-sampling is a strategy used to tackle this problem. The basic approach is to eliminate particles with low weights and replace them with particles with the highest weights, without changing the underlying pdf. First, a method for estimating the amount of particles that contain most of the weight is necessary. Liu *et al.*, proposed methods of estimating the number of particles that carry most of the weight via the coefficient of variance cv_{t_k} , Equation 6.32, and the effective sample size (ESS), as illustrated in Equation 6.33 [57].

$$cv_{t_k} = \frac{var(W_{t_k})}{E^2(W_{t_k})} \tag{6.32}$$

$$ESS_{t_k} = \frac{P}{1 + cv_{t_k}} \quad (6.33)$$

When ESS drops below a certain fraction of the P , then the re-sampling strategy is applied. The fraction of P is initially estimated by the user based on the application and later tuned based on experimentation

The simplest method of particle re-sampling is by creating a new set of particles and selecting with replacement from X , where the probability of selecting a particle is equal to its corresponding weight. The strategy is based on the premise that particles with the highest weights, and that contribute most to the statePDF, are selected multiple times and the particles with near zero weights are rarely selected. As a last step to the re-sampling strategy, all of the particle weights are reset to $1/P$.

Horizontal Particle Filter Mechanization

System Models. As mentioned in Section 6.6.2, the particle filter uses system models to estimate the system state at a future time. The system model must add independent noise to each estimate. The added noise is selected to approximate the noise characteristics in the underlying system. Two systems models were developed for the (HPPF), one is based on INS performance, and the second one is a First Order Gauss-Markov Acceleration Model (FOGMA).

The INS model is based on the navigation equations presented in Section 2.1.5 and a modified model of INS estimation errors presented by Titterton in [1]. When using the INS system model, the state x of each particle consists of five $[3 \times 1]$ vectors, for a total 15 elements:

$$x = \begin{bmatrix} \delta p \\ \delta v \\ \delta \Psi \\ b_a \\ b_g \end{bmatrix}, \quad (6.34)$$

where δp is the INS position error vector, δv is the INS velocity error vector, $\delta \Psi$ is the INS attitude error vector, and b_a and b_g are the bias state vectors, for the accelerometer and gyroscope bias stability model. The INS error model for a six degree of freedom INS is given by:

$$\dot{x}(t) = Fx(t) + w(t) \quad (6.35)$$

where

$$F = \begin{bmatrix} 0 & I_3 & 0 & 0 & 0 \\ 0 & 0 & (f^n \times) & C_b^n & 0 \\ 0 & 0 & 0 & 0 & -C_b^n \\ 0 & 0 & 0 & -\frac{1}{\tau_a} & 0 \\ 0 & 0 & 0 & 0 & -\frac{1}{\tau_g} \end{bmatrix}, \quad (6.36)$$

$$w(t) = \begin{bmatrix} 0 & C_b^n \omega_a & -C_b^n \omega_g & \omega_{a_{bias}} & \omega_{g_{bias}} \end{bmatrix}^T, \quad (6.37)$$

where

- I_3 is a 3×3 identity matrix.
- $(\cdot) \times$ is the cross product operator that creates a skew symmetric matrix of its input vector, f^n in case of Equations 6.36.
- C_b^n is a DCM that transforms a vector from the b-frame to the n-frame.
- τ_a and τ_g are the time constants of the FOGMP modeling the bias stability of the accelerometer and gyroscopes respectively.
- f^n is the specific force measurement from the accelerometer.
- ω_a and ω_g are white Gaussian noise modeling thermo-mechanical noise in the accelerometer and gyroscope sensors respectively.
- $\omega_{a_{bias}}$ and $\omega_{g_{bias}}$ are the white Gaussian noise that drive the FOGMP.

Parameters τ_a , τ_g , ω_a , ω_g , $\omega_{a_{bias}}$, and $\omega_{g_{bias}}$ are selected based on the performance characteristics of the inertial sensors. All noise sources are assumed independent.

The filter particles are first initialized with the expected error from the system initial conditions. Then particles are propagated forward in time via Equation 6.35, as the INS produces its estimates until a measurement update becomes available. At this time, the error estimates of each particle are added to the INS estimates of vehicle state to obtain a particle spread around the INS estimate that is a function of the inertial sensor performance characteristics.

With the FOGMA system model accelerometer measurements are replaced by accelerations modeled by FOGMPs. The basis of this substitution is when an FV is deployed it spends most of the deployment in a static (non-accelerating) state. With exceptions being short lived events (less than 5s), when leaving the surface, reaching the final depth, releasing ballast, and reaching surface. When operating in a static state, accelerometer and gyroscope measurements will be mainly noise from the sensors. That, depending on sensor performance, can cause tens of meters of position error in 10 min to thousands of meters in position error, in the same 10 min. When these error performances are compared to the expected horizontal displacement of the FV [46], expected position errors would overshadow the FV horizontal position displacements. For this reason when using the FOGMA the accelerometer readings are replaced by FOGMA output that more closely resembles expected FV horizontal displacement. FOMGA have been used to model car and robot displacement for the purpose of navigation [56].

When using FOGMA, system model the state of each particle becomes:

$$x = \begin{bmatrix} p & v & a \end{bmatrix}^T \quad (6.38)$$

where p is $[2 \times 1]$ horizontal position vector with the form $[Lat \ Lon]^T$, v is a $[2 \times 1]$ horizontal velocity vector of form $[V_{north} \ V_{east}]^T$, and a is a $[2 \times 1]$ horizontal acceleration vector with the form $[a_{north} \ a_{east}]^T$.

The FOGMA then takes the form:

$$\dot{x}(t) = F_{FOGMPA}x(t) + w_{FOGMPA}(t), \quad (6.39)$$

where

$$F_{FOGMPA} = \begin{bmatrix} 0 & 0 & 1 & 0 & 0 & 0 \\ 0 & 0 & 0 & 1 & 0 & 0 \\ 0 & 0 & 0 & 0 & 1 & 0 \\ 0 & 0 & 0 & 0 & 0 & 1 \\ 0 & 0 & 0 & 0 & -\frac{1}{\tau_{north}} & 0 \\ 0 & 0 & 0 & 0 & 0 & -\frac{1}{\tau_{east}} \end{bmatrix}, \quad (6.40)$$

$$w_{FOGMPA}(t) = \begin{bmatrix} 0 & 0 & 0 & 0 & \omega_{north} & \omega_{east} \end{bmatrix}^T, \quad (6.41)$$

τ_{north} and τ_{east} are the time constants for the FOGMA in the north and east directions respectively, and ω_{north} and ω_{east} are the white Gaussian noise that drives the FOGMA process.

Measurement Model. The following paragraphs specify the measurement model used for the HPPF and assumptions made in its development. For our application, the measurement model $h_{HPPF}(x)$ relates the vehicle position to an expected magnetic measurement. In Section 2.3 we presented the components of the magnetic field, the magnetic fields that might be present when a magnetometer is sampled, and the steps necessary to extract a magnetic anomaly measurement from a magnetometer sample. Now we present the assumptions made in the development of the measurement model for the HPPF.

First, the height dependence of the anomaly magnetic field. Normally, magnetic anomaly maps over oceans are sampled from the water surface, meaning that the anomaly fields in those maps are not suitable for underwater magnetic navigation, since the contours of the anomaly field would change with depth [58]. From here,

there are two options: constructing a magnetic anomaly map at the operating depth or extrapolating the magnetic data from the surface to greater depths, via downward continuation techniques (DCT) [59]. Continuation techniques are used to predict magnetic intensities at different heights. Upward continuation has demonstrated promising results, but DCT is still a topic of research [58]. In an effort to continue forward with the navigation solution, the magnetic anomaly map of the oceans surface will be used regardless of the FV depth and assumed accurate enough for the purposes of navigation.

The magnetometer will be assumed to be calibrated, meaning that the only remaining source of error would be the sensor measurement noise. Other sources of error include mapping error, diurnal variations, remaining error from the WMM, and errors induced by magnetic storms. These sources of error will be modeled as Gaussian noise. This assumption, although not ideal, not uncommon for magnetic storm and sensor measurement noise, but somewhat inadequate for residual WMM errors [32].

With the given assumptions, the horizontal position measurement model can be expressed as:

$$\hat{z}(t_k) = \text{map}(x_k(1), x_k(2)) + \omega_{\text{residual}}, \quad (6.42)$$

where h_{horz} is the estimated magnetic anomaly measurement at location $[x(1), x(2)]$ described by the system state x ; $\text{map}(\cdot)$ is a function that samples the magnetic anomaly map at the location specified; and ω_{residual} represents the residual sampling noise modeled as Gaussian noise.

Likelihood Equations. Given the measurement magnetic measurement model assumptions, regarding residual measurement errors, a Gaussian Likelihood equation was adopted as the filter likelihood equation.

$$L(\hat{x}_{t_k} | z_{t_k}, \sigma_{\text{residual}}^2) = \frac{1}{2\pi\sigma_{\text{residual}}^2} \exp\left(-\frac{(z(t_k) - \hat{z}(t_k))^2}{2\sigma_{\text{residual}}^2}\right) \quad (6.43)$$

where $\sigma_{residual}^2$ is the variance of $\omega_{residual}$ and $z(t_k)$ is the latest magnetic anomaly field measurement.

Magnetic Anomaly Map. The earth's magnetic anomaly Map (EMAG2) is a 2-arc minute resolution map of the Earth magnetic anomaly field [60]. The map was constructed based on magnetic samples from magnetic survey trips (on land and sea and air) and magnetic data provided by satellite. The map is provided at two altitudes; sea level for sea covered areas, and at 4 km altitude for land and sea covered areas. The resolution of the map is too coarse for our application and thus it is interpolated at the desired location using 2D spline methods.

Matlab HPPF Implementation. The HPPF was implemented in four Matlab scripts. The user chooses which to use depending on whether the script is going to process real or simulated data and which system model and measurement model is going to be used. The scripts can be divided into six main sections: parameter specification, load sensor data, sensor data processing, filter initialization, filters loop, and a results section. The roles and actions performed in each section are specified bellow:

Parameter Specification In the parameter specification phase the user provides the duration of the deployment (in seconds), the system model sampling period, the measurement update period, control parameters for the system model, system initial state estimate, initial state error (sa standard deviations for each state) and the control parameters for the HPPF.

The parameters for the system model, naturally, depend on the chosen system model for the particle filter. If the INS system model is used then the user must specify the performance parameters τ_a , τ_g , ω_{abias} , ω_{gbias} , ω_a , and ω_g for the accelerometer and gyroscope (see Equations 6.35-6.37). If the FOGMA were used instead, the user must specify the control parameters τ_{north} , τ_{east} , ω_{north} and ω_{east} of the FOGMA model, in Equations 6.39-6.41.

The specified initial state estimate and expected error estimate, also depend on the system model chosen. If the INS model were used the user must provide initial conditions for r^n , v_e^n , and $q_{b,0}^n$ of Equations 2.13, 2.14 and 2.9. With the initial conditions, the user must also specify corresponding expected error (as a standard deviation) for each state. These initial estimate errors would later be used to initialize the particle's of the filter. If the FOGMA model were used instead, then the user would specify initial conditions for p , v , and a of state Equation 6.38, and corresponding expected errors, as a standard deviation for each state.

The control parameters for the HPPF are: the number of particles P and the threshold value re-sampling the filter's particles. The threshold value must be between 0 and 1 and represents the minimum fraction of P before particle re-sampling is performed.

Load Sensor Data When processing real data gathered from a FV deployment, if the magnetic measurement model is used then magnetometer samples are loaded from a sensor file, obtained from the FV. If the IMU system model were used then, IMU sample data would also be loaded from the sensor file. Else if, the FOGMP model were used, no additional data would be loaded.

When processing simulated data: first, an FV trajectory is simulated using the trajectory simulator in Section 6.2. At this point, if the INS system model is used, then the FV accelerations in the n-frame, from the trajectory generator, are corrupted by noise using the sensor models presented in Section 6.3. Else if, the FOGMA system model is used, no further simulations of data are necessary.

Sensor Data Processing When processing real deployment data and using the magnetic measurement model, magnetic anomaly measurements are extracted from the magnetometer samples via the process mentioned in Section 2.3. Then if, the INS system model were used: the vehicle's attitude would be estimated using the complementary filter, in Section 6.6.1, to create a quaternion description of the vehicle

attitude in time. Then the attitude estimates are used to project the specific force measurements, from the accelerometer, in the b-frame to the n-frame. These n-frame acceleration are then the ones used for the INS. If the FOGMP were used then no IMU sensor information needs to be loaded into the system.

When simulated data is used instead, the horizontal position from the simulated trajectory are used to simulate magnetic anomaly measurements via the measurement model in Equation 6.42, if the magnetic measurement model is selected. Then if, the INS system model were used: the n-frame vehicles accelerations, provided by the trajectory generator are used for the INS system model. Else if, the FOGMA model were used instead: no further data simulation would be needed.

Particle Initialization At this point of the script the filter's particles are initialized based on the initial conditions provided earlier and their expected error.

Filter's Loop In the Filter loop phase the deployment duration is divided into $c = \text{floor}(\text{deployment_duration}/\text{measurement_period})$ time window. At the start of each time windows, the effective sample size of the particles is estimated, via Equations 6.32 and 6.33. If the effective sample size falls below the user specified threshold, particle re-sampling is then performed. Then the HPPF would go through its prediction stage, in which it would use the system model to predict the FV horizontal position at the moment just before a measurement update. If the magnetic measurement model was used the predicted vehicle positions are used to produce a set of predicted magnetic anomaly samples using the measurement model in Equation 6.42. The predicted magnetic anomaly samples are then compared to the anomaly sample extracted from the magnetometer using the Likelihood Equation 6.43. At this point the particles weights $W_{t_{k-1}}$ are re-evaluated using Equation 6.29. As a final step, estimates of the vehicle state and confidence intervals are obtained, via Equations 6.30 and 6.31, and saved.

Results In the final section of the script the results of the particle filter's state estimate are plotted for analysis.

Depth Particle Filter Mechanization

This Section presents the mechanization of the depth particle filter. Starting with the filter's system models in the following paragraph. The discussion continues by presenting likelihood and measurement equations and concludes by presenting the filter's implementation.

Depth Particle Filter System Models. Two system models were developed for the depth particle filter, one based on INS performance and a second based on the FOGMA model. The system model based on INS performance is exactly the same model presented in Section 6.6.2, only that this time only the components related to the vertical axis are the only outputs used. Using the INS model the state of the filter is then represented by Equation 6.34. Now the same process described in Section 6.34 takes place: the particles are initialized with the expected amount of initial condition error. The INS uses IMU data to produce an estimate of the vehicle location and the error state of the particles are propagated via Equation 6.35 until a measurement update becomes available. At this time INS estimates are added to each particle error state to produce an estimated end depth per particle that considers potential INS error.

The second system model used for the depth particle filter is based on a FOGMA model that describes the expected FV descent and ascent dynamics. When using the FOGMA model the state of the depth particles become:

$$x_{dpth} = \begin{bmatrix} d & V_d & a_d \end{bmatrix}^T \quad (6.44)$$

where d is the estimated depth for the particle, V_d is the estimated downward velocity and a_d is the acceleration state of the particle's FOGMA model. The FOGMA system

model is given as:

$$\dot{x}_{dpth}(t) = F_{dpth}x_{dpth}(t) + w_{dpth}(t), \quad (6.45)$$

where:

$$F_{dpth} = \begin{bmatrix} 0 & 1 & 0 \\ 0 & 0 & 1 \\ 0 & 0 & -\frac{1}{\tau_{dpth}} \end{bmatrix}, \quad (6.46)$$

$$w_{dpth} = \begin{bmatrix} 0 & 0 & \omega_{dpth} \end{bmatrix} \quad (6.47)$$

where τ_{dpth} is the time constant selected for the FOGMA and ω_{dpth} is the white Gaussian noise driving the FOGMA. Both $\tau_{dpth} = 100s$ and $\omega_{dpth} = 0.05$ are selected to model the FV expected vertical dynamics including: constant descent and ascent velocities around $1m/s^2$ and rapid acceleration and deceleration.

Measurement Update And Likelihood Equation. This section specifies how the measurement update is done in the depth particle filter. Since Equation 2.18 relates a pressure measurement to sea water depth, with a one-to-one relationship, the measurement update will be applied directly in depth. Meaning that the estimated depth of each particle is compared to the depth estimate provided by the depth sensor measurement. According to the pressure measurement model presented in Section 2.2, the errors in depth estimates from a calibrated pressure measurement we are considering are the pressure sensor's thermo-mechanical noise and the geopotential anomaly from Equation 2.18. If the remaining errors are modeled Gaussian noise, this enables us to use a Gaussian likelihood equation for the depth particle filter. The depth filter's likelihood equation can then be expressed as:

$$L_{dpth}(x_{i,dpth}(1)|x_{sens}) = \frac{1}{2\pi\sigma_{dpth}} \exp\left(-\frac{(x_{i,dpth}(1) - x_{sense})^2}{2\sigma_{dpth}}\right) \quad (6.48)$$

where $x_{i,dpth}(1)$ is the depth estimate from the i^{th} particle, x_{sense} is the depth update from the pressure sensor, and σ_{dpth} is the standard deviation of the error in the measurement model.

DPF Matlab Implementation. The depth particle filter was implemented as four Matlab scripts, similar to the implementation of the position filter. Which script to run depends on whether the user want to analyze real or simulated data and whether the INS or FOGMA model is used. The script's actions can be divided into five sections: parameter specification, sensor data load phase, filter initialization, filter loop and a results sections. The roles of each section are the same as for the position filter, see Section 6.6.2

6.7 Experimental Setup

This section presents the experimental setup used to test the different subcomponents of the navigation system. The experiments use both simulated and real data sensor data. First Section 6.7.1 presents the experimental setup for the test performed on the attitude complimentary filter. Section 6.7.2 presents the experimental setup for the experiments performed on the position particle filter. The experimental setup for the experiments performed on the depth particle filter are presented in Section 6.7.3.

6.7.1 Attitude Complementary Filter Test Setup

Simulated Attitude Complementary Filter Test. A series of simulated tests were performed on the complementary attitude filter with the objectives of verifying its functionality and evaluating its performance when using different sensor performance grades. The basis of each test was the same, consisting of simulating three consecutive constant velocity rotations of $1m/s$ on the b-frame's x, y, and z axes, With a sensor sampling frequency of 10Hz. First, the best case attitude estimate was computed using the ideal constant velocity rotation stimuli and the

attitude computer. This attitude estimate was treated as the true attitude of the systems and later used as a metric to estimate the complementary filter's performance. Gyroscope measurements were simulated by corrupting the constant velocity rotation with the error from the sensor model presented in Section 6.3. Accelerometer and Magnetometer data were simulated by rotating the global frame vectors (gravity and magnetic field) into the local frame using the attitude reference produced by the processing of the constant velocity rotations. The accelerometer and magnetometer simulated measurement were later corrupted with the sensor models to represent more realistic sensor readings.

Now that the basis of each simulated test was presented, we can present the different test cases considered:

- *Test Case 1:* The gyroscope measurements were corrupted by error in the sensor models to quantify the effect of gyroscopic error in the filter attitude estimate. The measurements of the accelerometer and magnetometer will be kept ideal. We expected the filter to be able to produce a drift free, attitude estimate due to the accelerometer and magnetometer measurements.
- *Test Case 2:* The accelerometer measurements were corrupted by the sensor models to quantify the effect of accelerometer measurement error in the filter's performance. The gyroscope and magnetometer readings were kept ideal and the performance parameters of a consumer grade accelerometer was used in the sensor model. We expected the filters pitch and roll attitude estimates to be noisy, due to the noise in the accelerometer measurement but free of any attitude drift.
- *Test Case 3:* The magnetometer measurements were corrupted by the errors in the sensor model to quantify the effect of magnetometer error in the filters performance. The gyroscope and accelerometer readings were kept ideal and the performance parameters of a consumer grade magnetometer were used in the sensor model. We expected the filters yaw attitude estimates to be noisy due to the error in the

magnetometer's measurements but the pitch and roll components would remain unaffected.

- *Test Case 4*: All of the sensor measurements were corrupted by the sensor models with performance parameters pertaining to consumer grade sensors. We expected the filter to be able to produce a drift free attitude estimate, with some noise.
- *Test Case 5*: All of the sensor measurements were corrupted by the sensor models with performance parameters pertaining to tactical grade sensors. We expected the filter to be able to produce a drift free attitude estimate, with some noise less than the one exhibited in *Test Case 4*.

The performance parameters used for the sensor models pertaining to consumer, tactical and navigation grade are tabulated in Table 6.1 :

Performance Parameter	Consumer Grade	Tactical Grade	Navigation Grade
c_a (m/s^2)	0	0	0
ω_a (m/s^2)	$1.96e^{-1}$	$9.8e^{-3}$	$2.45e^{-4}$
τ_a (s)	3600	3600	3600
ω_{abias} ($m/s^{3/2}$)	$4.3e^{-3}$	$9.5e^{-3}$	$2.3e^{-4}$
c_g (rad/s)	0	0	0
ω_g (rad/s)	$8.7e^{-3}$	$4.8e^{-6}$	$7.2e^9$
τ_g (s)	3600	3600	3600
ω_{gbias} ($rad/s^{1/2}$)	$6.5e^{-4}$	$8.7e^{-5}$	$5.8e^{-7}$
c_m (nT)	0	0	0
ω_m (nT)	$300nT$	$50nT$	$10nT$
τ_m (s)	∞	∞	∞
ω_{mbias} ($nT^{1/2}$)	0	0	0

Table 6.1 : Sensor Performance Parameters

The IMU sensor performance parameter used were presented by Kauffman *et al.* in [61]. The performance parameters for the magnetometer were derived from the datasheet of the MPU 9150 sensor, [56], and [59] for the consumer, tactical and navigation grade magnetometer sensor perforce parameters.

6.7.2 Horizontal Position Particle Filter Test Setup

A series of simulated tests were performed on the position particle filter with the objective of verifying its functionality and to gain insight into expected navigation performance based on the system model, measurement model and sensor grades used. For the magnetic measurement model three main simulation tests cases were performed, one in which the magnetic navigation error was 1nT (standard deviation), another where the error was 10nT and the last one, where the error was 50nT. Both, the INS and FOGMP system models will be used in each of the three main test cases. The INS system model was tested using the three accelerometer and gyroscope sensor grades, presented in Table 6.1 . Each test will attempt to estimate the landing position of a simulated FV deployment. A system sampling period of 1/10s and measurement update period of 45s at 68.5 deg Latitude, 19.5 deg Longitude and an a depth of 1m was used as the system's intimal conditions. Initial velocity and accelerations were assumed to be zero. With a position accuracy of 5m in the North and East, a 0.3m depth accuracy, a $0.1m/s$ velocity accuracy and $0.001m/s^2$ acceleration accuracy. In an attempt to process real deployment data with the HPPF using the magnetic measurement model two deployment data sets form March 8, 2016 were analyzed.

For the PFHD measurement model three simulated deployments were made, using the performance parameters of a commercial, tactical and navigation grade INS, from Table 6.1 . A system sampling period of 1/10s and measurement update period of 1s was used The simulated deployment location was at 68.5 deg Latitude, 19.5 deg Longitude and the initial depth of the system was set to 1m. The simulated FV deployment was set to 4000m of depth. In addition a total of five real deployment data set were analysed using the PFHD measurement model. The results of these tests are presented and analyzed in Chapter 7.

6.7.3 Depth Particle Filter Tests Setup

The depth particle filter (DPF) was tested using both real and simulated data sets. The objective of the simulated data tests was to gain insight on the depth estimate performance of the DPF. All simulated tests were performed assuming the pressure measurement came from a calibrated pressure sensor rated to 10,000 decibars and a measurement accuracy of 0.1% of the pressure range [8]. The different simulated test cases test the DPF performance with navigation, tactical, and consumer-grade IMUs and the FOGMPA model. The simulated test cases are presented below:

- *Test Case 1*: This represented the best case scenario using the INS model and the performance parameter a navigation grade IMU.
- *Test Case 2*: The INS model used the performance parameters of a tactical-grade INS.
- *Test Case 3*: The INS used the performance parameters of a consumer-grade INS.
- *Test Case 4*: The FOGMPA model was used with the performance control parameters set to τ_{dpth} and ω_{dpth} , which were found to describe the expected vehicle vertical dynamics (including acceleration and deceleration). This test case evaluated the DPF estimation performance based on a model FV vertical dynamics alone, with no INS data.

All simulated test were performed on a 1 hour FV simulated trajectory. The depth measurement updates were simulated by adding independent white Gaussian noise, with a standard deviation of 10m, to the simulated FV depth trajectory. IMU measurements were simulated by corrupting the n-frame FV accelerations provided by the trajectory generator via the presented IMU sensor models and the IMU performance parameters specified in each case. With an IMU sampling period of 1/10s and measurement update period of 1s, 1000 particle, an initial depth of 3m with an expected error of 0.3m, initial vertical velocity of 0 with 0.05 expected error and an acceleration of $0m/s^2$ with an error of $0.005m/s^2$

Chapter 7

Results and Analysis

In this chapter, we present and analyze the results of the different tests performed on the estimators of the post-processing navigation system. The tests results and analysis for the attitude complementary filter are presented in Section 7.1. The results of the tests performed on the horizontal position particle filter (HPPF) are presented and analyzed in Section 7.2. Section 7.3 presents the results and analysis of the tests conducted on the depth particle filter (DPF). The final Section of the chapter concludes with a brief summary of the test results for each filter and recaps on highlights of the result's analysis.

7.1 Attitude Complementary Filter Test

7.1.1 Attitude Complementary Filter Tests With Simulated Data Sets

Test Case 1

This simulated experiment was meant to estimate the attitude complementary filter's performance with simulated gyroscope data and error free accelerometer and magnetometer data. The plots on the left column in Figure 7.1 show the ideal body rates, of 1 revolution per minute in the b-frame's x , y and z axes. The middle column, depicts plots of the simulated gyroscope errors using the sensor models from Section 6.3, and the performance parameters of a commercial gyroscope (see Table 6.1). The plots on the right column illustrate the simulated gyroscope output created by adding the simulated sensor noise to the ideal body rates.

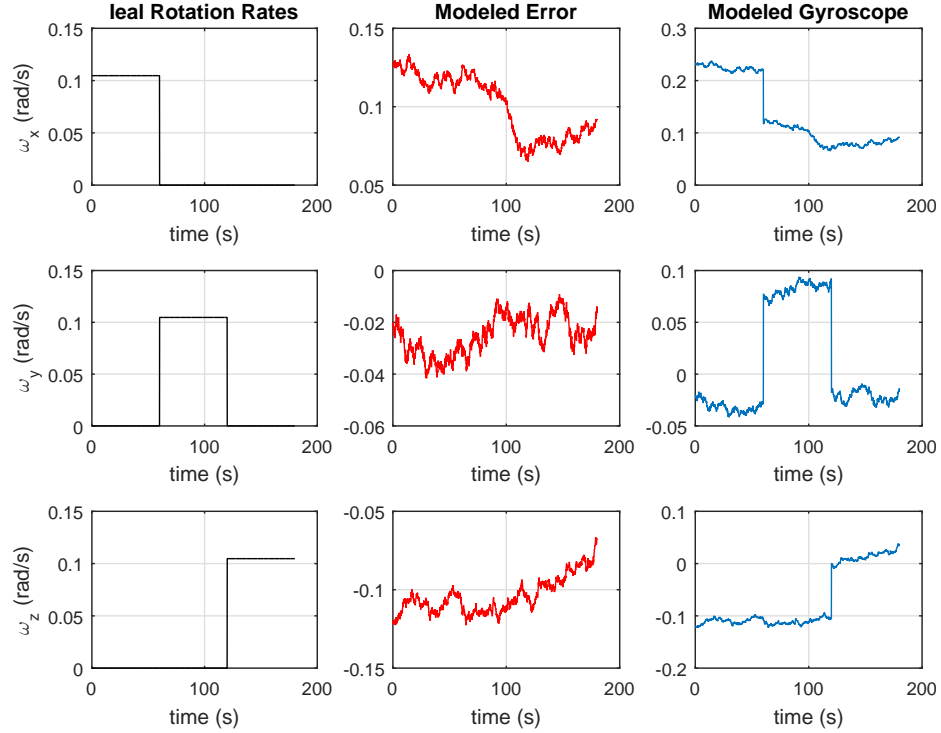


Figure 7.1 : Plot of the gyroscope simulated measurements.

The results from the simulation are shown in Figures 7.2 and 7.3 . The first plot in Figure 7.2 is the attitude estimated from the simulated input rates q_{in} , the second plot provides the filter's attitude estimate q_{fltr} , and the third plot corresponds to the attitude estimates derived from solely using gyroscopic data q_w . Note that within a few seconds of the simulation q_w drifts significantly from q_{in} . Also, the estimate of the complementary filter attitude q_{fltr} , closely follows the that of q_{in} , because of the corrections provided by the ideal accelerometer and magnetometer measurements.

The angle between two quaternions can be used to estimate the difference, or error, between their attitude representations. The angle θ_q between two quaternions q_1 and q_2 can be obtained using the following Equations 7.1 and 7.2.

$$q_{1,2} = q_1 \otimes q_2 \quad (7.1)$$

$$\theta_{1,2} = \arccos(q_{1,2}(1)) \quad (7.2)$$

where $q_{1,2}(1)$ is the first element of $q_{1,2}$

The estimated drift, or error, between q_{in} and q_w is graphed in the second plot of Figure 7.3. From this plot we can observe that gyroscopic estimates of system attitude, drift in a matter of seconds. This is an expected outcome since the angle drift of commercial grade gyroscopes is measured in degrees per second. The first plot in Figure 7.3, shows the attitude errors between q_{in} and q_{fltr} . The filter attitude estimate was found accurate within 0.2° . This is largely due to the ideal references to the local vertical and local magnetic north provided by the ideal simulated accelerometer and magnetometer.

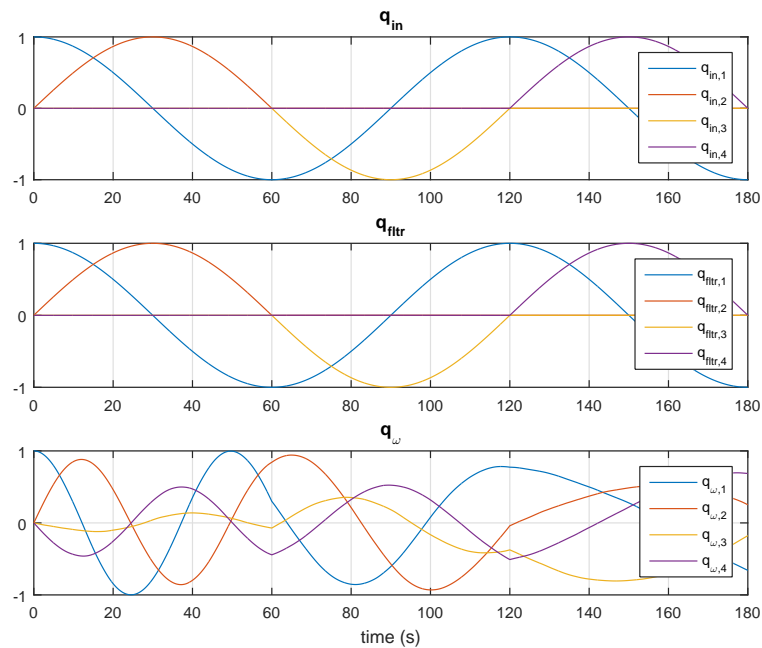


Figure 7.2 : Attitude plots: simulated input q_{in} , estimated from the complementary filter q_{fltr} and derived from gyroscopic data q_w , for test case 1

Test Case 2

This experiment was meant to estimate the attitude complementary filter's performance with simulated accelerometer data with ideal gyroscope rates and magnetometer measurements. The plots on the leftmost column in Figure 7.4 are the

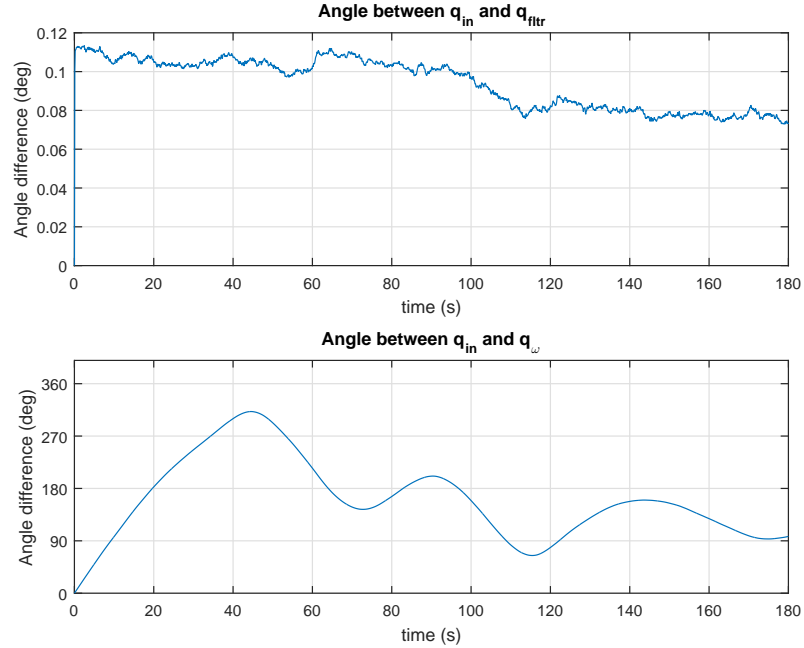


Figure 7.3 : Plot the attitude error of the complementary filter’s estimate.

normalized ideal accelerometer measurements of the local gravity vector as the sensor is rotated sequentially in the x , y , and z , axes at 1 revolution per minute. The middle column plots are of the simulated sensor errors in the accelerometer’s measurements. These error were simulated using the sensor models from Section 6.3, and the parameters for a commercial-grade accelerometer listed in Table 6.1 . Note that the data in the sensor error plots are not normalized to better recognize the magnitude of the corrupting sensor errors. The plots in the rightmost column of Figure 7.4 show the normalized simulated accelerometer outputs. The simulated accelerometer output seems very similar to the normalized ideal accelerometer, this is because the local gravity vector will have an average magnitude of $9.8m/s^2$ while the simulated bias stability errors have a magnitude less than $0.5m/s^2$ when both are added and normalized the bias errors are overshadowed. But the effect of the bias error is observable in the resulting filter estimates q_{ftr} , see the discussion bellow.

Test results are shown in Figures 7.5 and 7.6 . The plot in Figure 7.5 shows q_{in} , the simulated system’s input attitude and the second plot is the filter’s

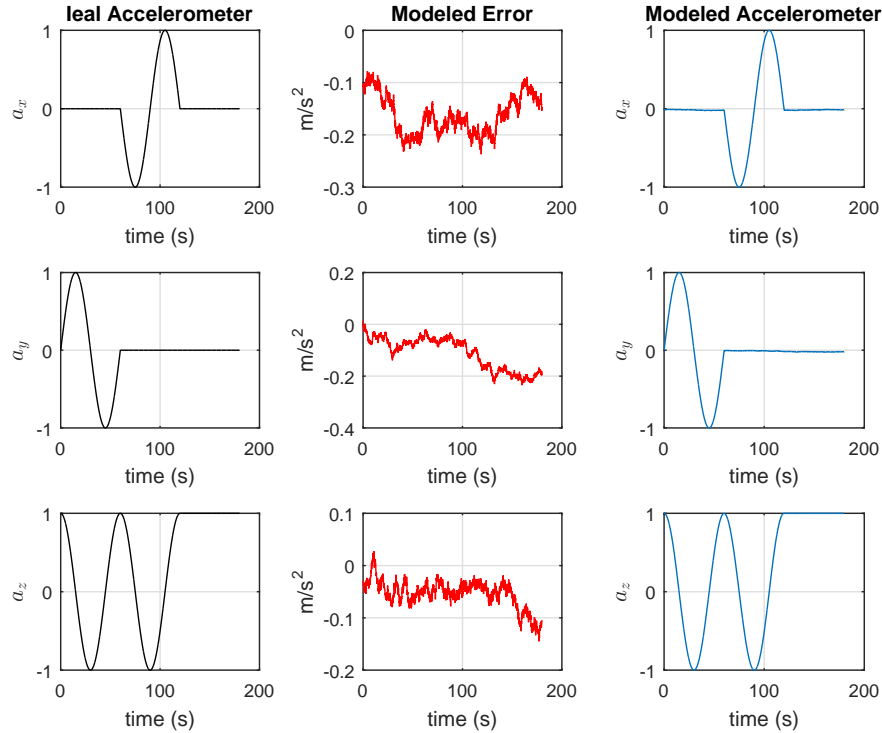


Figure 7.4 : Plot of the accelerometer simulated measurements.

attitude estimate q_{fltr} . The attitude error between q_{in} and q_{fltr} is estimated and plotted in Figure 7.6. Note that as the accelerometer data was not integrated in the system's attitude estimation process, remaining, sensor biases did not cause increasing attitude errors. Instead the attitude error oscillates with the bias errors from the accelerometer. The filter's performance error performance exhibit a mean value of 2° and oscillates as the local gravity vector is sensed by different sensor axes.

Test Case 3

This simulated experiment was meant to estimate the attitude complementary filter performance with simulated magnetometer data, with ideal gyroscope and accelerometer measurements. Similar to Test Case 2, Figure 7.7 contains the plots of the simulated magnetometer measurements used for the test. The left column plots, show the normalized ideal magnetometer measurements. The middle column plots,

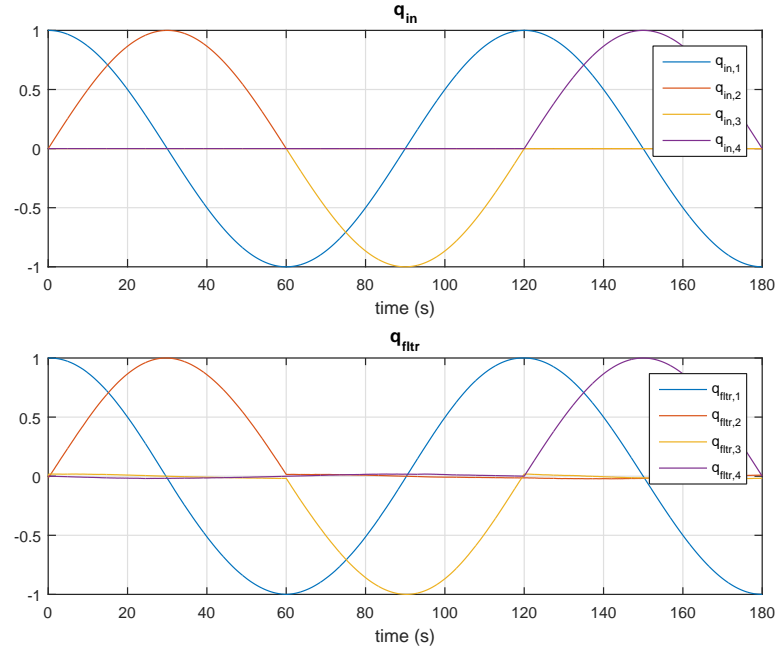


Figure 7.5 : Attitude plots: of simulated input q_{in} and estimated from the complementary filter q_{filtr} for test case 2.

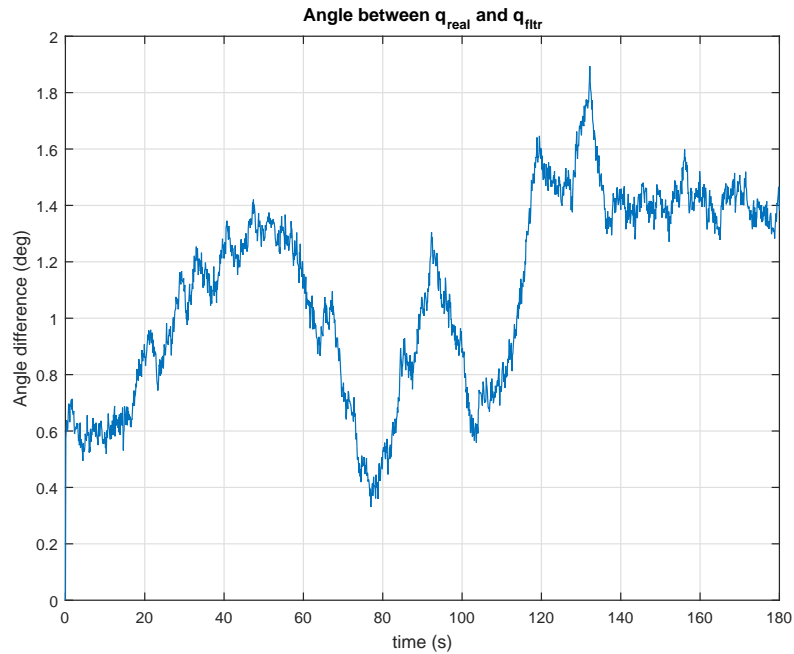


Figure 7.6 : Plot of the attitude error from attitude filter's test Case 2.

correspond to the un-normalized simulated magnetometer errors, and the plots on the right column, are of the normalized simulated magnetometer measurements.

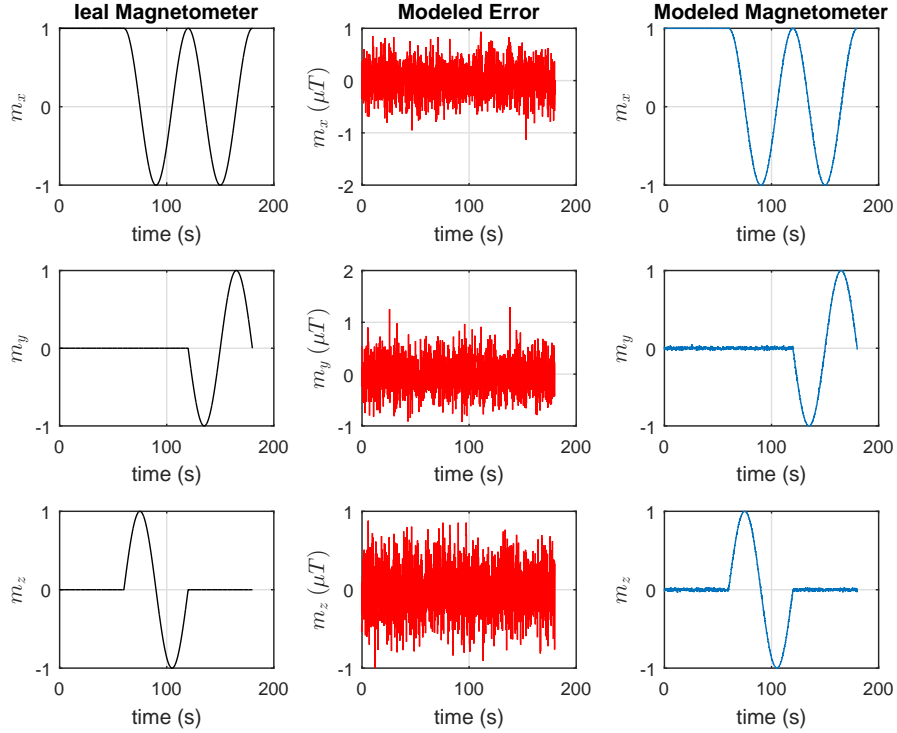


Figure 7.7 : Plot of the magnetometer simulated output

The results of the test are shown in Figures 7.8 and 7.9 . A plot of q_{in} , for this test, is located on the top of Figure 7.8 and a plot of q_{fltr} at the bottom. The attitude error between q_{in} and q_{fltr} is plotted in Figure 7.9 . Note, that similar to Test Case 2, since the magnetometer measurements are not integrated, the sensor's measurement errors result in a noisy attitude estimate. It is important to mention that in the presence of un-calibrated hard-iron or soft-iron effects, the attitude errors exhibit a constant offset or change in magnitude as a function of the system's orientation. The nature of the resulting attitude errors depends on the nature of the corrupting magnetic field affecting the magnetometer's measurements.

Test Case 4

In this test, the performance of the attitude filter's is evaluated using simulated sensor data from a commercial grade gyroscope, accelerometer, and magnetometer. The plots of the sensor data used for the test are in Figure 7.10 .

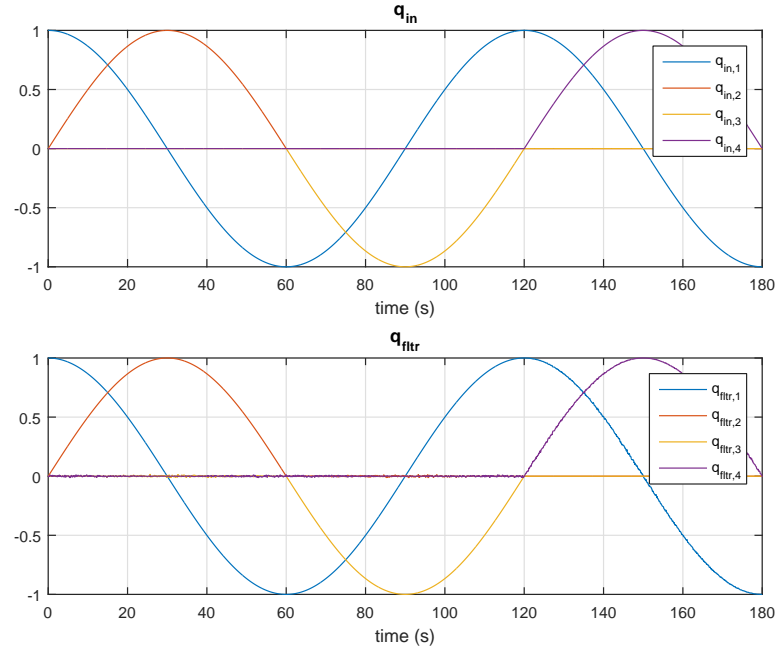


Figure 7.8 : Plots of the simulations true attitude q_{in} and attitude estimated from the complementary filter q_{filtr} for the Attitude Filter's Test Case 3.

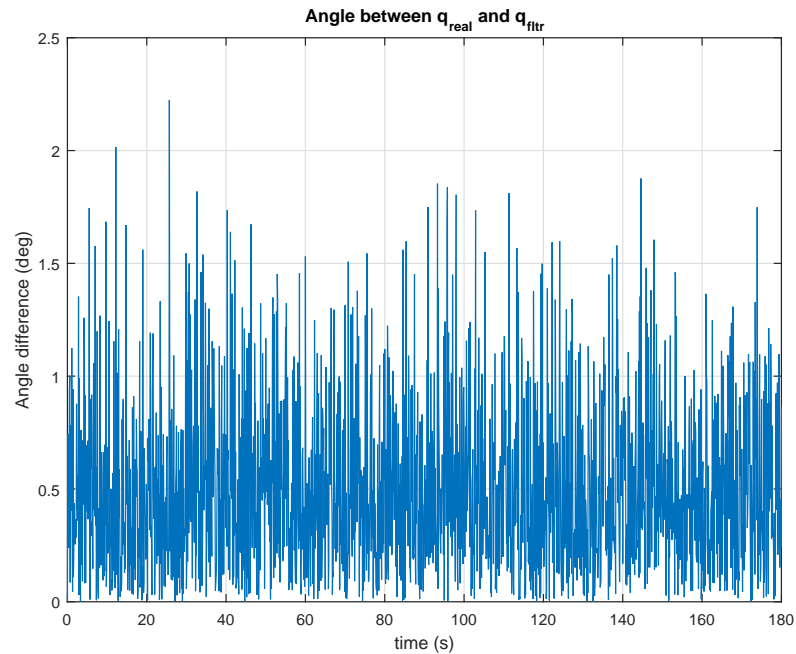


Figure 7.9 : Plot of the attitude error from attitude filter's test Case 3.

The input attitude of the simulated system, q_{in} , is plotted atop Figure 7.11, q_{filtr} , and q_w is in the middle and bottom plots respectively. Figure 7.12 is a plot of the attitude error between q_{in} and q_{filtr} .

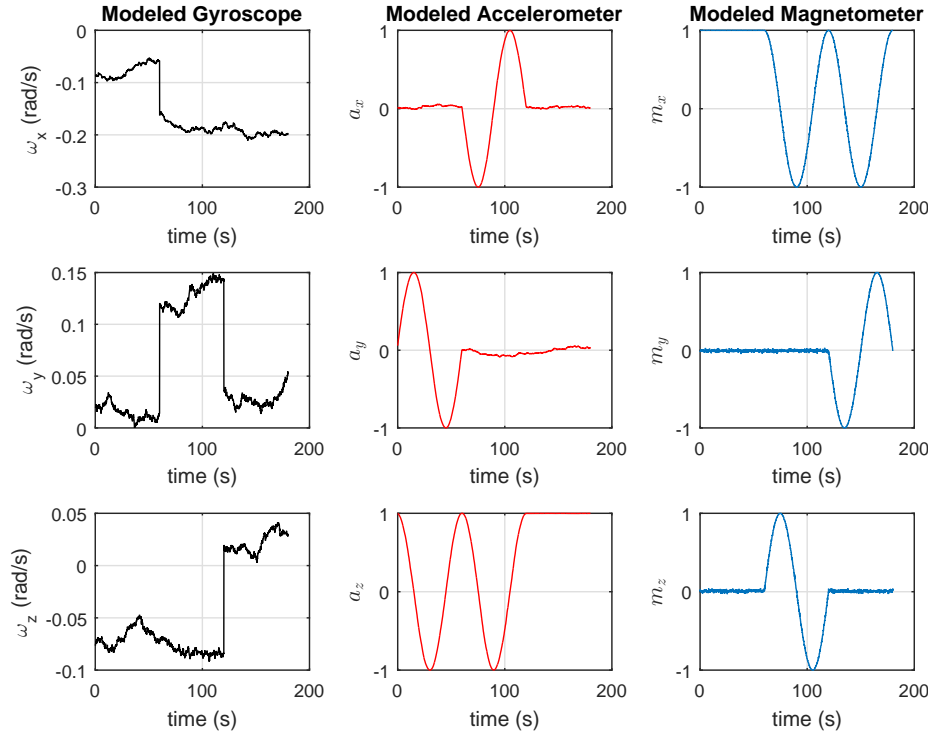


Figure 7.10 : Plot of simulated commercial grade gyroscope, accelerometer, and magnetometer measurements

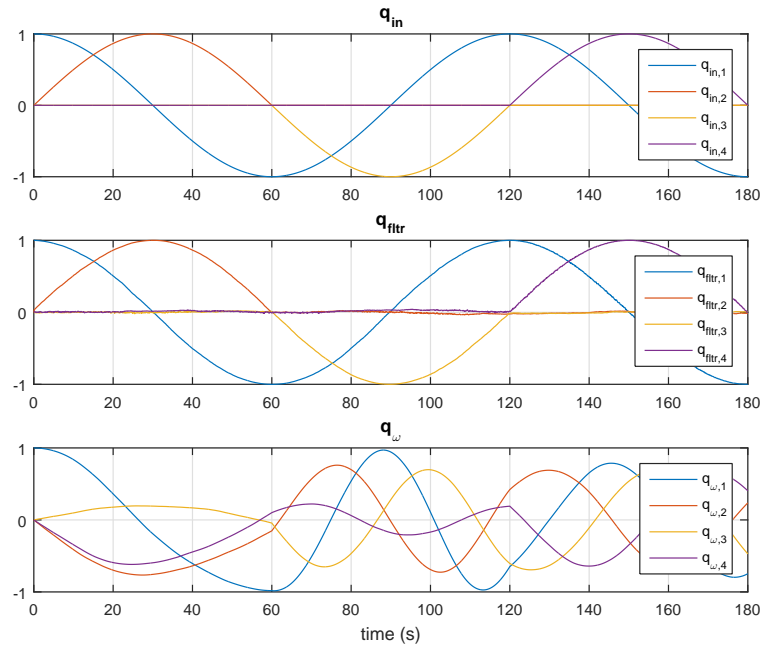


Figure 7.11 : Attitude plots: simulated input q_{in} , estimated from the complementary filter q_{filtr} and derived from gyroscopic data q_{ω} , for test case 4.

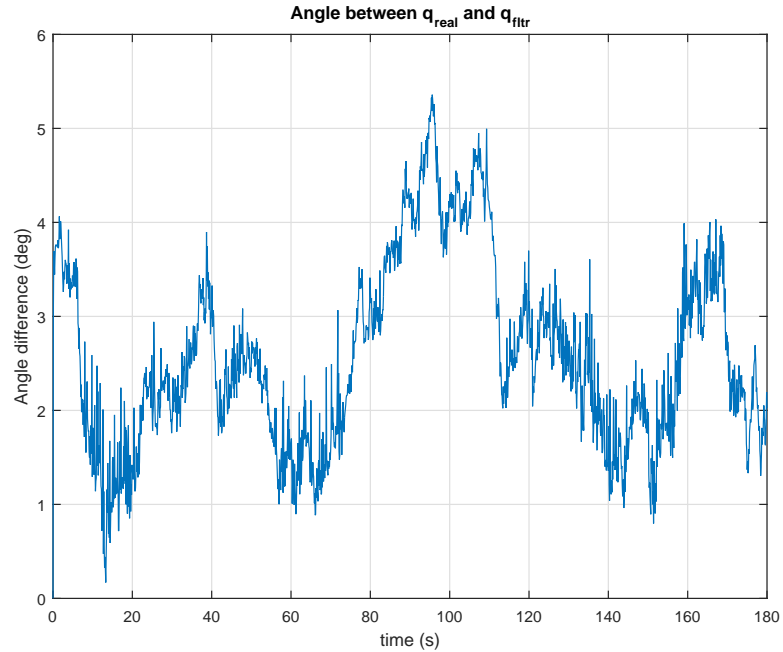


Figure 7.12 : Plot of the attitude errors from the complementary filter's estimates for test case 4.

We observe from Figure 7.12 that the filter's attitude estimate was bounded within 8° of error with some oscillations. The increase in error magnitude and noise levels in q_{fltr} were due to combinations of the bias errors in the sensors plus their combined measurement noise. Overall the filter performance shows improvement over the attitude estimate derived using only commercial grade gyroscopic measurements.

Test Case 5

In this test case the performance of the attitude filter was estimated when using simulated sensor data from a tactical grade gyroscope, accelerometer, and magnetometer. In Figure 7.13 show the plots of the simulated sensor measurements used for this test. Note the difference in bias error between a tactical grade IMU, Figure 7.13, and a commercial grade IMU, in Figure 7.10.

The resulting attitude estimate from the filter, q_{fltr} , was plotted in Figure 7.14 along with the simulated system's input attitude q_{in} and the attitude estimate derived using only gyroscopic data q_w . It is worth noting that q_w exhibited a better

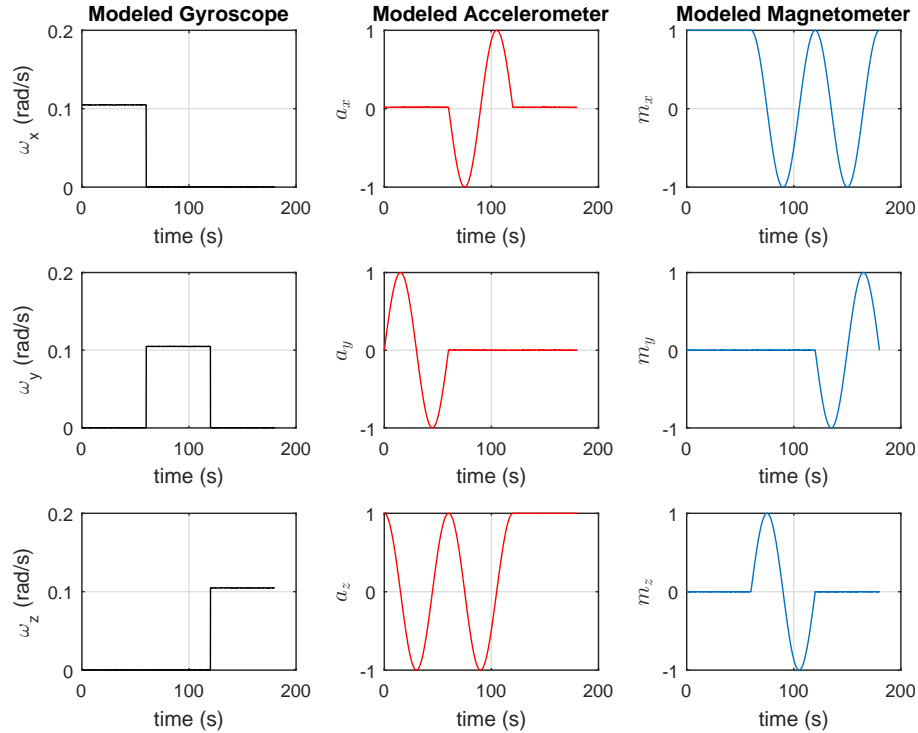


Figure 7.13 : Plot of simulated tactical grade gyroscope, accelerometer, and magnetometer measurements

performance than q_{flt} , in this short test period. This improvement in q_w 's estimates was largely due to the improved bias performance in the gyroscope measurements. q_w would eventually drift, without bound, without any external feedback given a longer timescale. A plot of the error in the filter's attitude estimate, for this test, was plotted in Figure 7.15. Judging from the error performance plot, the attitude errors were bounded within 2° s, and exhibit some oscillations. The attitude estimate oscillations were a result of the small bias errors present in the accelerometer's measurements.

Analysis of Attitude Filter's Simulated Tests

From the simulated test we could observe that the Attitude complementary filter was capable of tracking the system attitude, by fusing data from calibrated gyroscope,

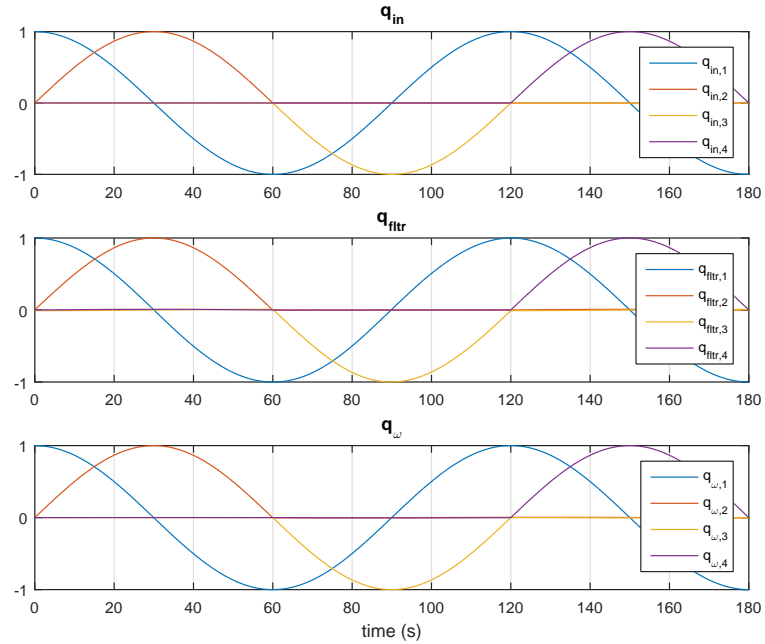


Figure 7.14 : Attitude plots: simulated input q_{in} , estimated from the complementary filter q_{flt} and derived from gyroscopic data q_w , for test case 5.

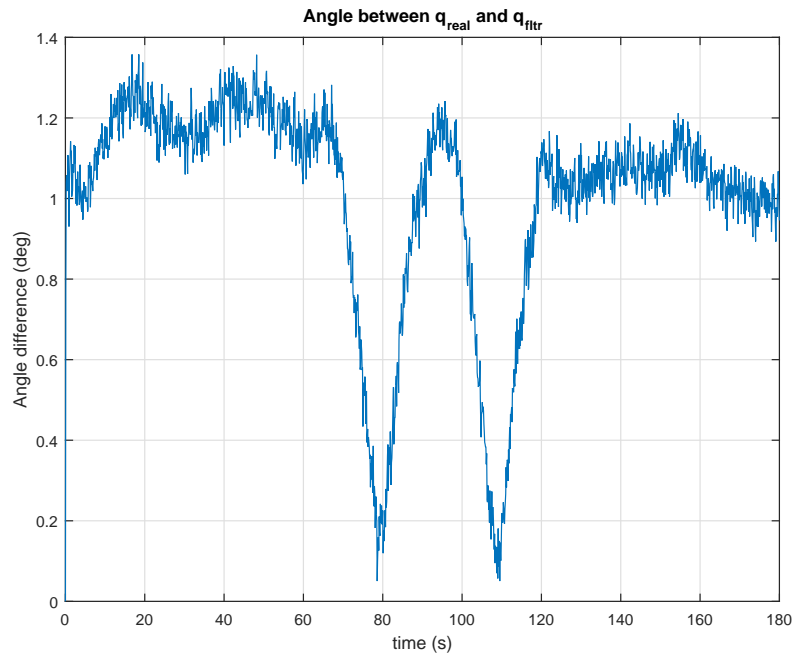


Figure 7.15 : Plot of the filter's attitude estimate error

accelerometer, and magnetometer sensors. Although filter's attitude estimates exhibited error, these were bounded in time and were directly related to the sensor's performance grade. It was possible to obtain better performance from the filter, by fine

tuning the filter’s gains to the FV dynamics and actual sensor performance. This will require the execution of controlled test on the vehicle with an external independent attitude reference that is more accurate than the filters’s performance. The difference between the filter attitude between the filter and the external reference would then be used to tune the filter’s gains to maximize its performance.

In its current form the attitude complementary filter was susceptible to errors resulting from vehicle acceleration, as these would inevitably change the accelerometer’s estimate of the local vertical. If these acceleration events were short lived, then the error would be mitigated by the filter and completely removed when the accelerations end. But prolonged vehicle accelerations have a detrimental effect on the filter’s attitude estimate performance. Corrupting magnetic fields would have similar effect on the attitude estimates derived from the magnetometer’s measurements. this type of error can be mitigated by implementing an adaptive gain scheme, similar to that presented in [3]. However such an implementation is out of the scope of this thesis and left as a potential future work.

7.2 Horizontal Position Particle Filter (HPPF) Tests

7.2.1 HPPF Tests With Simulated Data Sets

This section presents the results from a series of tests performed on different configuration of the HPPF, using simulated data sets. These Test were performed with the objective of estimating the filter’s horizontal positioning performance under different filter configurations. All of the tests were performed on the same 17min and 33s simulated FV deployment, at Latitude 19.88 and Longitude 64.38. The location is marked in an contour plot of the anomaly fields in a ocean section just north of Puerto Rico in Figure 7.16 . The location was chosen because of its relatively abundant magnetic features. The trajectory of the simulated deployment is plotted in Figure 7.17 . As explained in Chapter 2, geomagnetic navigation is concerned with estimating the vehicle’s Latitude and Longitude coordinates on the n-frame. For this

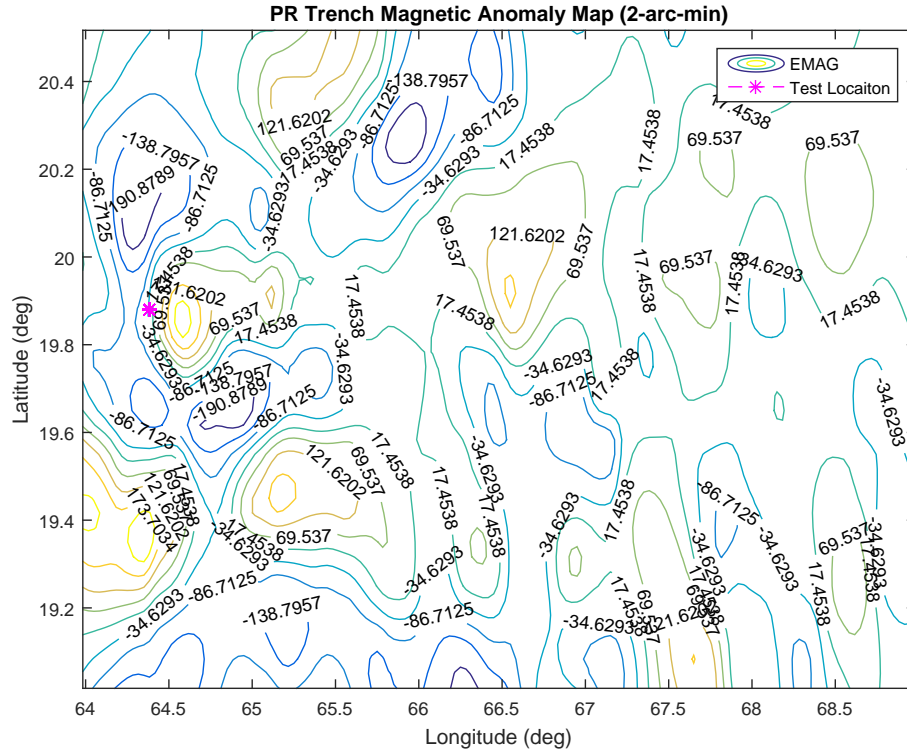


Figure 7.16 : HPPF Simulated Test Location

reason only data from the north-east plane of the FV trajectory were considered in these tests.

The magnetic samples gathered by the FV were simulated by sampling the EMAG map at the FV simulated location and adding to it, Gaussian noise with a zero mean and a 1nT standard deviation. For each test, 1000 particles were instantiated within 10m of the starting location of the FV, with zero initial velocities and attitude errors less than 1° . Particle Re-sampling was performed when the ESS estimate was below 400 particles.

Test Case 1: 1nT Magnetic Measurement

The tests presented in this section were made with the assumption that the remaining error in the magnetic measurement model, have a zero mean and 1nT standard deviation. Such a test case is representative of an optimal condition for magnetic

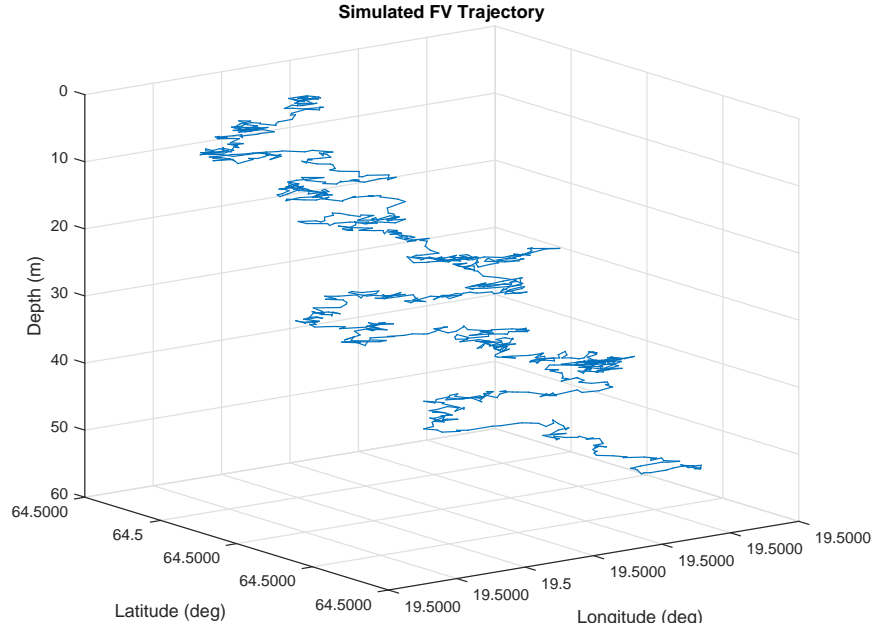


Figure 7.17 : Simulated FV Deployment Trajectory

navigation: the availability of an accurate magnetic anomaly map and the capability to accurately sample the magnetic anomaly field.

The first test was performed using the INS system model introduced in Section 6.6.2, with the performance parameters of a navigation grade IMU (see Table 6.1). A plot of the HPPF estimated vehicle position of the vehicle is shown in Figure 7.18, together with the input position of the simulated FV deployment. All position plots were made over the contour plot of the EMAG magnetic anomaly map. Judging from the plot of the HPPF position estimate, its solution drifted southward from the FV true location. A plot of the east and north positioning errors for this test is shown in Figure 7.19. From the error plot it is observed that the position errors in the east axis (max 43m) were relatively smaller than the errors in the north axis (max of 504m). This difference in positioning performance can be explained by noting that the magnetic contour lines at the deployment location run almost parallel to the north axis, as seen in Figure 7.18.

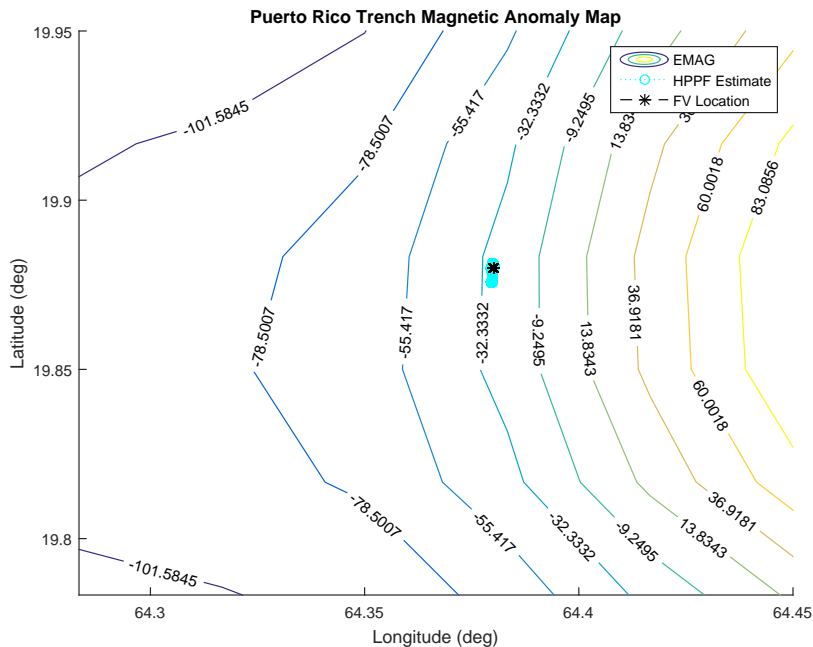


Figure 7.18 : HPPF estimate location of FV using INS system model and navigation grade IMU parameters

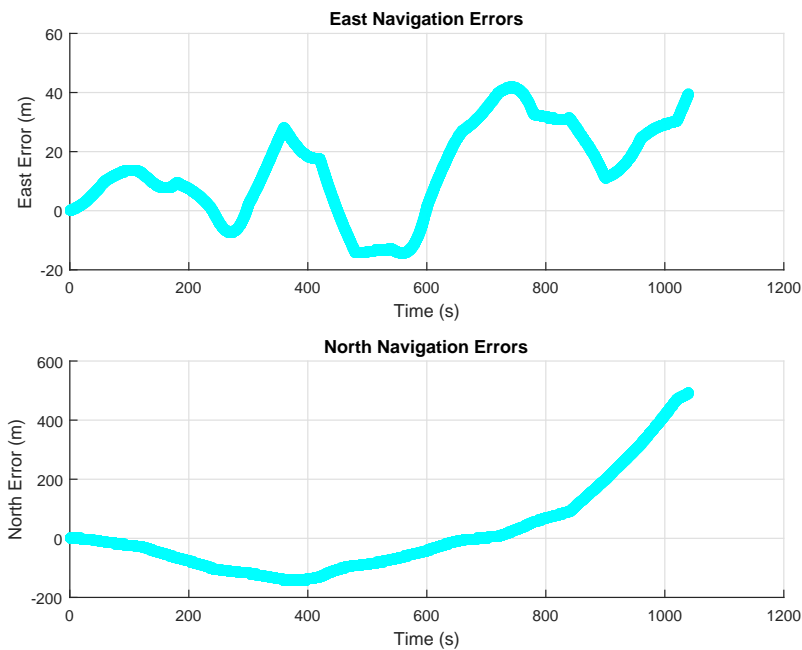


Figure 7.19 : HPPF position estimate errors in the east and north axes while using a navigation grade IMU and the INS system model.

In the prediction phase of the HPPF, the particle's were spread in an uniform fashion from their starting location, via the INS system model. An example of a 10min

particle spread, is shown in the plots (A) and (B) of Figure 7.20 . In the update phase, a magnetic anomaly sample was taken for each particle based on its predicted position on the EMAG map. Each particle’s magnetic signature was then compared to magnetic samples taken from the FV via the likelihood equation. Because the contour for the FV magnetic signature runs from south to north at the test location, particles near the contour line were assigned the highest weights even if they had drifted from the FV actual position. An example plot of this event is shown in plot (C) of Figure 7.20 . Another explanation for the HPPF position estimate drift is that the particle spread caused by the INS system model, with navigation grade IMU parameters (1k position error per hour), was greater than the expected FV horizontal displacement (40m per hour). This overestimation of the FV horizontal displacement made more likely the movement of particles move over the contour lines of a given magnetic signature.

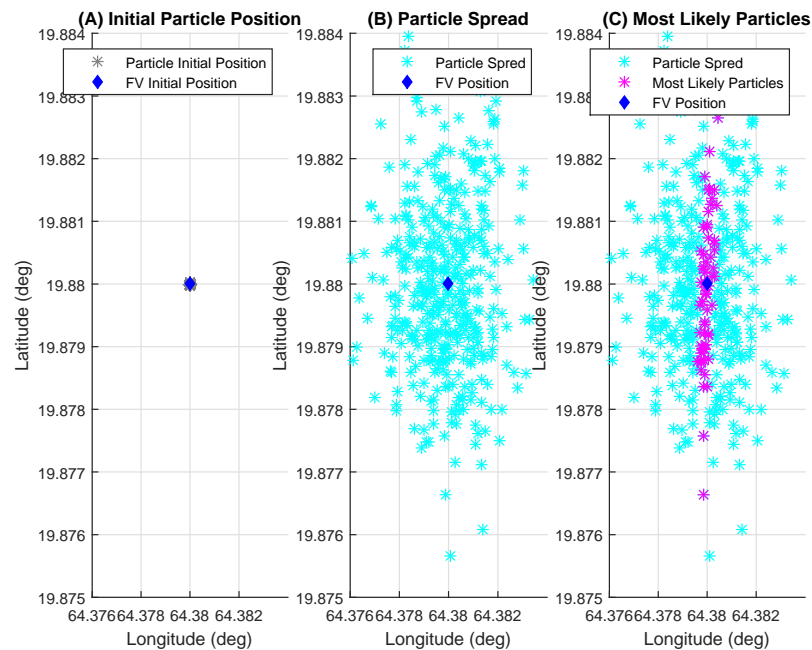


Figure 7.20 : Plot(A): state of HPPF particles at the start of the prediction phase. Plot(B): particle spread caused by the INS system model with navigation grade IMU parameters for a period of 10 minutes. Plot(C): a plot of the most likely particles (top 30%) based on the FV magnetic sample and likelihood equation.

A plot of the FV simulated magnetic samples and the weighted average magnetic signature from the particles of the HPPF are shown in Figure 7.21 . It is observed from the plot that the HPPF were from of particles with a magnetic signature that resembles the FV sampled anomaly magnetic field.

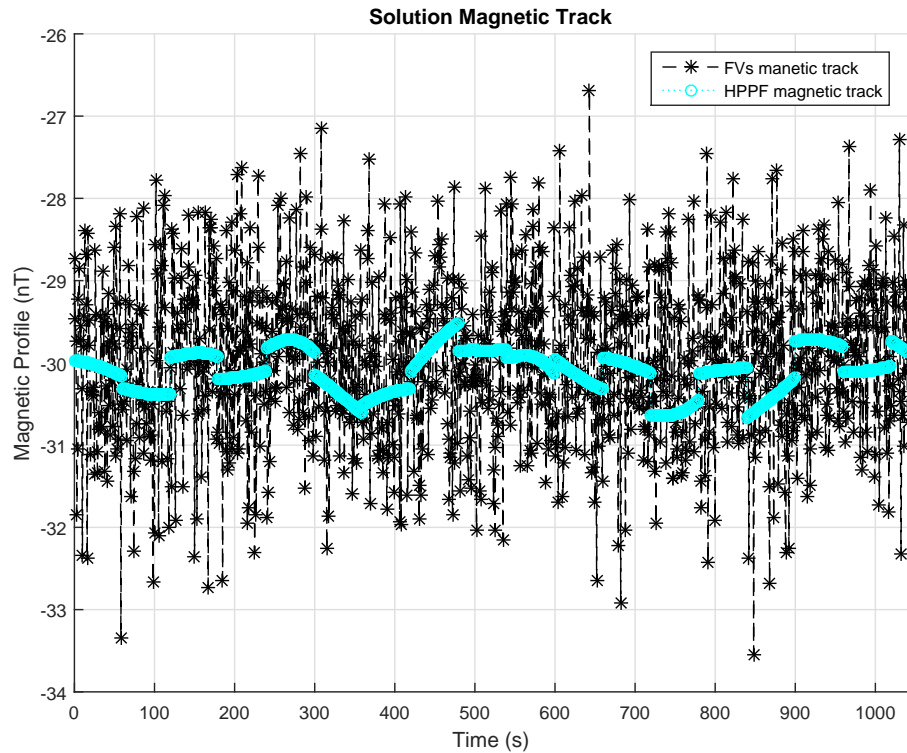


Figure 7.21 : Plot of the simulated FV magnetic samples and the weighted average of the particle's magnetic sample from HPPF.

A second test was performed using the same INS system model but with the performance parameters of a tactical grade IMU. The HPPF estimate position for this test were plotted in Figure 7.22 . The positioning errors in the east and north axes were plotted in Figure 7.23 .From the error plot it is observed that the position error in the filter's estimate increased. This was due to the increase in particle spread caused by downgrading the IMU's performance parameters. In Figure 7.22 we can also observe the HPPF tendency to "follow" the magnetic contour lines on the map.

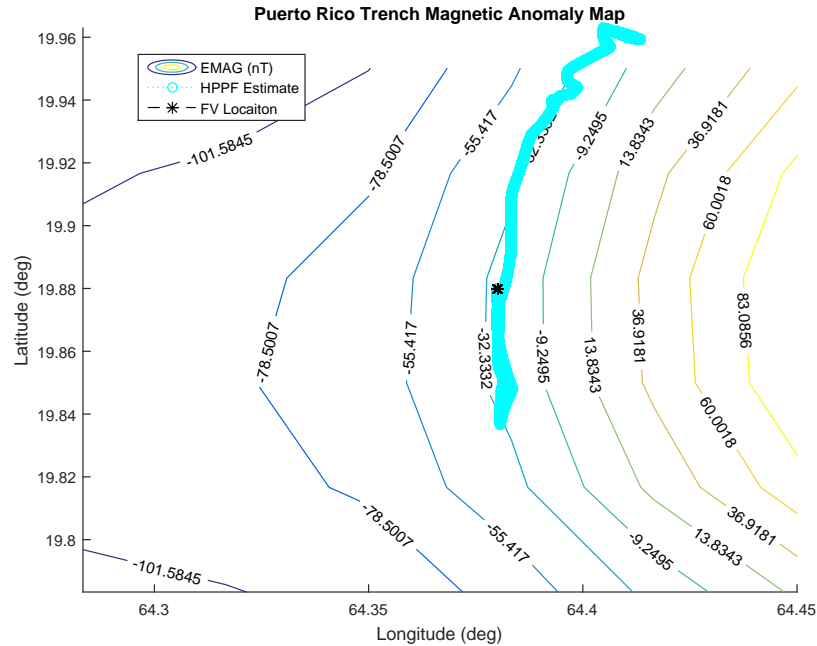


Figure 7.22 : HPPF estimate location of FV using INS system model and tactical grade IMU parameters

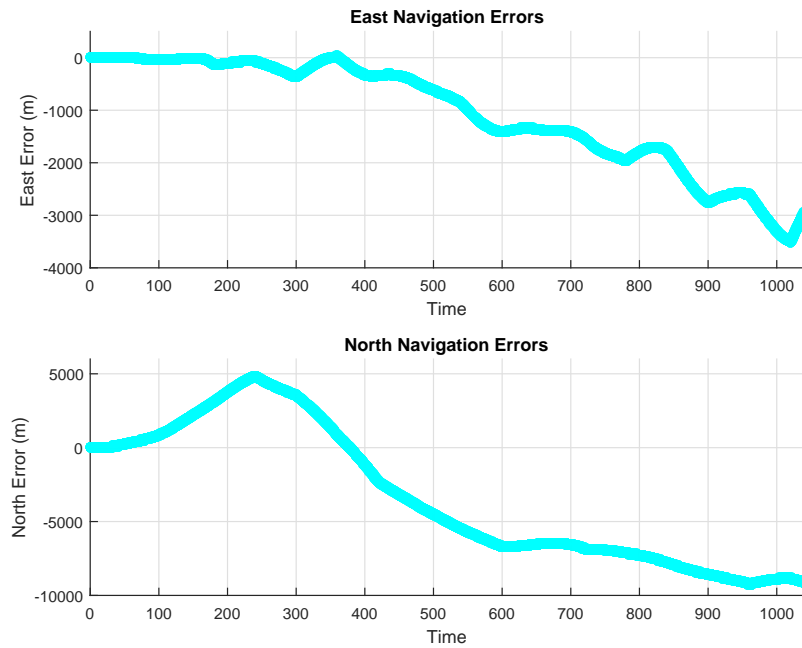


Figure 7.23 : HPPF position estimate errors in the east and north axis, using the INS system model and the performance parameters of a tactical grade IMU.

The magnetic track of the simulated FV samples and the weighted average of the particle's magnetic signature are plotted in Figure 7.24 . From the plot it is

observed that the HPPF attempted to track the magnetic signature sampled by the FV but because of the larger particle spread, its position estimate drifted away from the FV location, following the corresponding contour line.

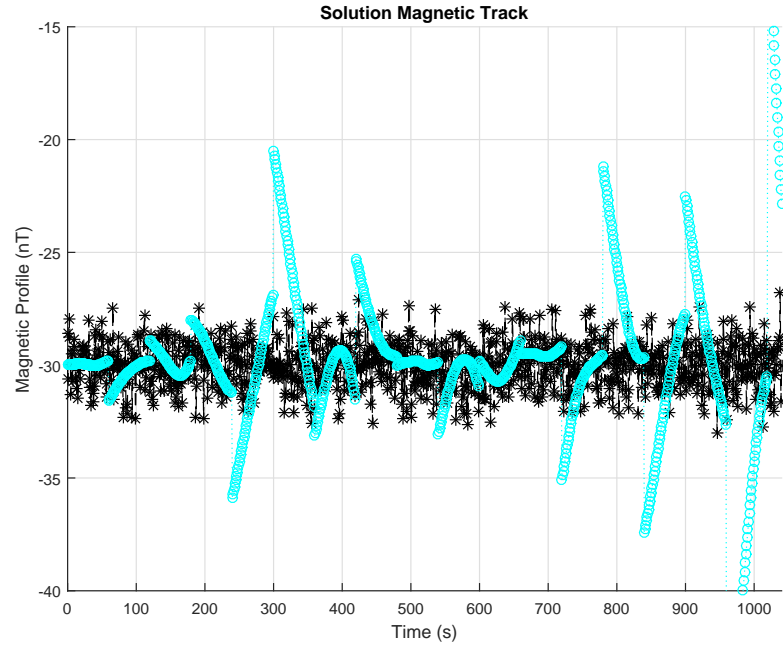


Figure 7.24 : Plot of the simulated FV magnetic sample and the weighted average of the particle's magnetic sample from HPPF.

The third test performed, with a magnetic measurement error of 1nT, was performed using the first order Gauss-Markov acceleration (FOGMPA) system model, (Section 6.6.2). The model used parameters $\tau = 100$ and $\omega = 2.2361e - 05$ for the both north and east axes of the model. These parameters are representative of the FV expected horizontal displacements. Figure 7.25 plots 1000 Monte Carlo simulations, with a duration of 1000s, each of the north axis of the FOGMPA model with the given model parameters. Note that the predicted spread from the model has zero mean but a standard deviation of 10m, closely approximating the FV expected horizontal displacement.

The HPPF position estimate is plotted in Figure 7.26 and the plots of the HPPF error is shown in Figure 7.27 . Note that because the FOGMPA model

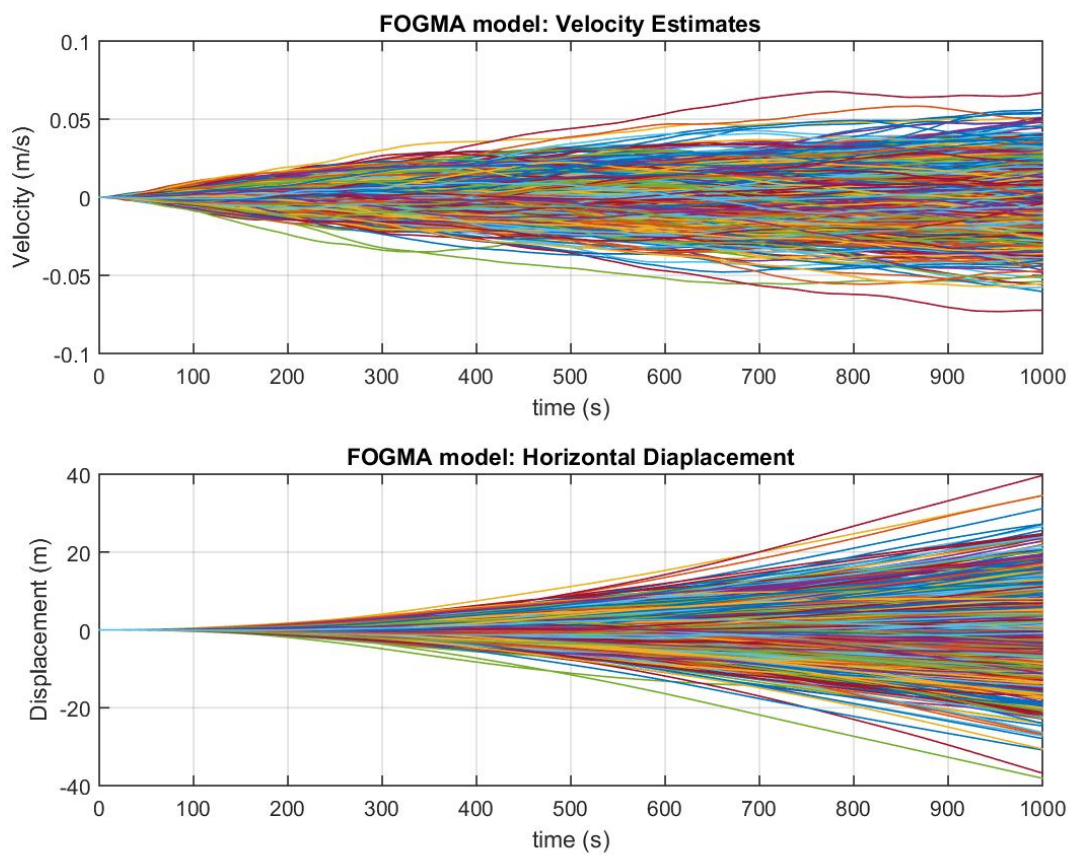


Figure 7.25 : 1000 Monte Carlo simulation of the FOGMPA system model of the HPPF

approximates the expected horizontal displacements of the FV, the HPPF particles were not allowed to spread as far, as when using the INS model. This limited spread of the filter's particles improved the HPPF ability to estimate the position of the FV.

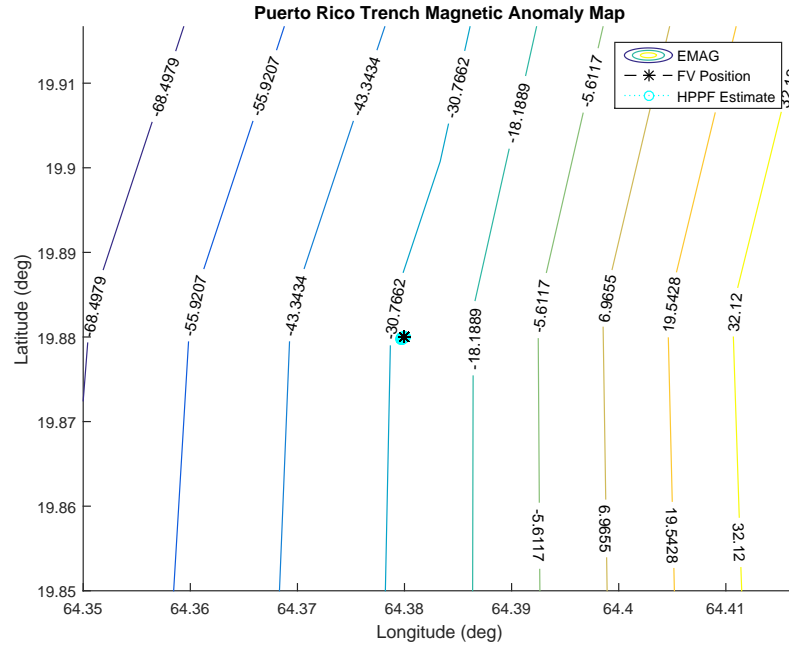


Figure 7.26 : Plot of HPPF estimate location of FV using FOGMA system model

A second simulation test was performed using the a magnetic measurement model of 1nT and the FOGMPA model. This time the simulation duration was increased from 17min to 1 hour. The results for the simulation are presented in Figures 7.28 and 7.29 . Because of the limited particle spread of the FOGMPA model, the HPPF estimates did no exhibit a tendency to follow the contour lines of the anomaly map, hence improving the HPPF position estimate performance.

Test Case 2: 10nT Magnetic Measurement

The tests presented in this section were made with the assumption that the remaining error in the magnetic measurement model had zero mean and a standard deviation of $10nT$. In a fashion similar to the HPPF Test Case 1, most of the tests were also performed in the 17min and 33s simulated FV deployment presented

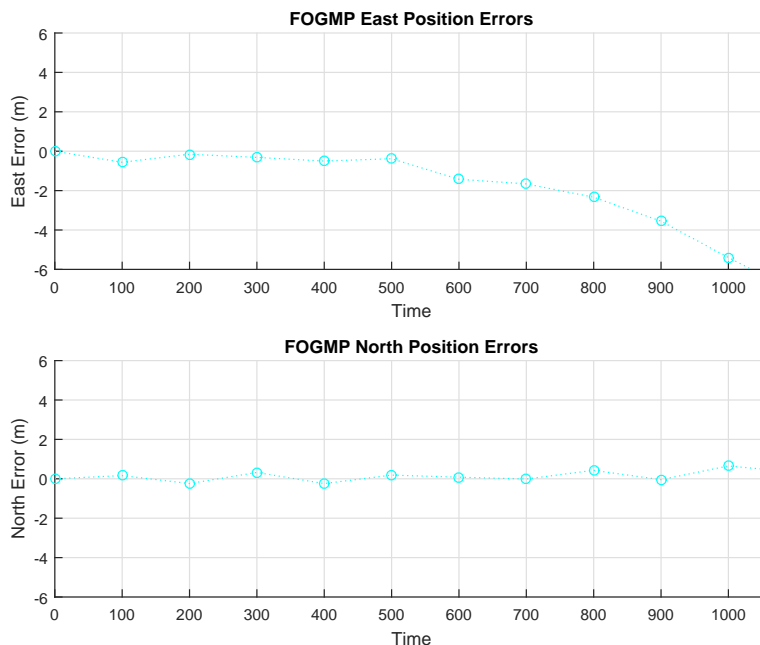


Figure 7.27 : HPPF position estimate errors in the east and north axis using the FOGMA system model.

earlier. The magnetic samples from the FV were simulated in the same fashion as well, sampling the EMAG map at the FV simulated location and adding a white Gaussian error of zero mean and 10nT.

The first test was performed using the INS system model with the performance parameters of a navigation grade IMU. The HPPF estimates of the FV position is presented in Figure 7.30 . From the plot, we can observe that the HPPP's performance was similar to that in Test Case 1, for the same system model configuration. The error plots, shown in Figure 7.31 , denote a bounded error in the east position estimates as the axis runs perpendicular to the local magnetic contours. While the north position error is larger because the axis runs almost parallel to the local contour curves. Notice that the HPPF estimate still exhibit a tendency to "follow" the local magnetic contour lines in its effort to estimate the FV location.

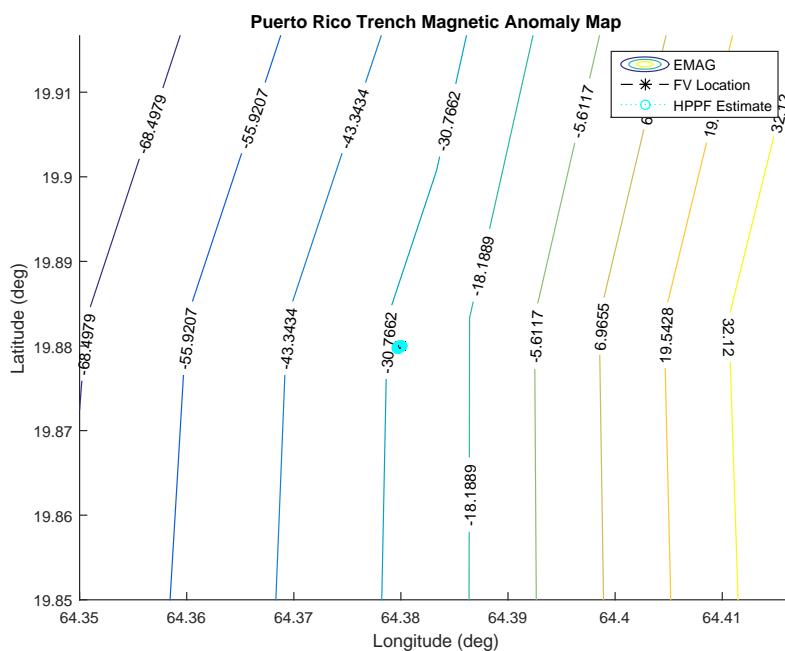


Figure 7.28 : Plot of HPPF estimate location of FV using FOGMA system model for a simulated deployment of 1 hour.

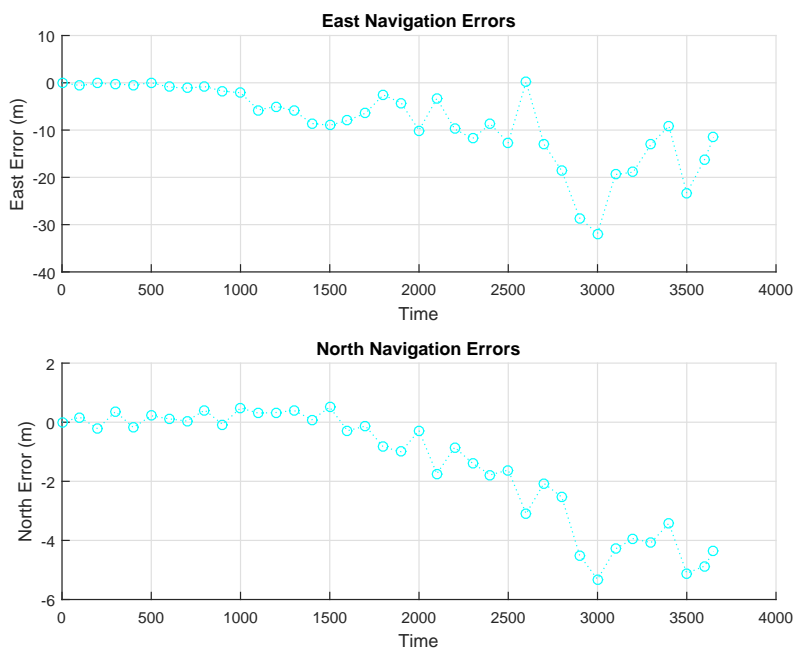


Figure 7.29 : HPPF position estimate errors in the east and north axes using the FOGMOPA system model on a 1hour simulated deployment

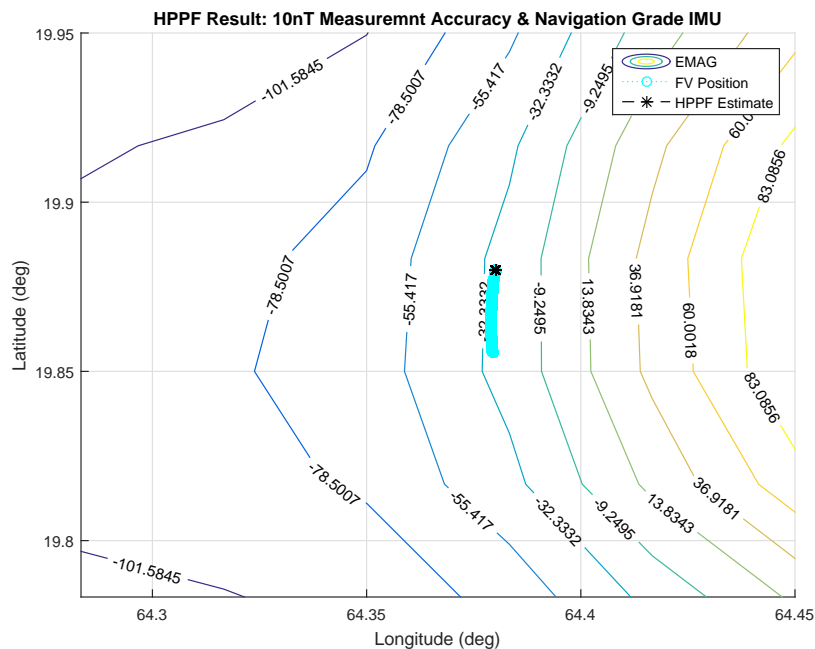


Figure 7.30 : HPPF estimate location of FV using a 10nT measurement model and INS system model with navigation grade IMU parameters

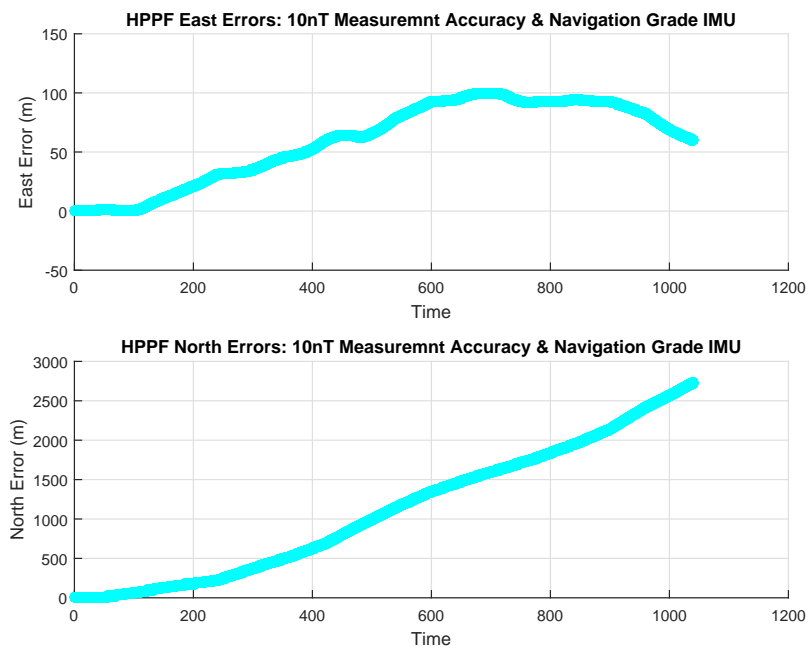


Figure 7.31 : HPPF position estimate errors in the east and north axes, with a 10nT measurement model and a navigation grade IMU system model.

The HPPF tendency to follow local magnetic contour lines when using INS system model is more noticeable when the IMU parameter are degraded, like the following test. The second test, under the assumption of a 10nT accuracy, in magnetic

measurements, was performed using tactical grade IMU parameters in the INS system model. The HPPF position estimate is plotted in Figure 7.32. Similar performance to its corresponding test, in Test Case 1, is observed. The position error for the test shown plotted in Figure 7.33. As the tactical grade INS system model predicts a greater particle spread, the HPPF estimates are further away from the FV location but on the same contour line.

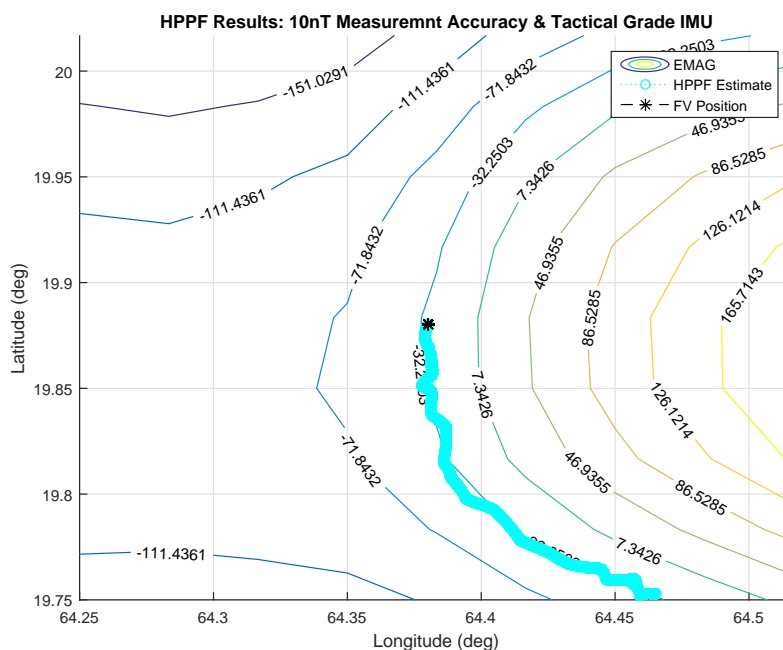


Figure 7.32 : HPPF estimate location of FV using a 10nT measurement model and INS system model with tactical grade IMU parameters

The third performed test used the FOGMPA model parameters that approximated the FV horizontal displacements. The HPPF position estimate and errors are plotted in Figures 7.34 and 7.35. Again the FOGMPA system model exhibits better positioning performance than its INS counterpart.

A simulated test of 1 hour using the FOGMPA model was also performed for this test case. Test results are plotted in Figure 7.36 and the corresponding error are in Figure 7.37. A performance similar that in Test Case 1 was observed. A total positioning error within 100m with a larger estimation error in the north axis.

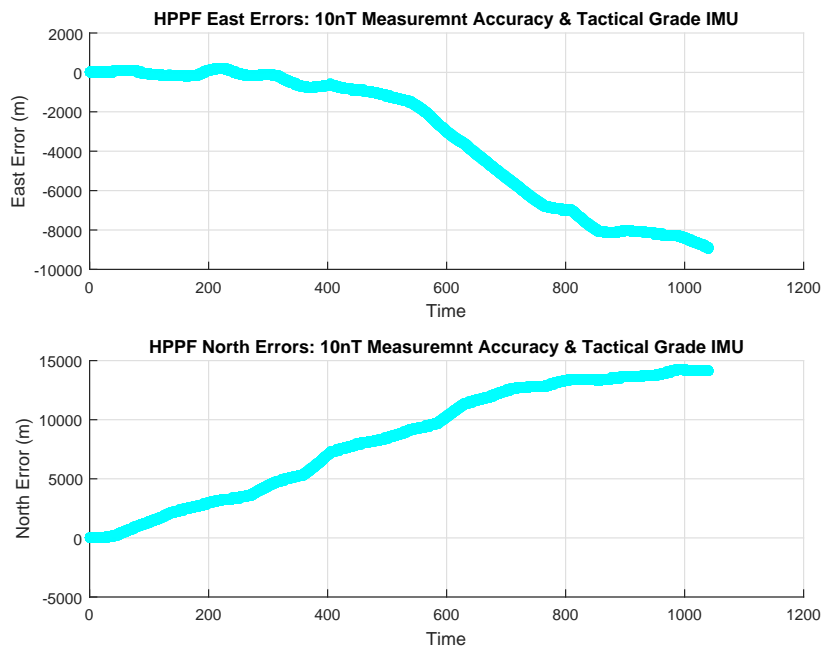


Figure 7.33 : HPPF position estimate errors in the east and north axis, with a 10nT measurement model and a tactical grade IMU system model.

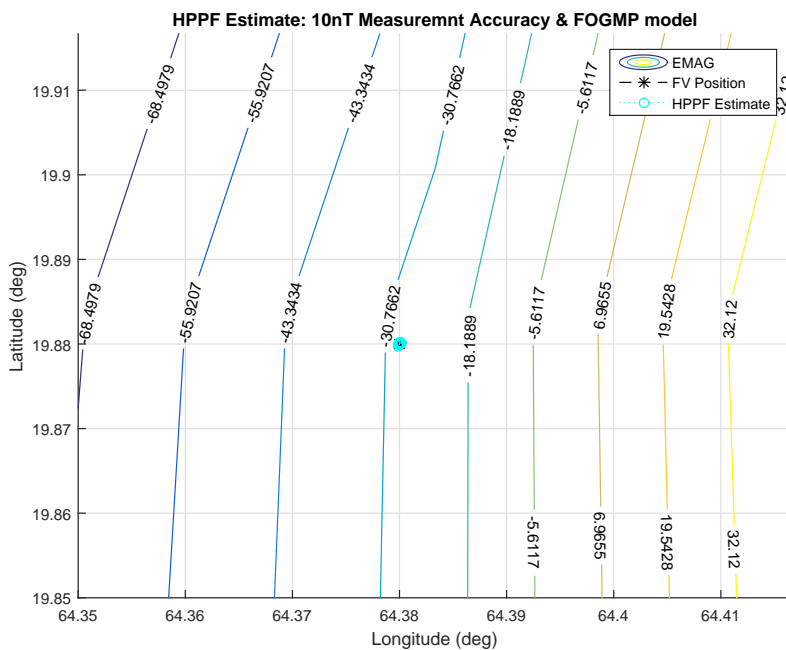


Figure 7.34 : HPPF estimate location of FV using a 10nT measurement model and the FOGMPA system model.

Test Case 3: 1nT Magnetic Measurement

The tests presented in this section were performed with the assumption that the remaining error in the magnetic measurement model had a zero mean and a standard

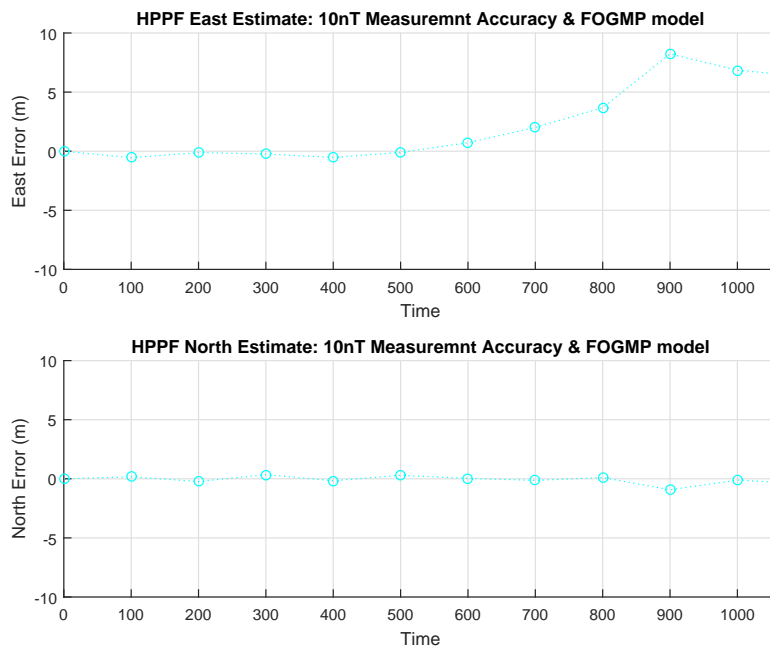


Figure 7.35 : HPPF position estimate errors in the east and north axis, with a 10nT measurement model and the FOGMPA system model.

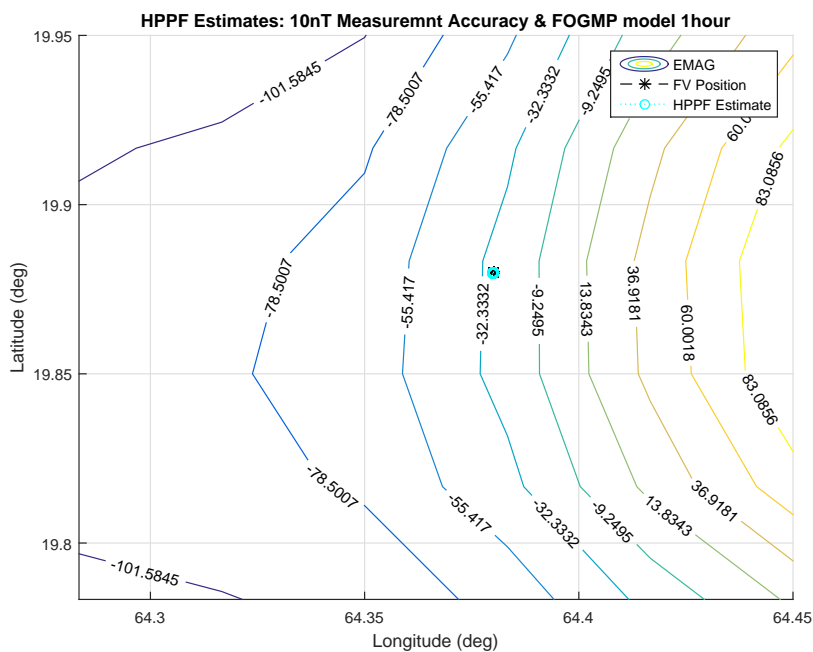


Figure 7.36 : HPPF estimate location of FV using a 10nT measurement model and the FOGMPA system model for a simulation time of 1hour.

deviation of $50nT$. Because of the poor position performance of the INS system in the HPPF, see Test Cases 1 and 2, the INS system models were not used. Instead,

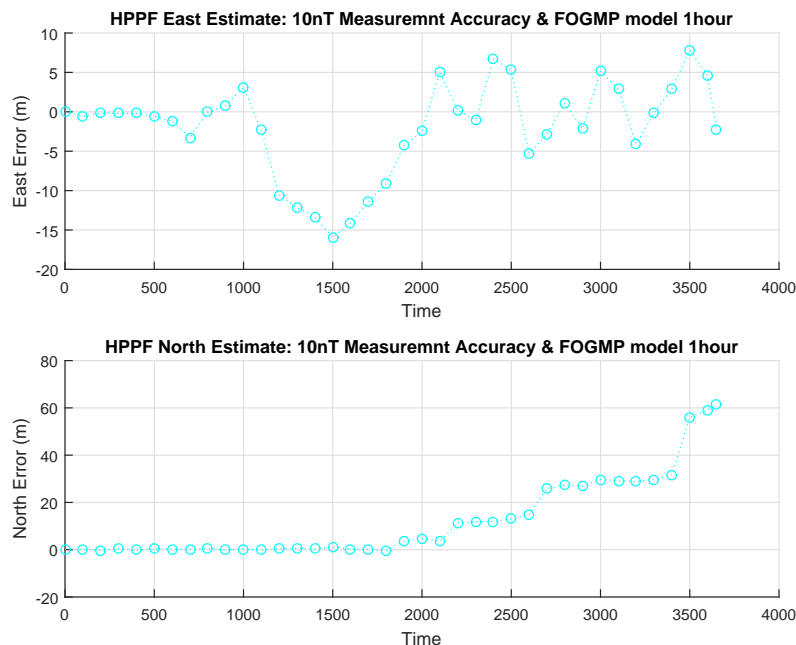


Figure 7.37 : HPPF position estimate errors in the east and north axes, with a 10nT measurement model and the FOGMPA system model for a simulation time of 1hour.

only the FOGMPA system model was tested to gain insight on the expected HPPF estimation performance. The results from the tests are plotted in Figures 7.38 and 7.39 .

Although not evident in the result plots, the magnetic navigation algorithm was not able to provide any positional feedback to the HPPF. This stems from the fact that at the end of the 1-hour simulation, the positional spread from the FOGMPA model is at most 60m from any two of the filter particles. Because of the small horizontal gradients from the EMAG map, no particle group had a sufficiently different magnetic signature to be uniquely identify by the Likelihood equation, during the whole test duration. A histogram of the final particle weights for the test is plotted in Figure 7.40 . Note that no one group of particle have distinct weight assigned to them.

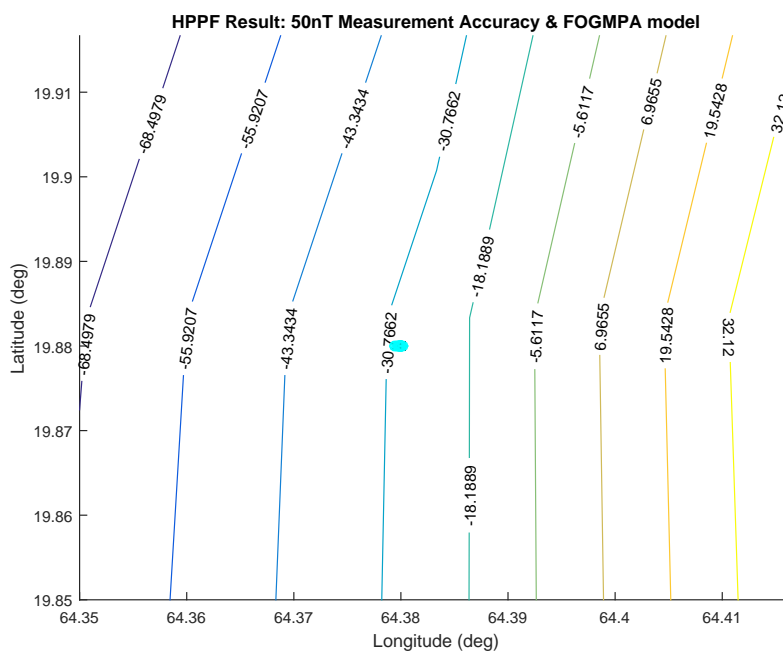


Figure 7.38 : HPPF estimate location of FV using a 10nT measurement model and the FOGMPA system model for a simulation time of 1hour.

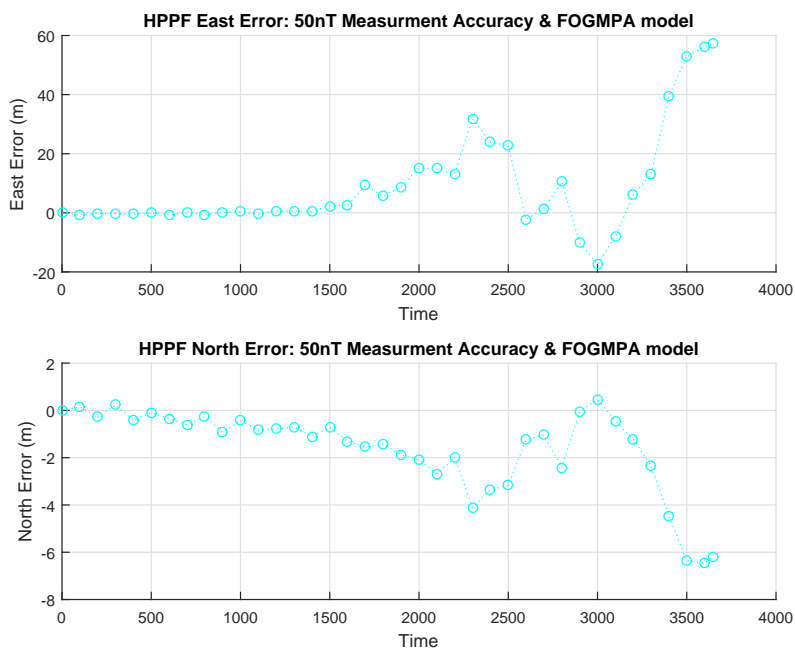


Figure 7.39 : HPPF position estimate errors in the east and north axis, with a 50nT measurement model and the FOGMPA system model, for a test time of 1hour.



Figure 7.40 : Histogram of HPPF particle weights at the end of the test, for a measurement model of 50nT

Analysis and Conclusion for the HPPF Tests Using Simulated Data Sets

From the results of the tests performed of the DPF with simulated data sets, we can conclude that the INS system models are inadequate for the current mechanization of the HPPF. The inadequacy of the INS system model stems from the fact that the expected positioning error from a navigation grade IMU (1km per hour) dwarf the expected horizontal displacements of the FV (40m per hour), resulting horizontal displacements that are unfeasible for an FV. The FOGMPA model resulted more adequate in describing the FV displacements and produced the most accurate results.

Because of the subtle changes in the magnetic anomaly field intensity in the EMAG, in order for the HPP's to provide position estimation feedback on the FV location it is necessary that the resulting magnetic measurement model have a residual error of 10nT or less. Implying that residual error from the calibrated magnetometer, mapping error, error from the WMM model, and error for the compensation of the ionospheric magnetic interference, all sum to an error with approximately zero

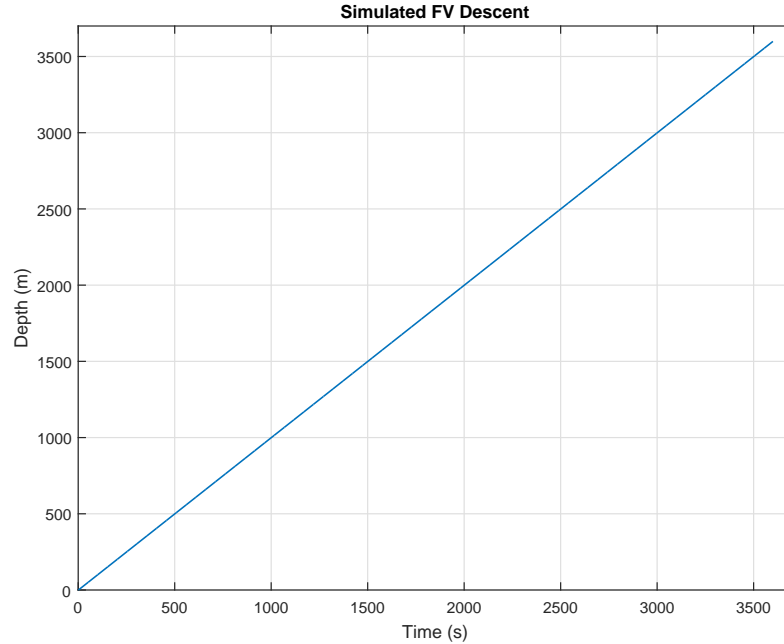


Figure 7.41 : FV Simulated Descent

mean and a standard deviation of 10nT or less. This is no small feat, as the level of magnetometer calibration alone requires highly specialized tooling and a controlled magnetic environment. This level of magnetic measurement accuracy usually achievable by geomagnetic survey entities [59]

7.3 Depth Particle Filter Tests

7.3.1 DPF Test With Simulated Data

This section presents the results of the tests performed on the DPF. For these tests it was assumed that the residual error from the depth measurement model, Equation 2.21, had a white Gaussian error with zero mean and a standard deviation of 10m. All tests performed on the DPF used the vertical descent data from the same simulated FV deployment. A plot of the FV descent used for these tests is shown in Figure 7.41. The descent duration was 1hour during which the FV reached a maximum simulated depth of 3599m.

Depth measurement were simulated by adding white Gaussian noise, with zero mean and 3m standard deviation, to the FV simulated depth. This measurement model is representative of a scenario where the FV is equipped with a calibrated depth pressure sensor with an accuracy of 0.03% of its depth range. Periodic depth measurements were provided to the DPF every 10s. The DPF used 1000 particles, each instantiated with an initial depth equal to that of the FV with an error of 0.5m, initial velocities set to $0m/s$, and aligned with initial attitude error of less than 1° . A particle resampling was performed when the estimated effective sample size was less than 400 particles.

Test Case 1: INS System Model with Navigation Grade Performance Parameters

In this case the DPF was tested using the INS system model with performance parameters of a navigation grade IMU. The estimated depth from the DPF is plotted in Figure 7.42. Figure 7.43 is a plot of the measured error from the pressure meter and the depth estimate errors from the DPF.

From the results plots, it was observed that the DPF is capable is estimating the FV depth fusing the data provided by a navigation grade IMU and depth measurements. In the short term the error characteristics of the DPF's estimates are better than the error characteristics of the depth meter. This is due to the relatively accurate initial condition of the particles and the slow state drift caused the navigation grade IMU. In the long term the DPF error estimate performance is similar to that of the depth measurements, this is expected as these are the only measurements used by the filter that do not accumulate error over time.

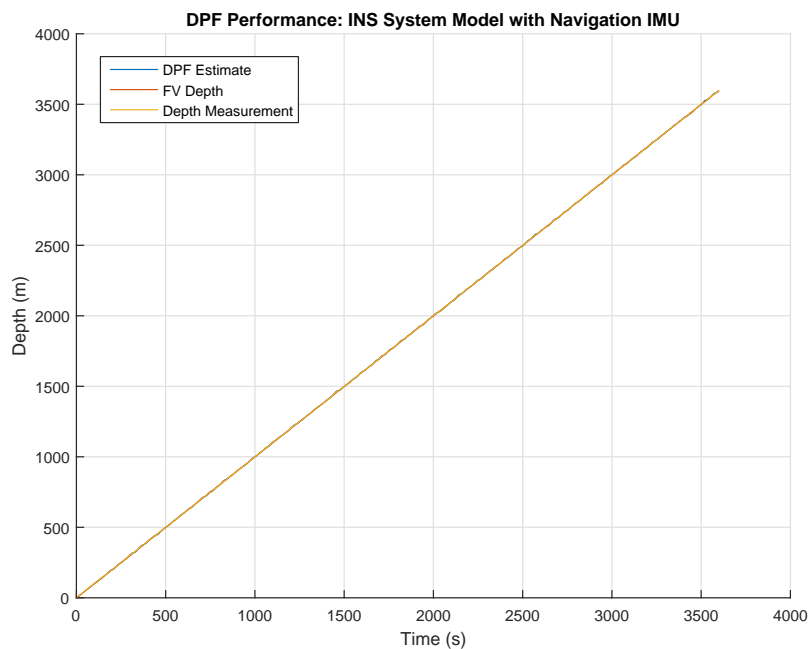


Figure 7.42 : DPF Estimation performance using the INS system model and the model parameters of a Navigation grade IMU.

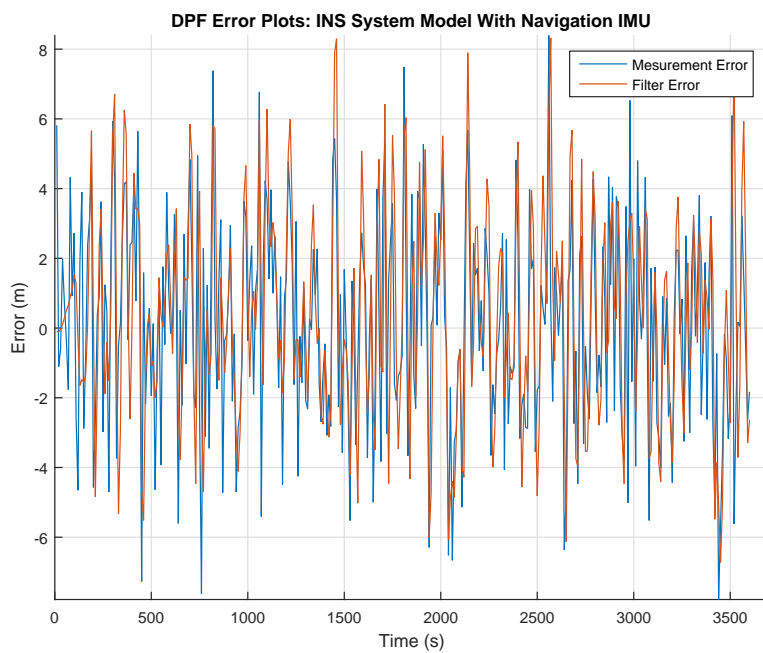


Figure 7.43 : DPF error performance using the INS system model and the model parameters of a Navigation grade IMU.

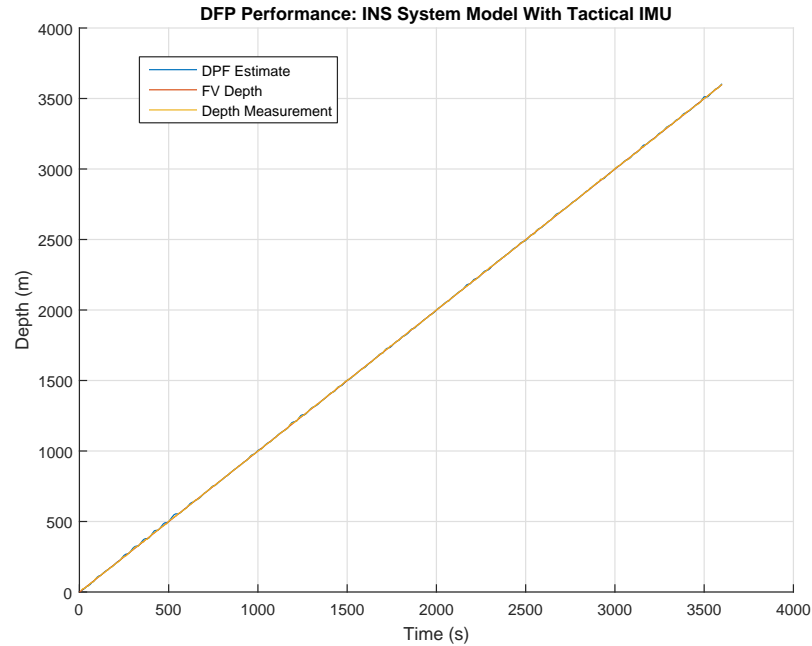


Figure 7.44 : DPF Estimation performance using the INS system model and the model parameters of a Tactical grade IMU.

Test Case 2: INS System Model with Tactical Grade Performance Parameters

This test case was meant to test the performance of the DPF using the INS system model with the performance parameters of a tactical grade IMU. The result from the test are plotted in Figures 7.44 and 7.45 .

From the results plots it is observed that the DPF was capable of estimating the FV depth by data fusion from a tactical grade IMU and a depth meter. Because of the degraded sensor performance of the IMU model, the DPF suffers from some degraded estimation performance, peak error of 20m.

Test Case 3: INS System Model with Commercial Grade Performance Parameters

This tests case was meant to test the performance of the DPF using the INS system model with the performance parameter of a commercial grade IMU. Unfortunately the error form the commercial grade IMU caused a large particle spread in the predicted depth. This error grew at a quick pace and spread the filter particles outside

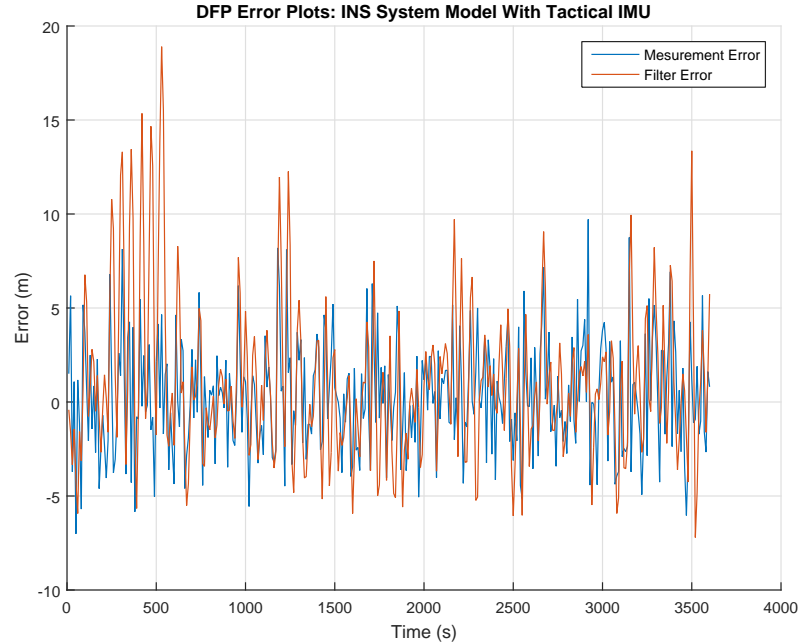


Figure 7.45 : DPF error performance using the INS system model and the model parameters of a Tactical grade IMU.

the error range of the depth measurements and consequently outside the Likelihood equation range. This caused the filter to assign every particle the same weight, even if their state estimates contradict each other and were far from the true depth of the FV. A plot of the DPF estimate is shown in Figure 7.46 . The estimation duration was cut short because later, the DPF suffered from stability error. This was somewhat an expected result as commercial grade IMU's are known for their poor dead reckoning performance. A plot of the simulated vertical acceleration measurement is shown in Figure 7.47 together with the ideal vertical acceleration of the FV.

Test Case 4: FOGMPA system Model

In this test, the depth FOGMPA model was used as the DPF's system model, with $\tau_{dpth} = 1/100$ and $\omega_{dpth} = 0.45$. A plot of 1000 Monte Carlo simulation of the FOGMPA model, with the specified parameters, is shown in Figure 7.48 .

From the plot we can observe that, for every 10s, the FOGMPA model offered a broad spectrum of vehicle states. This broad spectrum of predicted depths allows the

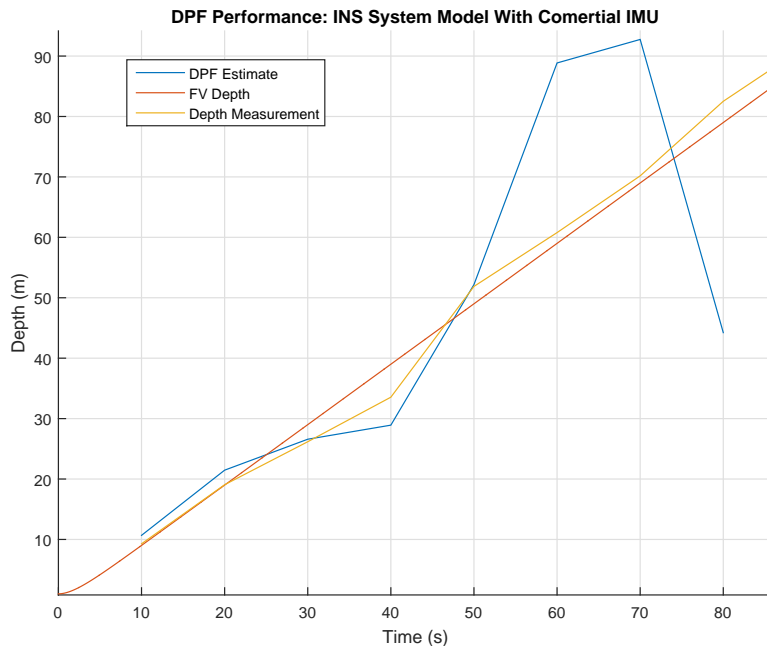


Figure 7.46 : DPF Estimation performance using the INS system model and the model parameters of a commercial grade IMU. The simulation duration was cut short from the expected 1hour duration because the filter's estimate became unstable after 90s of the simulation.

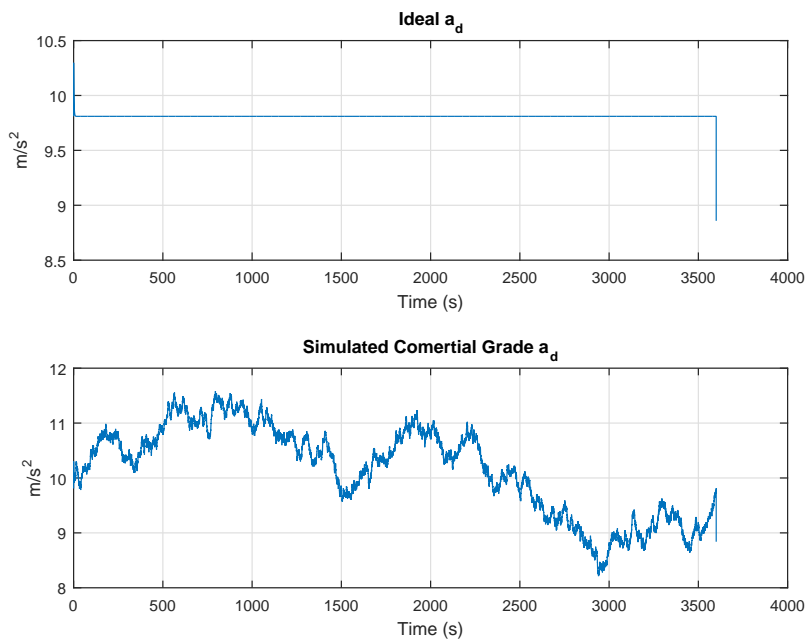


Figure 7.47 : A plot of the simulated downward acceleration using a commercial grade IMU and the ideal vertical acceleration of an FV descent.

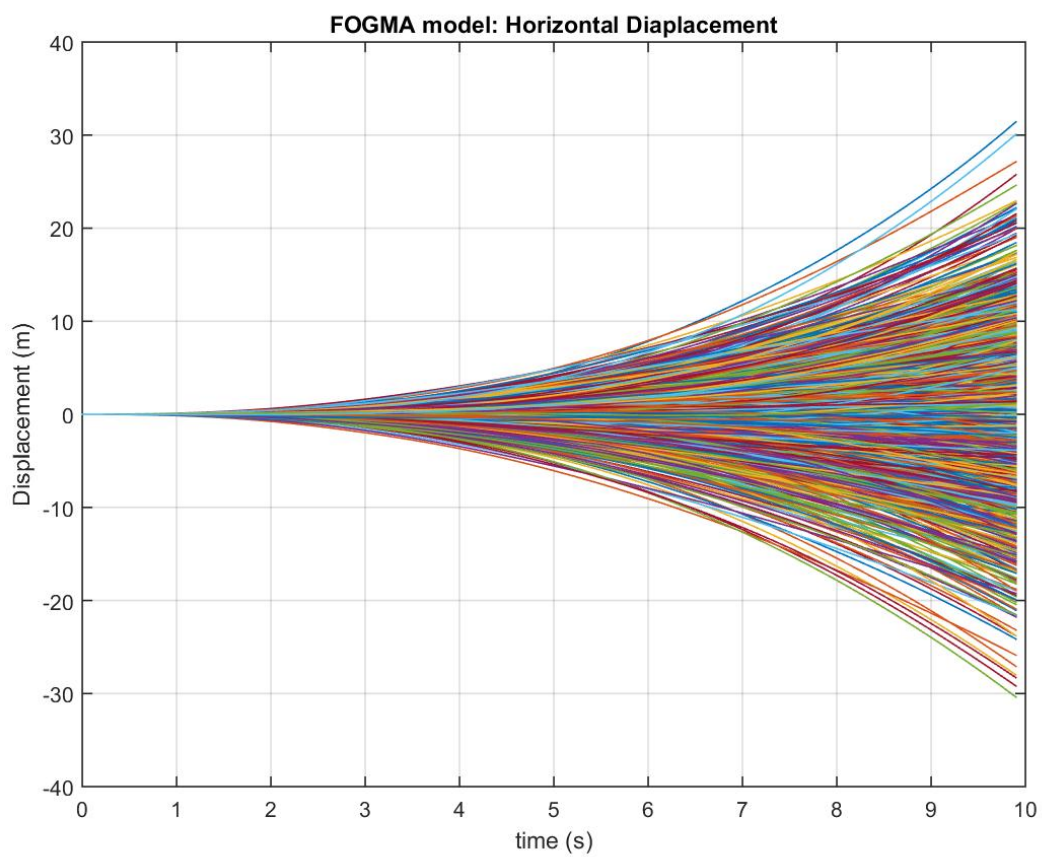


Figure 7.48 : 1000 Monte Carlo simulations of the Depth FOGMPA model

system model to encompass every potential future depth state of the vehicle. This includes if the FV landed, released its ballast in the water column or if its descending or ascending at a constant rate. Each of these states is then evaluate during the update phase and the state's closest to the measurement are chosen.

The results from the simulated experiment are plotted on the top of Figure 7.49 and their corresponding prediction errors are plotted below.

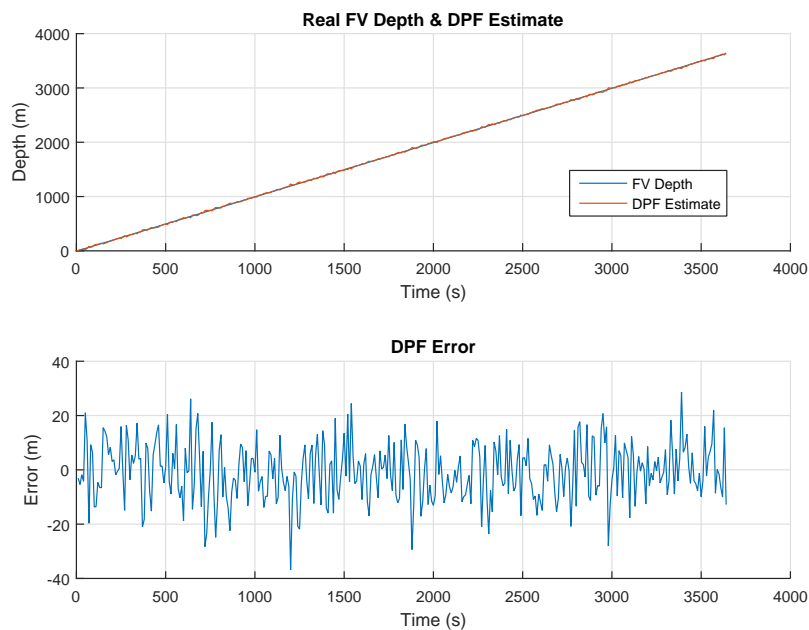


Figure 7.49 : Results of the DPF using FOGMPA model

From the error plot of the test results we could observe that the errors from the filters state did no exhibit lagging oscillatory behavior but instead more closely resembled the measurement errors from the pressure meter. This was an expected result, since the spread of the FOGMPA model has a wide spread of predicted FV depths.

Analysis and Conclusion for the DPF's Tests Using Simulated Data Sets

From the results of the test performed of the DPF, with simulated data sets, we can conclude that DPF is capable of estimating the FV depth using an INS system

model, as long as the IMU grade is tactical or greater. The poor dead reckoning performance of the commercial grade IMUs caused filter estimate instability. The DPF was also capable of estimating the FV depth when utilizing the FOGMPA model but offers little to no improvement from using the depth pressure sensor on its own. A more accurate model of the FV dynamics can improve the DPF's performance, this is left for future improvements for the DPF.

7.4 Creation of a Physically Constraint Model

As discussed in Section 7.2, the HPPF with an unconstrained geomagnetic-aided INS can produce positioning results that are physically unfeasible for an FV. Moreover, when using a commercial grade magnetometer, the navigation scheme cannot provide all the information needed to correct for accumulated INS errors. A physical constraint model (PCM) was developed to tackle these issues. The objective of such a model was to complement the HPPF by keeping its particles within the horizontal displacements that are physically feasible according to observed FV hydrodynamics. The FV hydrodynamics reported by Schmidt and Siegel (2011) [46] were the foundations for the development of the PCM. Below we describe how the PCM was developed. Subsection 7.4.1 presents the development of the PCM and Subsections 7.4.2 and 7.4.3 presents the results and analysis of the HPPF with the PCM on both simulated and field data.

7.4.1 PCM Development

When deployed, an FV quickly reaches and almost stationary state, with almost constant descent velocity, little horizontal displacements and rotates at about 1 revolution per 220s [46]. With an estimate of maximum horizontal velocity it is possible to determine a boundary of maximum horizontal displacement, from a known starting point. Let the origin of the coordinate frame, for the PMC analysis, be at the

location of FV deployments. Its x , y , and z axes point to local north, east, and down direction. let t_D represent time of the deployment, where:

- $t_D = 0$ when the FV is deployed
- $t_D = t_{lnd}$ when the FV reaches the ocean floor
- $t_D = t_{res}$ when it the FV releases its ballast
- $t_D = t_{surf}$ when the FV surfaces
- $0 < t_{lnd} \leq t_{res} < t_{surf}$
- $t_{lnd} = t_{res}$ when the FV releases the ballast while descending in the water column.

Figure 7.50 is an example FV trajectory as seen form the horizontal north-east plane with the PCM coordinate frame, t_D , and Recovery location (d_{north}, d_{east})

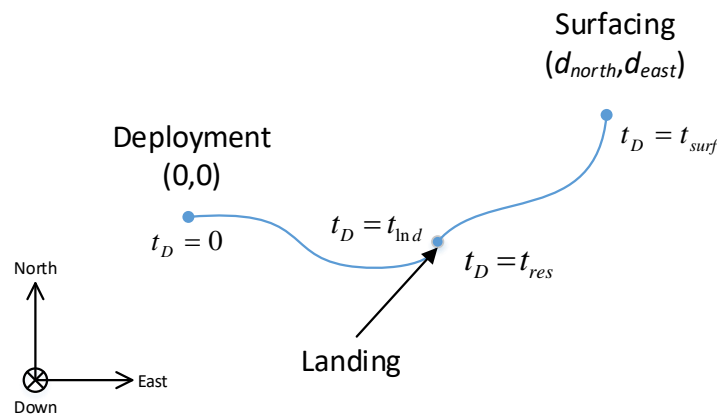


Figure 7.50 : Example FV deployment trajectory as seen in the horizontal north-east plane.

In the work by Schmidt and Siegel (2011), the authors reported a maximum ambient horizontal current of 5 cm/s at the ocean floor and a maximum horizontal current of 8 cm/s during the FV descent, in a FV deployment at the Puerto Rico trench [46]. It is important to note that horizontal currents measured during the FV descent included ambient horizontal currents, FV rotation, and horizontal displacement. Joyce *et al.*, reported an average ambient current of 5.14 cm/s at 6,000 m of depth in the Puerto Rico Trench. Using this information, a maximum horizontal

velocity during FV descent $v_{h,dsc}$ can be estimated, as in Equation 7.3.

$$v_{h,dsc} = v_{amb} + v_{hydro}, \quad (7.3)$$

where v_{amb} accounts for the maximum horizontal ambient current and is assigned a value of 5 cm/s. Term v_{hydro} accounts for the maximum horizontal FV hydrodynamic instability and is assigned a value of 5 cm/s. Resulting in $v_{h,dsc} = 10\text{cm/s}$.

During the ascent, FVs are no longer weighted down by a ballast. Instead it rises through the water column pulled by the net buoyancy force. In this configuration exhibits a higher horizontal dynamic instability, than the descent trajectory, a consequence the reduced vehicle weight. This observation is supported by analyzing the standard deviation (STD) of the FV horizontal accelerometer data for the descent and ascent periods. Table 7.1 lists the STD analysis of horizontal accelerometer data for the descent and ascent periods for ten FV deployments.

Table 7.1 : Standard deviation of FV horizontal accelerometer data.

	Deployment Date	Ascent std	Descent std
1	03-19-2015	0.13	0.15
2	03-21-2015	0.16	0.24
3	03-24-2015	0.16	0.21
4	03-30-2015	0.04	0.14
5	04-01-2015	0.04	0.14
6	03-08-2016	0.44	1.08
7	03-08-2016	0.37	1.19
8	04-09-2016	0.36	0.69
9	04-09-2016	0.29	1.10
10	04-09-2016	0.54	0.94

For this reason the v_{hydro} , in Equation 7.3, was doubled to estimate a maximum horizontal velocity during FV ascent $v_{h,asc}$, see Equation 7.4

$$v_{h,asc} = v_{amb} + 2v_{hydro} \quad (7.4)$$

Thus, $v_{h,asc}$ accounts for the maximum horizontal ambient currents and doubles the FV hydrodynamic instability, for a total of 15 cm/s.

With knowledge about the FV deployment and recovery locations as well as estimates of its maximum horizontal velocities, it is possible to determine the maximum FV horizontal displacement in time, relative to the deployment and recovery locations. Equation 7.5 represents the maximum horizontal displacement, in m, for the descent trajectory of the FV, as a function of t_D .

$$d_{dsc}(t_D) = \frac{v_{h,dsc}}{100}t_D + d_{dsc,0}, \quad (7.5)$$

where $0 \leq t_D \leq t_{lnd}$, and $d_{dsc,0}$ accounts for the uncertainty of the deployment location introduced by the GPS accuracy.

Using a similar analysis, Equation 7.6 represents the the maximum horizontal displacement d_{asc} , in m, of the FV from the surfacing location during the FV ascent.

$$d_{asc}(t_D) = \frac{v_{h,asc}}{100}(t_{surf} - t_D) + d_{asc,0}, \quad (7.6)$$

This distance information can be used in the HPPF framework to disregard particles that have exceeded these maximum displacements. First the particles are weighted based on their geomagnetic signature, as in Section 6.6.2. Then the particles are reweighed based on their horizontal distance from the deployment and surfacing locations. The distance $d_{i,dep}$ of the i th particle x_i from the deployment location can be calculated using Equation 7.7.

$$d_{i,dep}(t_D) = \sqrt{x_{i,1}(t_D)^2 + x_{i,2}(t_D)^2} \quad \text{for } 0 \leq t_D \leq t_{lnd}, \quad (7.7)$$

where $x_{i,1}(t_D)$ is the north coordinate of the i th particle, in the PCM coordinate frame, and $x_{i,2}(t_D)$ is its east coordinate.

Since all particles that satisfy $d_{i,dep} \leq d_{asc}$ are equally likely, the particle weights are updated using a uniform likelihood, Equation 7.8.

$$L(x_i(t_D)) = \begin{cases} \frac{1}{count(n)}, & \text{if } d_i \in n \\ 0, & \text{otherwise} \end{cases}, \quad (7.8)$$

where $n = \{d_{i,dep}(t_D) | d_{i,dep}(t_D) \leq d_{asc}(t_D)\}$, $count(n)$ is the number of elements in n and $0 \leq t_D \leq t_{ind}$.

During the ascent analysis, maximum horizontal displacements are calculated relative to the surfacing location. The distance $d_{i,surf}$ of the i th particle x_i with respect to the surfacing location can be estimated using Equation 7.9

$$d_{i,surf} = \sqrt{(x_{i,1}(t_D) - d_{north})^2 + (x_{i,2}(t_D) - d_{east})^2}, \quad (7.9)$$

where d_{north} is the north coordinate of the surfacing location, d_{east} is the east coordinate, and $t_{res} \leq t_D \leq t_{surf}$.

A similar analysis was applied to the ascend trajectory, where the weights of the particles are updated first based on geomagnetic data and secondly based on their relative distance from the recovery location using Equations 7.10.

$$L(x_1(t_D)) = \begin{cases} \frac{1}{count(m)}, & \text{if } d_i(t_D) \in m \\ 0, & \text{otherwise.} \end{cases}, \quad (7.10)$$

where $m = \{d_{i,surf}(t_D) | d_{i,surf}(t_D) \leq d_{asc}\}$, $count(m)$ is the number of elements in m and $t_{res} \leq t_D \leq t_{surf}$

If the maximum horizontal FV velocities are adequate and the deployment and surface locations are accurately recorded, then the maximum displacement constraint for both the descent and ascent analyses will form two intercepting circles at the ocean floor, as shown in Figure 7.51. The intersection lens represents the most likely landing area of the FV.

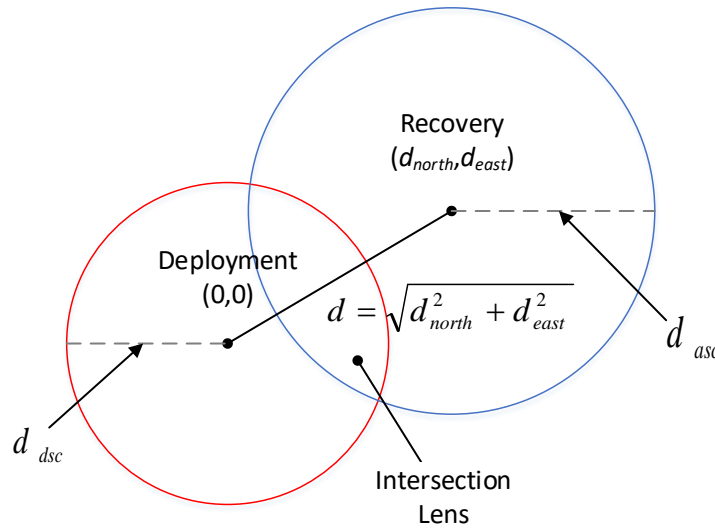


Figure 7.51 : Example interception lens of the PCM model, where d is total distance between the deployment and surfacing location.

The trajectory estimate of the HPPF was calculated by Selecting the particles from the ascent and descent analysis that landed in the intersection lens and averaging their trajectories. Figure 7.52 shows a plot of this solution for a simulated deployment of 1,000 m of depth using a navigation grade IMU and a magnetometer with a 1 nT measurement accuracy. Figure 7.53 is a plot of the ascent trajectory particles, in dark-lime, and the ascent trajectory particle, in purple, that landed inside the intersection lens. From Figure 7.53 it is possible to observe how the geomagnetic navigation algorithm and the PCM complement each other. Without the PCM, the estimates of the HPPF would drift, following the local isomagnetic lines (like in Section 7.2) but because of the PCM constraints the HPPF estimate are bounded. Also, if accurate geomagnetic data were available, the geomagnetic navigation would improve on the HPPF estimate, by keeping the particles close to the local isomagnetic line. Figure 7.54 plots of the difference between simulated FV trajectory and the HPPF estimate trajectory. Overall the navigation errors are kept within 50 m for the whole simulated deployment.

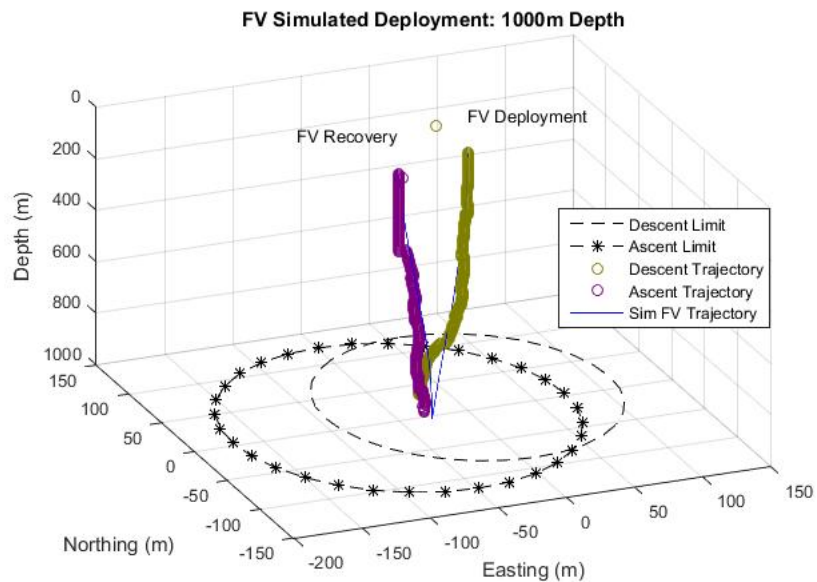


Figure 7.52 : Plot of the HPPF trajectory estimates using the PCM for a simulated FV deployment at 1,000 of depth. The ascend trajectory estimate is in dark-lime and the descent trajectory estimate is in purple.

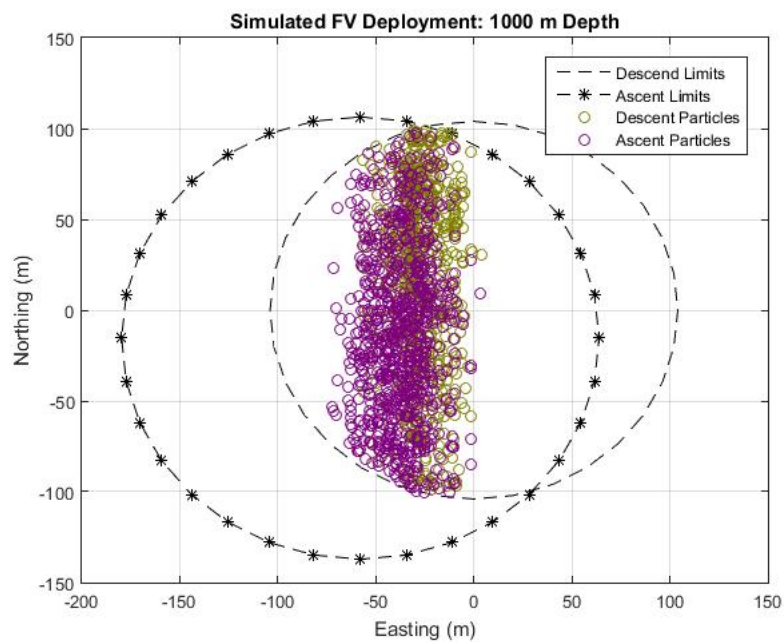


Figure 7.53 : Plot of the intersection lens and particle from trajectory analysis that landed inside the lens. Particles from the descent analysis are plotted in dark-lime and the particles from the ascent in purple.

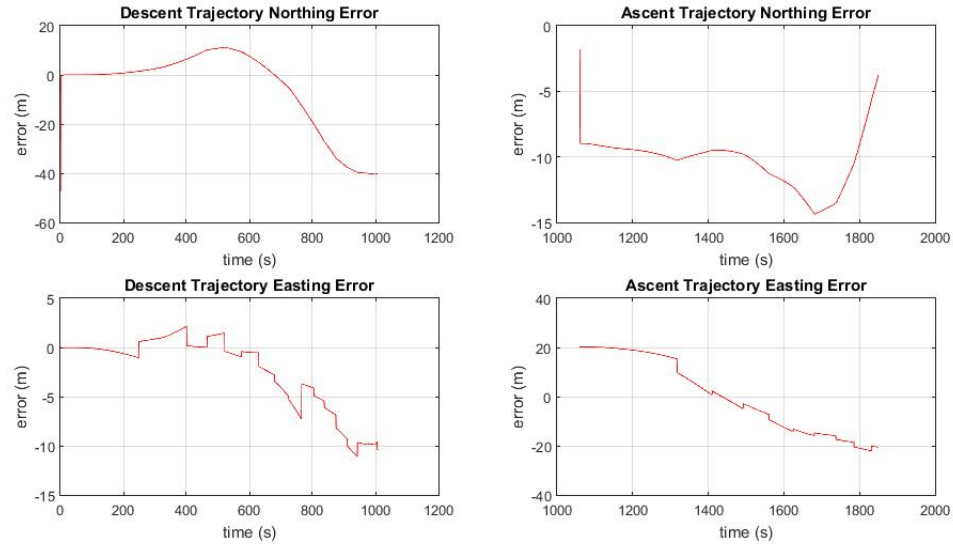


Figure 7.54 : Plot of HPPF estimate error for the 1000 m depth simulated deployment.

Figure 7.55 shows an updated system diagram of the postprocessing navigation system with the addition of the PCM. It is important to note that this solution does not provide a continuous position solution for the FV, since both landing locations, from the descent and ascent analysis, most likely would not match. Instead this strategy provides a set of potential FV trajectories based on geomagnetic information and physical horizontal dynamics of the FV. Also, due to the re-sampling nature of the particles filter that not all, if any, of the particle that landed in the intersection area might have followed a physically feasible trajectory. The behavior of each particle's trajectory will depend on the INS sensor grade used for the deployment, the lower the grade of the IMU the higher the re-sampling rate.

7.4.2 HPPF Test with Simulated Data

This section presents the results from a series of tests performed on different configurations of the HPPF, using the PCM and simulated data sets. The objective of these tests was to provide estimates of the HPPF horizontal position estimation performance under different filter configurations. All of the tests were performed on

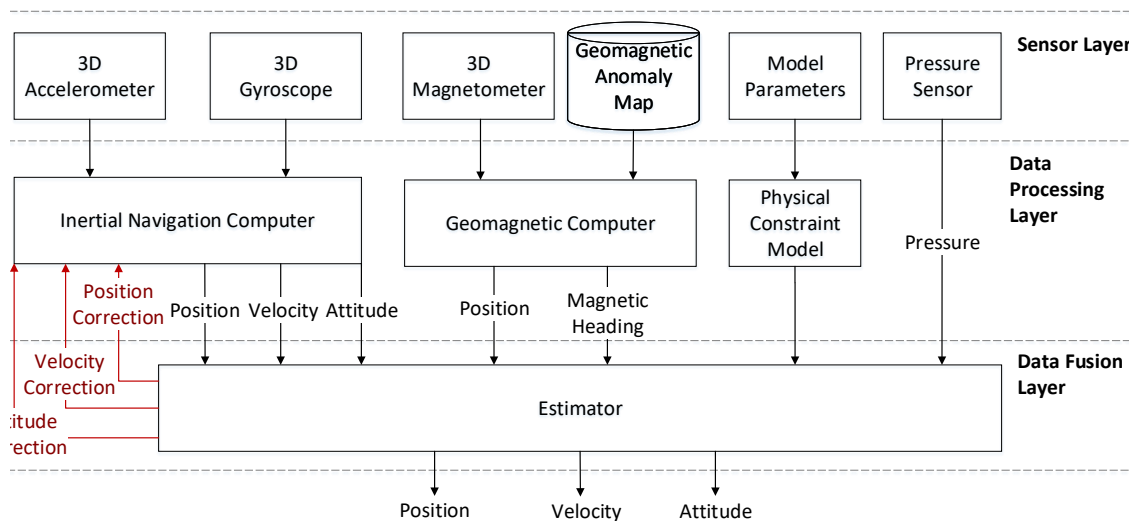


Figure 7.55 : Updated system diagram of the post-processing navigation system

the same simulated FV deployment at 4,000 m of depth, in Latitude 19.88N and Longitude 64.38W, with 5,000 filter particles. Figure 7.56 is a 3D plot of the simulated FV deployment. Figure 7.57 is a horizontal plot of the simulated FV trajectory with the boundaries of the PMC for the ascent trajectory, in black dashed line, and the ascent trajectory, in black dashed line with asterisks.

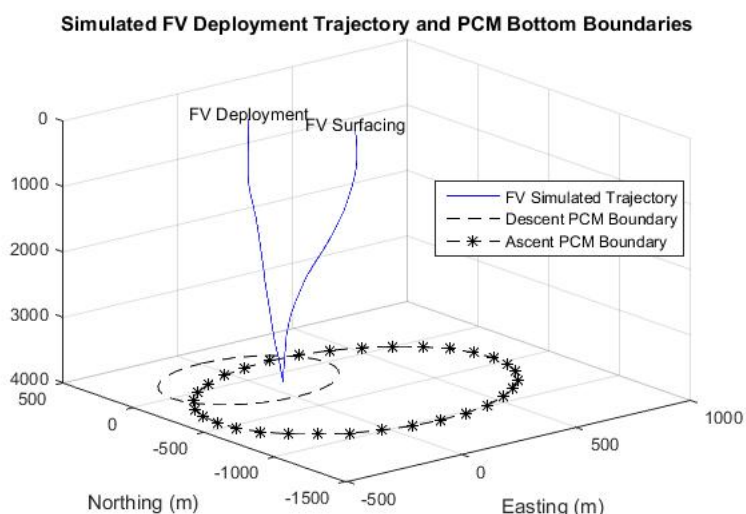


Figure 7.56 : Plot of the simulated FV deployment at 4000 m of depth, the origin of the coordinate frame is located at the deployment location.

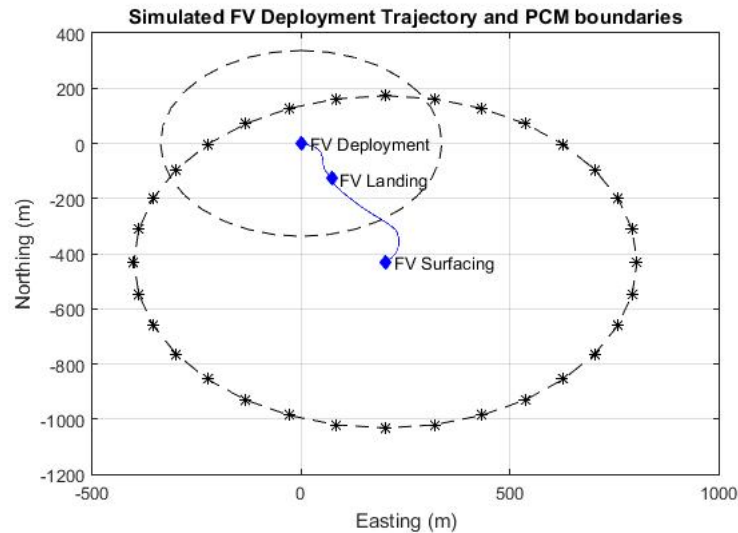


Figure 7.57 : A horizontal plot of the simulated FV deployment, with the boundaries of the PCM for the ascend trajectory, in black dashed line, and the ascend trajectory, in black dashed line with asterisk

The first simulated HPPF test used the parameters for a navigation-grade IMU and a magnetometer with 1 nT measurement accuracy. Figure 7.58 plots of the HPPF estimate trajectory, along with a plot of simulated FV trajectory. Figure 7.59 plots the particles from the ascent and descent analysis that landed inside the PCM intersection lens. Figure 7.60 are plots of the HPPF estimate error this test case. The error during the ascent analysis seems to peak at 430 m but this is most likely caused by the segmentation of the particles into two groups in the intersection lens. The segmentation of particle originated during a re-sampling phase of the HPPF, where two separate particles at the edge of the PCM boundaries were consistently inside the PCM boundaries and had favoring geomagnetic signatures. Overall the estimation errors were within 200m for the 8,070s of deployment. This is a significant navigation improvement from the previous HPPF implementation, which only relied on geomagnetic data. Note that particles around the local magnetic contour are favored more than those that are simply inside the physical limitation boundaries.

This is an example of the complimenting behavior of the PCM and geomagnetic data.

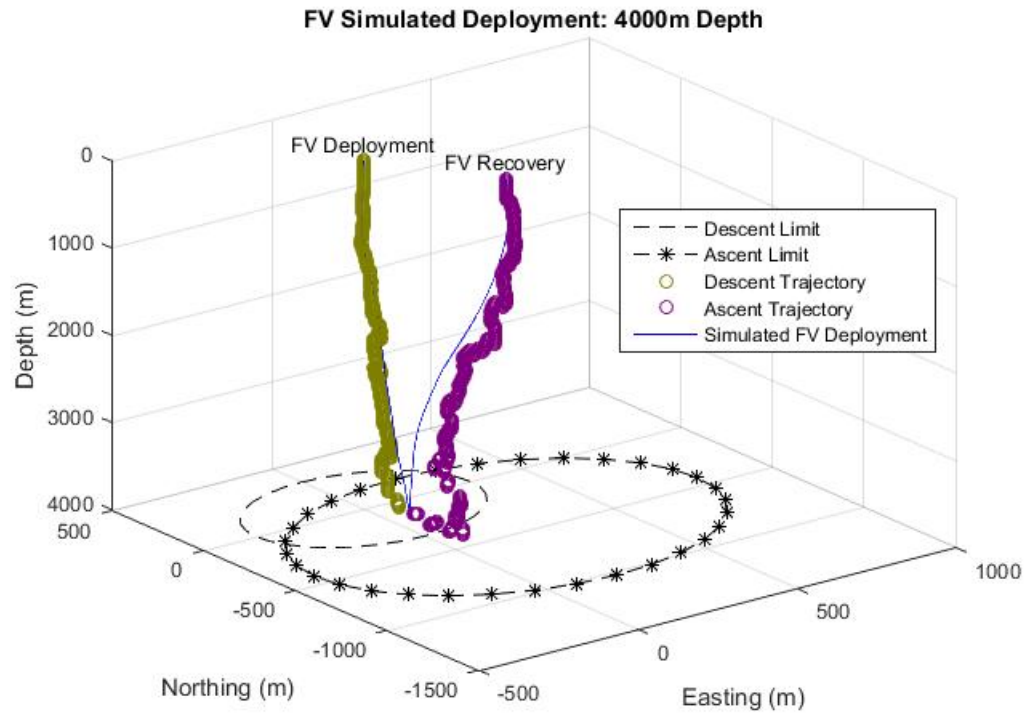


Figure 7.58 : A 3D plot of the HPPF estimated trajectory with the physically feasible measurement update, a navigation grade INS, and a magnetometer with 1 nT measurement accuracy. The descent trajectory is in dark lime and the descent is in purple.

The second simulated HPPF test used parameters for a tactical-grade IMU and a magnetometer with 10 nT measurement accuracy. Figure 7.61 plots the HPPF estimate trajectory, along with a plot of simulated FV trajectory. Figure 7.62 plots the particle from the ascent and descent analysis that landed inside the PMC intersection lens. Figure 7.63 are plots of the difference between the simulated FV trajectory and HPPF. From the Figures 7.61 and 7.62 it can be observed that with a geomagnetic measurement accuracy of 10 nT still offer navigational information which can complement the PCM. Errors from this simulation experiment are within

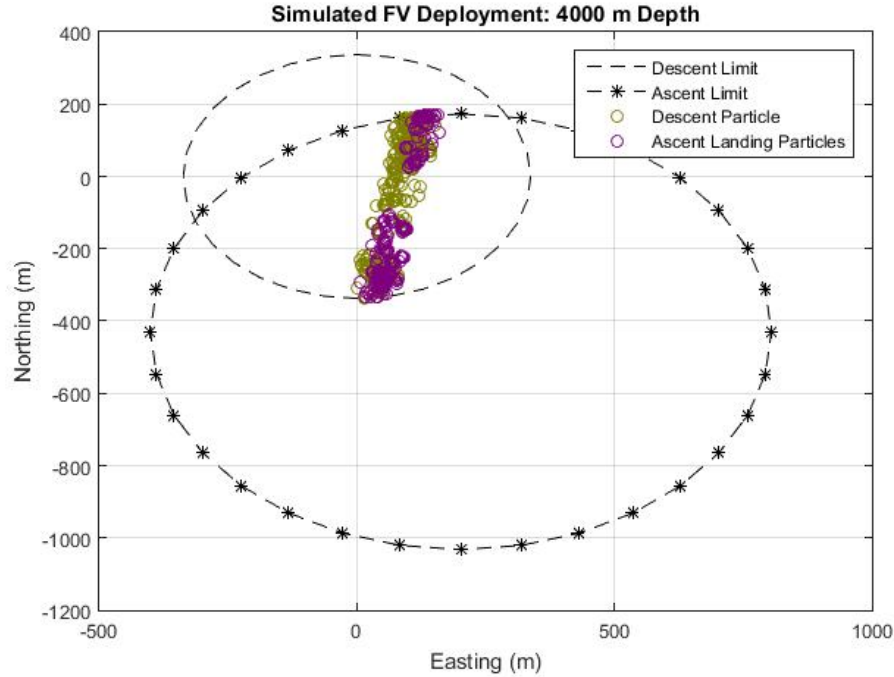


Figure 7.59 : A plot of the PCM boundaries and the particles from the ascent and descent analysis that landed inside.

300m. The apparent improvement over first test case is a result of a more uniform distribution of particles inside the intersection lens.

The third and final simulated HPPF test used commercial-grade IMU parameters and a magnetometer with 300 nT measurement accuracy, this is similar to the current configuration of the FV. In order to accommodate the degraded performance from a commercial-grade IMU an additional velocity constraint was applied to every HPPF estimate. If the HPPF estimate of horizontal velocity was larger than $v_{h,dsc}$ or $v_{h,asc}$, for the descent or ascent analysis, respectfully, then the estimate would be scaled to $v_{h,dsc}$ or $v_{h,asc}$ and the particle estimate of horizontal velocity, gyroscope bias and accelerometer bias would be reset. Figure 7.64 shows a 3D plot of the HPPF estimate trajectory. Figure 7.65 plots of the particle from the ascent and descent trajectory analysis that landed inside the PMC intersection lens. Figure 7.66 plots of the HPPF estimate error for the simulated deployment. From Figure 7.65 it is observable that

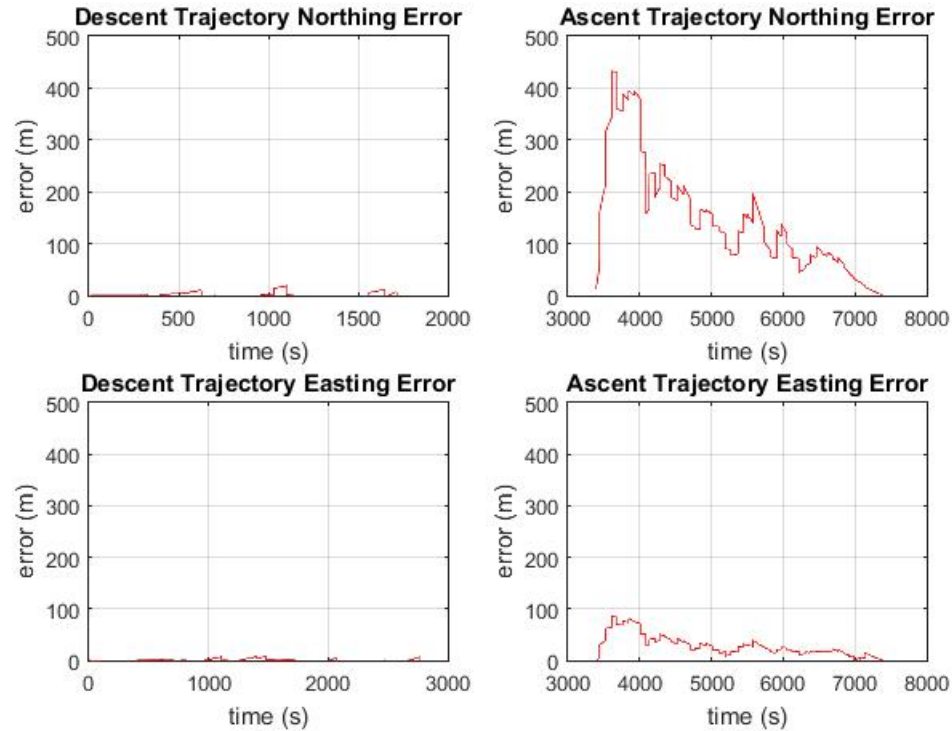


Figure 7.60 : Error plots from the HPPF estimate using the PCM, a navigation grade INS and a magnetometer with 1 nT measurement accuracy.

without accurate geomagnetic data, the HHP particles are allowed to spread freely within the boundaries of the PCM. The trajectory estimate and error plots show the effect of a commercial grade IMU on the HPPF. Because of the degraded IMU performance estimates from the HPPF have more noise. The increase in particle scatter due to the commercial grade IMU can also cause curving artifacts on the HPPF output trajectory. These artifacts are not unexplained since a commercial grade IMU model would cause increasing particle spread and as a result, increases the re-sampling rate of the HPPF which causes the curving artifacts. Even so, this is a significant improvement over the previous HPPF configuration which would only use the estimates from the commercial grade IMU to produce its estimate.

These simulation experiments of the HPPF provide insight to the expected navigation performance of the HPPF under different configurations. It also highlighted

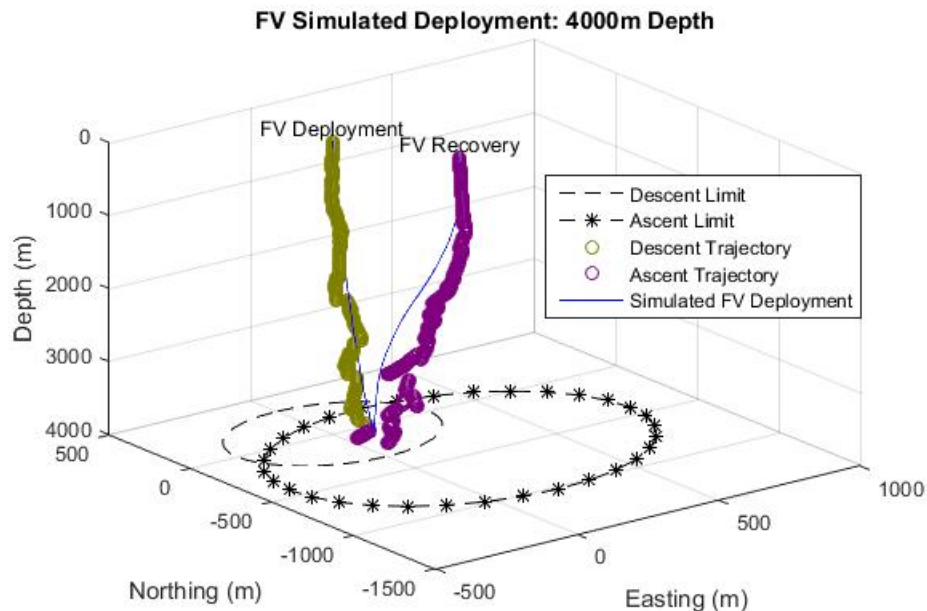


Figure 7.61 : A 3D plot of the HPPF estimated trajectory with the physically feasible measurement update, a navigation grade INS, and a magnetometer with 1 nT measurement accuracy. The descent trajectory is in dark lime and the ascent is in purple.

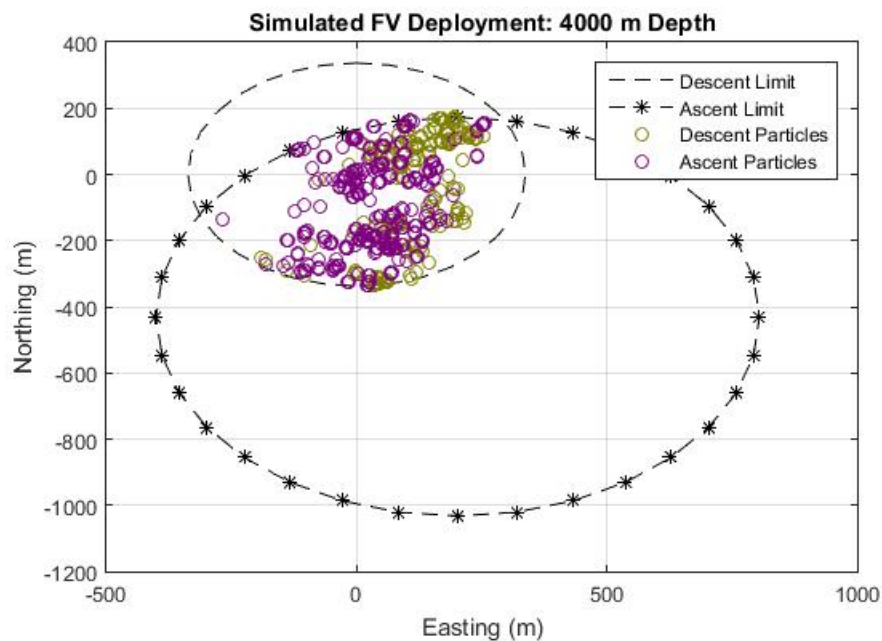


Figure 7.62 : A plot of the PCM boundaries and the particles from the ascent and descent analysis that landed inside.

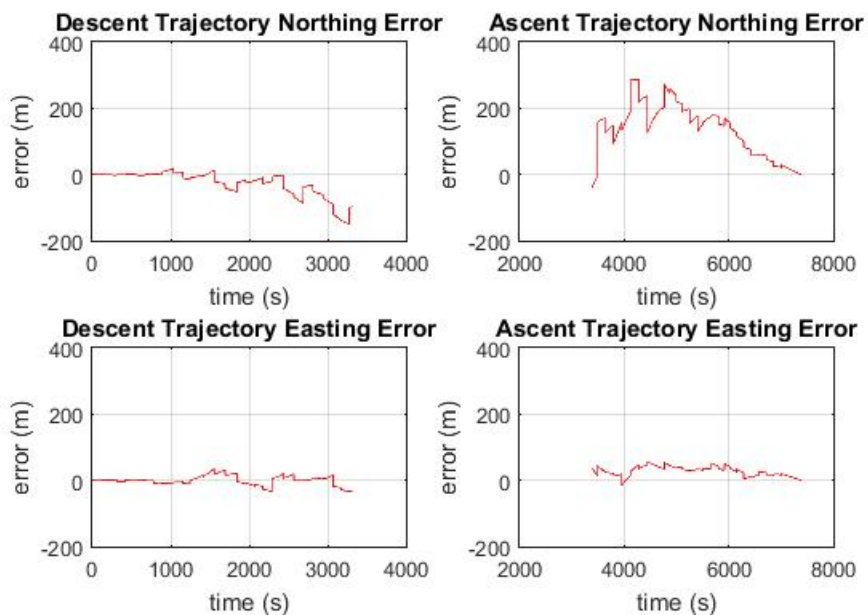


Figure 7.63 : Error plots from the HPPF estimate using the PCM, a tactical grade INS and a magnetometer with 10 nT measurement accuracy.

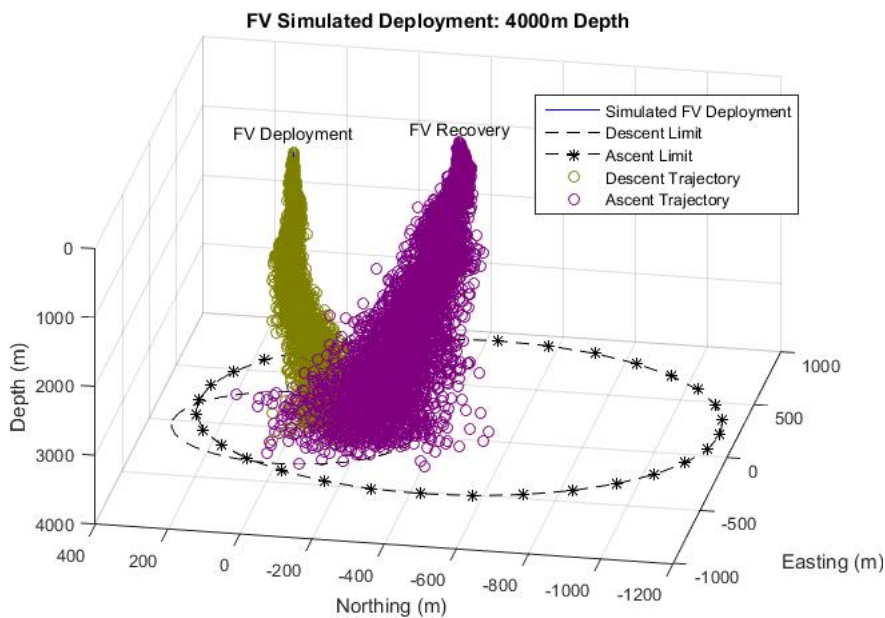


Figure 7.64 : A 3D plot of the HPPF estimated trajectory with the physically feasible measurement update, a commercial grade INS, and a magnetometer with 300 nT measurement accuracy. The descent trajectory is in dark lime and the ascent is in purple.

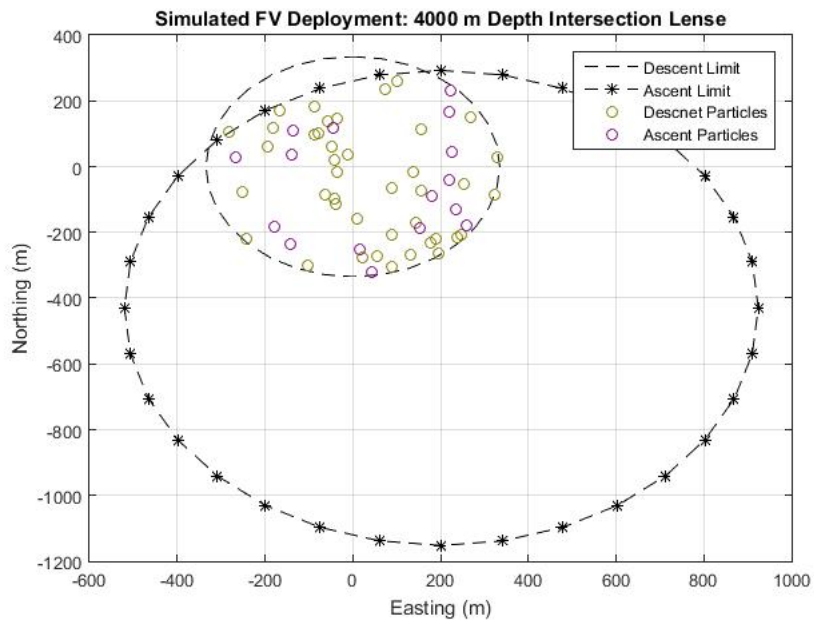


Figure 7.65 : A plot of the PCM boundaries and the particles from the ascent and descent analysis that landed inside.

the potential complimentary behavior between geomagnetic navigation information and the PCM.

7.4.3 HPPF Results and Analysis of Field Data

This subsection presents the HPPF estimates of five field deployment data sets. The Figure 7.67 plots the HPPF estimate trajectory and on bottom PCM boundaries for the 100 m depth FV deployment made on March 8, 2016. Figure 7.68 plots the HPPF estimate landing location for the descent and ascent analysis, in dark lime, and purple, respectively. Because the deployment and recovery locations were relatively close (within 15m), the trajectory estimates from the HPPF are almost vertical. The landing location estimate from the descent trajectory is 1 m west and 1 m north of the deployment location, with a standard deviation of 20 m. The landing estimate from the ascent trajectory is 0 m east and 1 m south of the deployment location, with at standard deviation of 21 m. It is worth noting that the descent and ascent

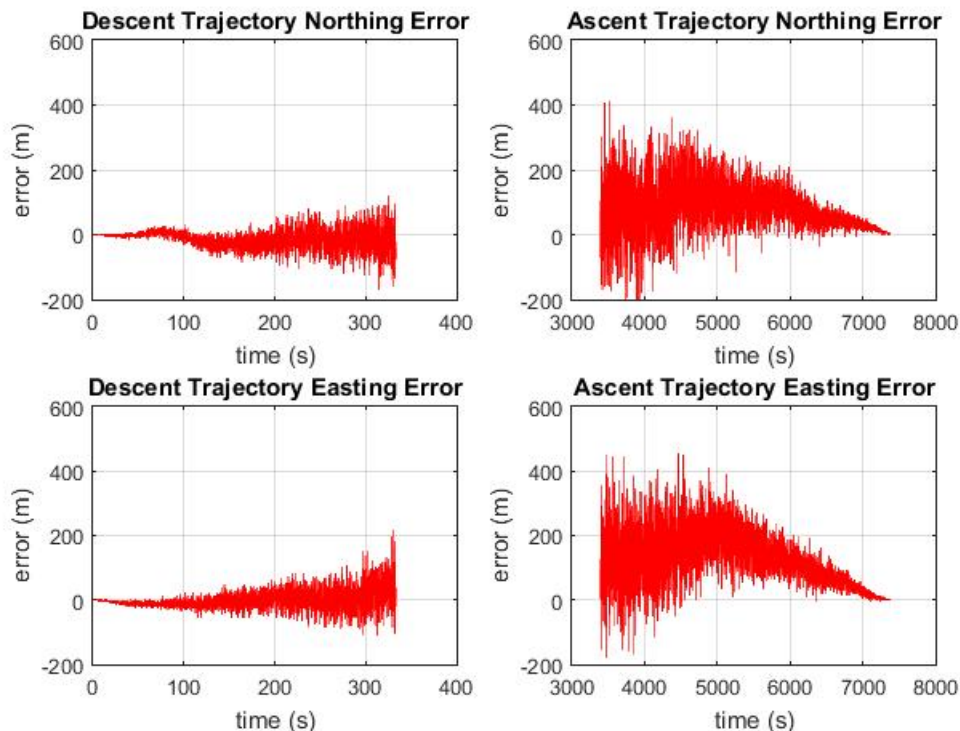


Figure 7.66 : Error plots from the HPPF estimate using the PCM, a commercial grade INS and a magnetometer with 300 nT measurement accuracy.

periods for this deployment were around 4 min, resulting in larger PCM boundaries and estimate standard deviations for both trajectories.

The larger descent and ascent periods could be caused by the safety line used to recover the FV in shallow deployments, like this one.

Figure 7.69 shows the HPPF estimate trajectory and on bottom PCM boundaries for the 1,000 m depth FV deployment made on March 8, 2016. Figure 7.70 plots the HPPF estimate landing location for the descent and ascent analysis, in dark lime, and purple respectively. Similar to the results from the 100 m deployment, the HPPF estimate trajectories are almost vertical, due to the relative proximity between deployment and recovery locations. The FV did not have a safety line for this deployment and exhibited descent and ascent periods around 1,000 s. The estimate landing location from the descent analysis was 2 m west and 0 m north from the deployment

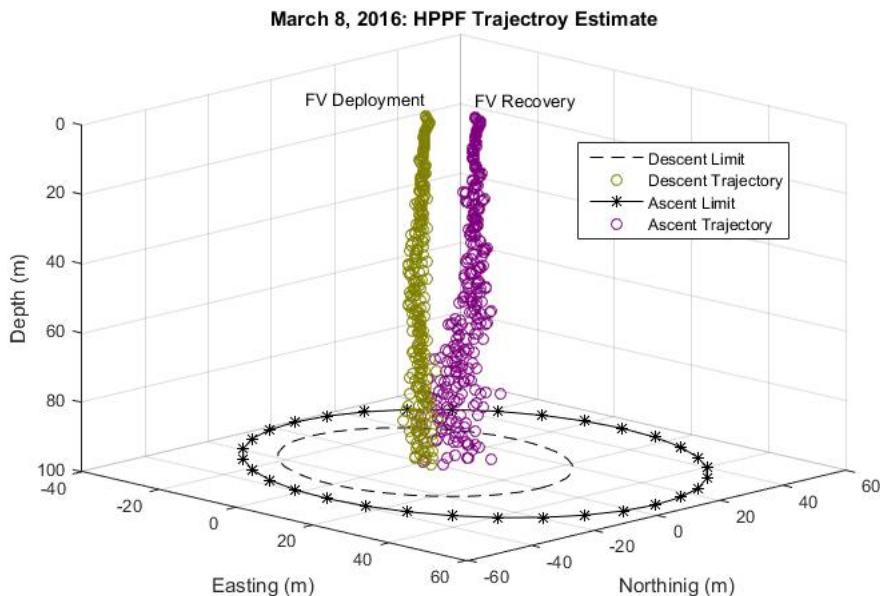


Figure 7.67 : Plot of the HPPF trajectory estimated for the 100 m FV deployment on March 8, 2016. The dark lime plot is trajectory estimate for the descent analysis and the purple plot is for the ascent analysis

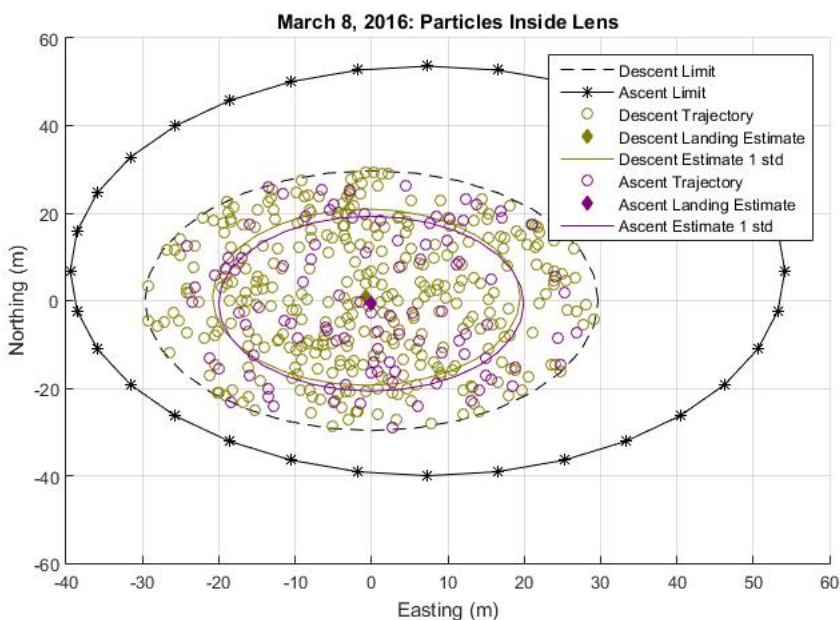


Figure 7.68 : Plot of the HPPF estimated landing location for the March 8, 2016 100 m deployment. The dark lime plots are for the descent trajectory, where the hollow circles are the particles inside the intersection lens and the diamond is their weighted average result. The same applies for the ascent analysis except the particles and their average is in purple.

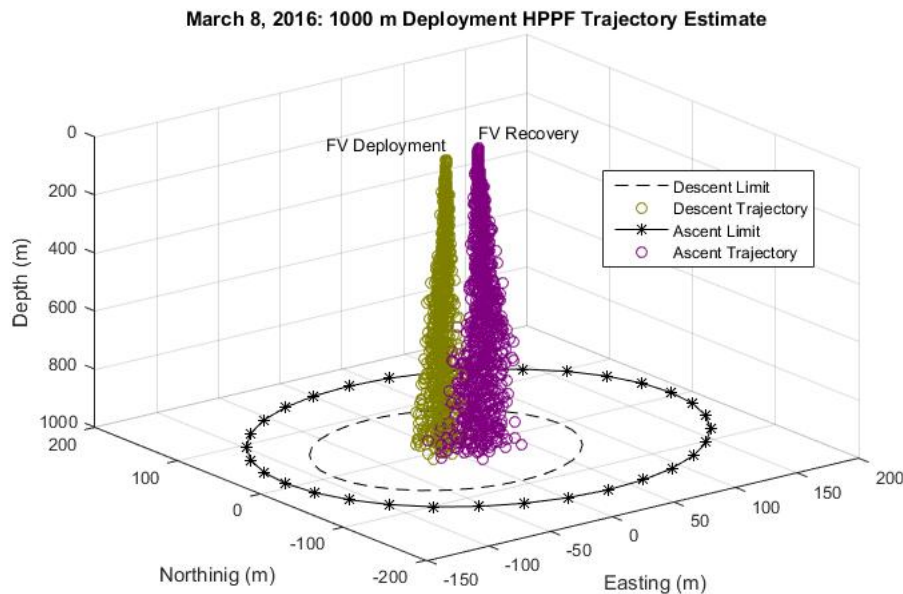


Figure 7.69 : Plot of the HPPF trajectory estimate for the 1,000 m FV deployment on March 8, 2016. The dark lime plot is trajectory estimate for the descent analysis and the purple plot is for the ascent analysis

location, with a standard deviation of 63 m. The estimate landing location from the ascent trajectory was 4 m west and 5 m south from the deployment location, with a standard deviation of 66 m.

Figure 7.71 plots of the HPPF estimate trajectories and on bottom PCM boundaries for 2,100 m depth FV deployment made on March 21, 2015. Figure 7.72 plots of the HPPF estimate landing location for the descent and ascent analysis, in dark lime, and purple respectively.

As expected, the trajectory estimates from the HPPF converge to the known deployment and recovery locations, and the uncertainty in its trajectory estimates increases with depth. The estimated landing location for the decent trajectory is 134 m east and 12 m south of the deployment location, with a standard deviation of 80 m.

The estimated landing location from the ascent trajectory is within 5 m of the descent landing estimate and has a standard deviation of 88 m.

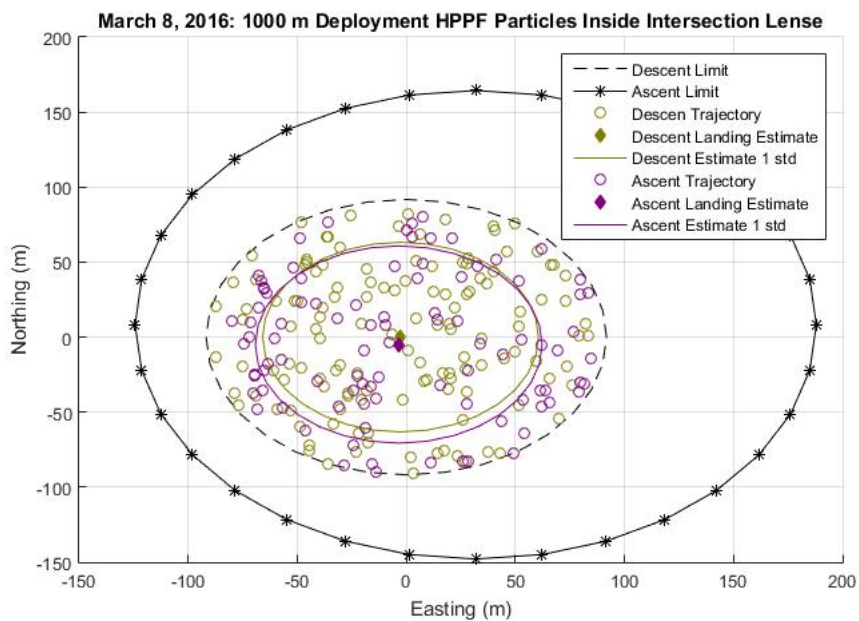


Figure 7.70 : Plot of the HPPF landing estimate for the 1000 m depth FV deployment on March 8, 2016. The dark line particle are for the descent trajectory, where the hollow circles are the particles inside the intersection lens and the diamond is their weighted average result. The same applied for the ascent analysis except the particles and their average is in violet.

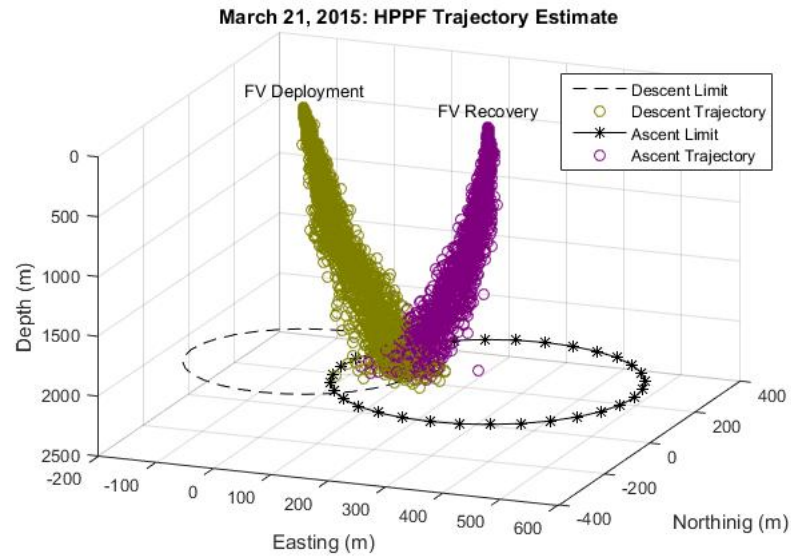


Figure 7.71 : Plot of the HPPF trajectory estimated for the 2100 m depth FV deployment on March 21, 2015. The descent trajectory estimate is in dark-lime and the ascent trajectory is in purple.

Since the particles from the ascent and descent trajectory estimates are spread uniformly inside the intersection lens, both landing estimates converge to the center of the lens and have similar standard deviation.

Figure 7.73 shows the HPPF trajectory estimate for the 8,300 m depth FV deployment made on March 30, 2015, along with on bottom PCM boundaries. Figure 7.74 plots the HPPF estimate landing location for the descent and ascent analysis, in dark lime, and purple respectively. For this deployment, the FV configuration used one glass sphere instead of two, the same configuration used in the deployment of April 1, 2015. In this configuration the FV is expected to exhibit more hydrodynamic instability during the ascent. For this reason, the hydrodynamic instability estimate, in 7.4, was doubled from 10 cm/s to 20 cm/s, for total maximum horizontal ascent horizontal velocity of 25 cm/s.

As mentioned in Subsection 7.4.2, due to the quick spread of HPPF particles caused by the commercial grade IMU parameters, might exhibit curving artifacts in the HPPF trajectory estimate. The FV was recovered 2,784 m from the deployment

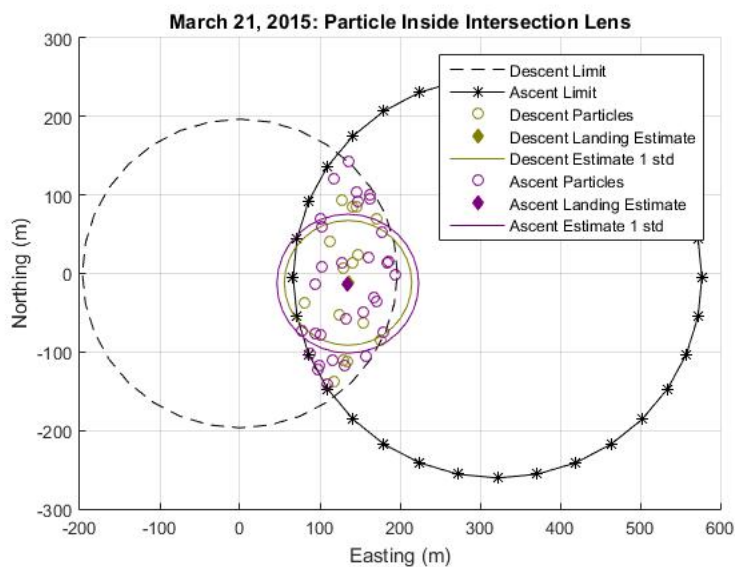


Figure 7.72 : Plot of the HPPF landing estimates for the deployment on March 21, 2015. The dark lime particle are for the descent trajectory, where the hollow circles are the particles inside the intersection lens and the diamond is their weighted average result. The same applies for the ascent analysis except the particles and their average are plotted in purple.

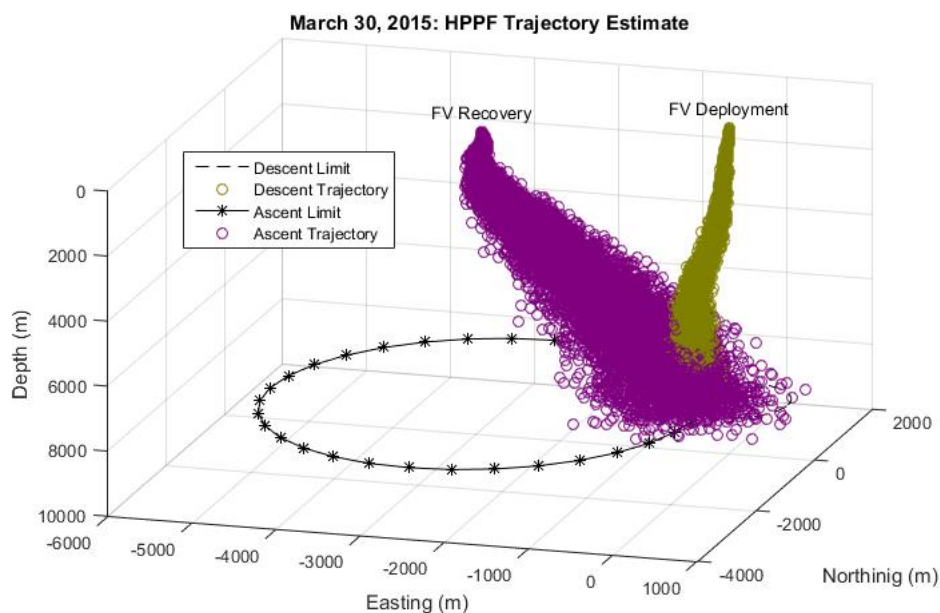


Figure 7.73 : Plot of the HPPF trajectory estimate for the 8,300 m depth deployment on March 30, 2015. The dark line plot is trajectory estimate for the descent path and the purple plot is for the ascent trajectory

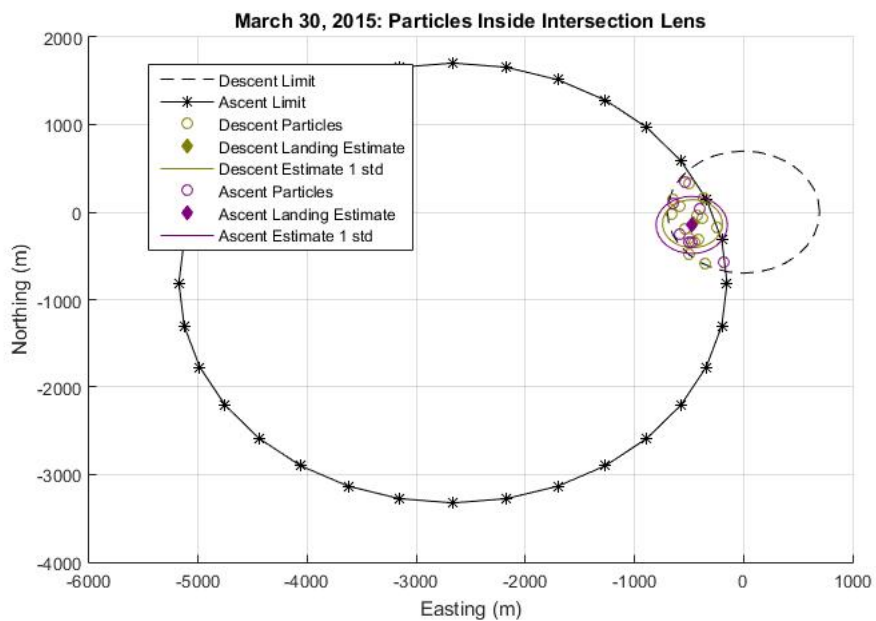


Figure 7.74 : Plot of the HPPF landing estimate for the deployment on March 30, 2015. The dark lime particle are for the descent trajectory, where the hollow circles are the particles inside the intersection lens and the diamond is their weighted average result. The same applied for the ascent analysis except the particles and their average is in violet.

location, 2,664 m west and 810 m south. The estimate landing location from the descent analysis is 468 m west and 132 m south of the deployment location, with a standard deviation of 274 m. The landing estimate from the ascent analysis is 474 m west and 146 m south of the deployment location with a standard deviation of 327 m.

Figure 7.75 plots the HPPF estimate for the FV field deployment of April 1, 2015, at 8,373 m of depth. Figure 7.76 plots the HPPF estimate landing locations for the ascent and descent trajectories along with the intersection lens formed PCM boundaries. The FV was recovered 1,280 m from the deployment location, 1,220 m west and 400 m south. The analysis of the FV descent estimates the landing location 33 m west and 43 m south of the deployment location, with a 487 m std. The ascent trajectory analysis estimates the landing location at 143 m west and 54m south of the deployment location, with a 461 m std. The descent trajectory resulted mostly vertical because the constraints for the analysis ended inside the constraints of the ascent. The ascent trajectory estimate exhibit some curving artifacts, these are the product of the relatively large constricting PCM boundaries and the high scatter of the particles from the commercial grade IMU model. Note that the simulated deployment with commercial grade sensors models, in Subsection 7.4.2, exhibit some similar behavior in estimation performance for this deployment and the deployment of March 2015.

7.4.4 PCM Summary

In summary, the development of a physical constraint model for the HPPS was presented. The model was created to complement the current HPPF geomagnetic configuration by binding the filters estimate to what is physically feasible for an FV, from a hydrodynamic point of view. It was possible to observe how PCM and geomagnetic navigation algorithms complement each other, from the results from the simulated

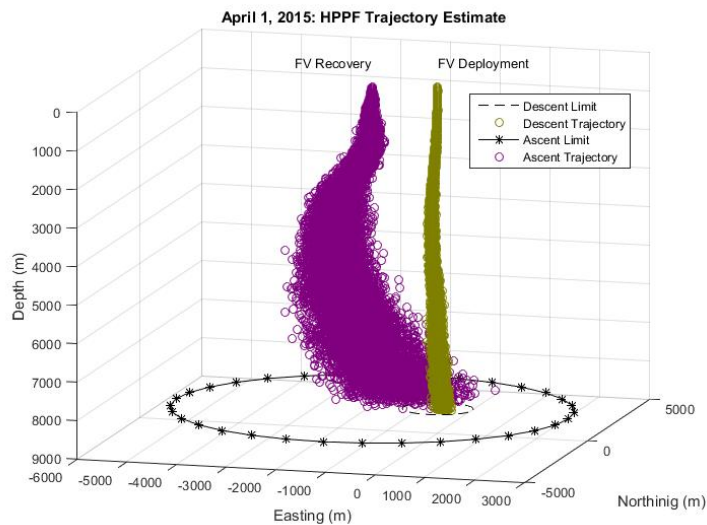


Figure 7.75 : Plot of the HPPF trajectory estimate for the 8,373 m depth deployment on April 1, 2015. The dark lime plot is trajectory estimate for the descent path and the purple plot is for the ascent trajectory

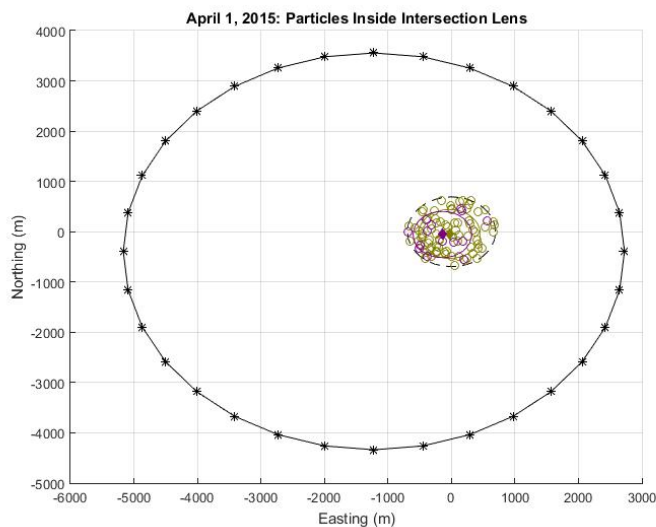


Figure 7.76 : Plot of the HPPF landing estimate for the deployment on April 1, 2015.

deployments. The PCM prevented drifts in HPPF estimates that caused by geomagnetic navigation algorithms following local isomagnetic. With accurate geomagnetic data, the geomagnetic algorithm favored regions inside the physical constraints which added more navigation information.

The trajectory and landing locations for five field deployments were analyzed. Although some trajectory estimates exhibited curving artifacts, these were the result of a high rate of HPPF particle re-sampling caused by the low accuracy of commercial-grade IMU model. The results of the field data also resembled the results from simulated deployment in Subsection 7.4.2. In short, the PCM provided a significant improvement on HPPF estimation performance regardless of the sensor performance grade.

7.5 Results and Analysis Summary

The results and analysis of the tests performed on an attitude complementary filter, a horizontal position particle filter HPPF, and a depth particle filter DPF were presented. The attitude complementary filter was found capable of estimating a system's attitude with respect to time, using a commercial, or better grade IMU. The attitude estimates demonstrated long-term stability with some oscillating errors due to the remaining biases in the IMU sensors.

The first HPPF configuration, with only geomagnetic-aided INS, was found to be inaccurate for the application of FV navigation, regardless of the sensor grade. This behaviour was attributed to the HPPF drifting estimates as the filter attempted to follow local isomagnetic lines. This analysis also concluded that the geomagnetic anomalies had to be sampled with at least 10 nT accuracy to be useful in geomagnetic navigation algorithms. A physically constraint model (PCM) was developed to complement the geomagnetic-aided INS scheme of the HPPF by limiting the particles within the physical limitations of the FV hydrodynamics. From the results of the simulated HPPF deployments, using the PCM, it was observed how the geomagnetic information could complement the PCM, provided accurate geomagnetic samples were obtained. The HPPF simulation also brought insight on the potential navigation performance of the HPPF under different sensor performance configurations. The HPPF was used to estimate the landing location and trajectory for five FV

field deployments. The result from these analyses behaved similarly to the simulated HPPF deployment using commercial grade sensors.

The DPF exhibited accurate estimates with either the FOGMPA or INS system models. The DPF was also found to be stable using the INS system model with navigation or tactical grade IMUs. The expected error from the dead reckoning estimates of a commercial IMU was too poor and caused instability in the DPF output. The FOGMPA model was found to offer little improvement over the depth estimates provided by the simulated pressure sensor. This was caused to by the broad range of estimated FV depth. An improved system model, that more accurately resembles the FV vertical dynamics, could be developed and tested at a next stage of the project.

In light of the results from all performed tests, the final sensor configuration of the FV post-processing navigation system was found to depends on the desired navigation performance and budget requirements. Potentially, the best navigation performance is achievable via a navigation-grade INS and a magnetometer with 10 nT measurement accuracy (or less). However a navigation-grade IMU can cost around \$100,000 [16] and accurate magnetometer can cost around \$20,000, which are considerably high when considering a low-cost FV. A low-cost solution could be archived using a calibrated commercial grade IMU however due to its low accuracy in geomagnetic operation it becomes necessary for it to be compliment by PCM in HPPF.

Chapter 8

Conclusions and Future Work

8.1 Conclusions

This research studied the foundation of inertial and geomagnetic navigation systems to develop a physically constraint geomagnetic navigation system. The system was composed of attitude, depth, and position estimators integrated in a post-processing framework that enables a low-cost implementation. The attitude estimator was based on a complementary filter framework. It was tested with simulated data sets and found capable of calculating the system's attitude with bounded error performance. The position estimator implemented a physically constrained geomagnetic matching navigation strategy, based on a particle filter framework. INS and FOGMPA system models were developed, as part of the particle filter's framework, to predict the system state. The position estimator was tested using both system models, in a simulated environment, and was used to analyze field data. The depth estimator of the system as developed, based on measurements from a pressure sensor, a particle filter framework and two system models (INS and FOGMPA). The depth estimator performed with satisfactory results when using both system models, although it proved to be unstable when using a commercial-grade IMU model.

In summary our findings indicate that is possible to develop a tarhecorey estimate using a comertia grade IMU however due to inherit resultion it needs to be complimente with a physically consrant model. If imporved navigation performace were disiraed we recomed using a higher grade IMU sensor and magnetomer.

8.2 Future Work

This research analyzed and explored several aspects of underwater geomagnetic navigation. While our approach produced feasible results, this research could be enhanced by making the following considerations:

- **Magnetometer Calibration:** calibrating the magnetometer before each deployment has the potential of improving its ability of detecting magnetic anomaly samples leading to improved geomagnetic navigation performance. There for the procedure of performing axis rotations and calibration strategies adequate for FV applications in a sea vessel shall be researched and developed.
- **Magnetic Anomaly Maps:** research on the usability of the EMAG map for navigation purposes shall be made. If no positional or correlation were possible via available EMAG or other available geomagnetic maps, then efforts should shift into the development of geomagnetic mapping schemes. This shall improve the geomagnetic algorithm's ability of correlating magnetic anomaly samples to positions on the map.
- **Magnetic Anomaly Field Downward Continuation:** as mentioned before in Chapter 2, the measured intensity of the geomagnetic anomaly field depends on the height above the local ground surface. Thus research efforts shall be made on downward continuation techniques which could be beneficial when using geomagnetic anomaly maps, made at ocean surface.
- **Research on FV hydrodynamics:** could lead to a more accurate and robust version of the physically constrained model. Such an improved model could enhance the estimation performance of the HPPF.
- **Adaptive Gain Complementary Attitude Filter:** research on adaptive gain strategies for the attitude complementary filter could improve the filter performance when the FV undergoes accelerations or is around perturbing magnetic sources. The HPPF could also improve its estimation performance from this enhancement.

Chapter 9

Contributions

The contribution of this research include:

1. A self-contained post-processing, physically constrained navigation system framework based on IMU data and pressure sensor, vehicle dynamics model and geomagnetic navigation strategies suitable for FV applications.
2. A simulation test framework composed of sensor models, deployment simulators and different system models suitable for testing and evaluating the performance characteristics of a navigation systems for FV applications.
3. Better insight on the potential navigation performance achievable by the developed navigation system under different system configurations.
4. A flexible navigation solution, it is possible to accommodate the current navigation solution to use other sources of navigation information with few changes to the overall framework. The developed navigation system can also be adapted for other underwater positioning application, with few additional development.
5. Knowledge on how the almost stationary state of FVs and their expected motion dynamics effect navigation strategies, like INS.

Bibliography

- [1] David Titterton and John L Weston. *Strapdown inertial navigation technology*, volume 17. IET, 2004.
- [2] K Großekatthöfer and Z Yoon. Introduction into quaternions for spacecraft attitude representation. Technical report, Technical University of Berlin, 2012.
- [3] Roberto G Valenti, Ivan Dryanovski, and Jizhong Xiao. Keeping a good attitude: A quaternion-based orientation filter for imu and margs. *Sensors*, 15(8):19302–19330, 2015.
- [4] Vernon Chi. Quaternions and rotations in 3d-space: How it works. Technical report, University of North Carolina at Chapel Hill, 1998.
- [5] Oliver J Woodman. An introduction to inertial navigation. *University of Cambridge, Computer Laboratory, Tech. Rep. UCAMCL-TR-696*, 14:15, 2007.
- [6] Oyvind Hegrehaes, Einar Berglund, and Oddvar Hallingstad. Model-aided inertial navigation for underwater vehicles. In *Robotics and Automation, 2008. ICRA 2008. IEEE International Conference on*, pages 1069–1076. IEEE, 2008.
- [7] Luke Stutters, Honghai Liu, Carl Tiltman, and David J Brown. Navigation technologies for autonomous underwater vehicles. *Systems, Man, and Cybernetics, Part C: Applications and Reviews, IEEE Transactions on*, 38(4):581–589, 2008.
- [8] James C Kinsey, Ryan M Eustice, and Louis L Whitcomb. A survey of underwater vehicle navigation: Recent advances and new challenges. In *IFAC Conference of Manoeuvring and Control of Marine Craft*, volume 88, 2006.
- [9] Ellyn T Montgomery and Kurt L Polzin. An integrated method of obtaining absolute ocean velocity from a profiling free vehicle. In *Current Measurement Technology, 2003. Proceedings of the IEEE/OES Seventh Working Conference on*, pages 227–230. IEEE, 2003.
- [10] Lynne D Talley. *Descriptive physical oceanography: an introduction*. Academic press, 2011.
- [11] Nicholas Paul Fofonoff and RC Millard Jr. *Algorithms for the computation of fundamental properties of seawater.*, volume 1. Unesco, 1983.

- [12] John Wright, Angela Colling, and Dave Park. *Waves, tides, and shallow-water processes*, volume 4. Gulf Professional Publishing, 1999.
- [13] Robert E Bicking. Features-fundamentals of pressure sensor technology. *Sensors-the Journal of Applied Sensing Technology*, 15(11):30–43, 1998.
- [14] Guo Caifa, Li Anliang, Cai Hong, and Yang Huabo. Algorithm for geomagnetic navigation and its validity evaluation. In *Computer Science and Automation Engineering (CSAE), 2011 IEEE International Conference on*, volume 1, pages 573–577. IEEE, 2011.
- [15] Felix Goldenberg. Geomagnetic navigation beyond the magnetic compass. In *Proceedings of IEEE/ION PLANS 2006*, pages 684–694, 2001.
- [16] Seamus Timothy Tuohy. Geophysical map representation, abstraction and interrogation for autonomous underwater vehicle navigation. Technical report, Massachusetts Institute of Technology, 1993.
- [17] Jianhu Zhao, Shengping Wang, and Aixue Wang. Study on underwater navigation system based on geomagnetic match technique. In *Electronic Measurement & Instruments, 2009. ICEMI'09. 9th International Conference on*, pages 3–255. IEEE, 2009.
- [18] Stefan Maus, Susan Macmillan, Susan McLean, Brian Hamilton, A Thomson, M Nair, and C Rollins. The us/uk world magnetic model for 2010-2015. 2010.
- [19] Ying Liu, Meiping Wu, Xiaoping Hu, and Hongwei Xie. Geomagnetism aided inertial navigation system. In *Systems and Control in Aerospace and Astronautics, 2008. ISSCAA 2008. 2nd International Symposium on*, pages 1–5. IEEE, 2008.
- [20] JF Vasconcelos, G Elkaim, C Silvestre, P Oliveira, and B Cardeira. Geometric approach to strapdown magnetometer calibration in sensor frame. *IEEE Transactions on Aerospace and Electronic Systems*, 47(2):1293–1306, 2011.
- [21] Yuanxin Wu and Wei Shi. On calibration of three-axis magnetometer. *IEEE Sensors Journal*, 15(11):6424–6431, 2015.
- [22] Benn Allen, Roger Stokey, Tom Austin, Ned Forrester, Rob Goldsborough, Mike Purcell, and Chris Von Alt. Remus: a small, low cost auv; system description, field trials and performance results. In *OCEANS'97. MTS/IEEE Conference Proceedings*, volume 2, pages 994–1000. IEEE, 1997.

- [23] James C Kinsey, David Smallwood, Louis L Whitcomb, et al. A new hydrodynamics test facility for uuv dynamics and control research. In *OCEANS 2003. Proceedings*, volume 1, pages 356–361. IEEE, 2003.
- [24] Bjørn Jalving, Kenneth Gade, Ove Kent Hagen, and Karstein Vestgard. A toolbox of aiding techniques for the hugin auv integrated inertial navigation system. In *OCEANS 2003. Proceedings*, volume 2, pages 1146–1153. IEEE, 2003.
- [25] Gabriel Grenon, P Edgar An, Samuel M Smith, and Anthony J Healey. Enhancement of the inertial navigation system for the morpheus autonomous underwater vehicles. *IEEE Journal of Oceanic Engineering*, 26(4):548–560, 2001.
- [26] Feizhou Zhang, Xiuwan Chen, Min Sun, Ming Yan, and Dongkai Yang. Simulation study of underwater passive navigation system based on gravity gradient. In *International Geoscience and Remote Sensing Symposium*, 2004.
- [27] Feng Haonan, Yang Zhaohua, and Fang Jiancheng. Simulation design of geomagnetic aided inertial navigation system. In *Systems and Control in Aerospace and Astronautics, 2008. ISSCAA 2008. 2nd International Symposium on*, pages 255–259. IEEE, 2008.
- [28] Zhixin Ren, Longwei Chen, Hui Zhang, and Meiping Wu. Research on geomagnetic-matching localization algorithm for unmanned underwater vehicles. In *Information and Automation, 2008. ICIA 2008. International Conference on*, pages 1025–1029. IEEE, 2008.
- [29] João Quintas, Francisco Curado Teixeira, and António Pascoal. Magnetic signal processing methods with application to geophysical navigation of marine robotic vehicles. In *OCEANS 2016 MTS/IEEE Monterey*, pages 1–8. IEEE, 2016.
- [30] Ying Liu, Meiping Wu, and Hongwei Xie. Iterative multi-level magnetic matching for uav navigation. In *Information and Automation (ICIA), 2010 IEEE International Conference on*, pages 1780–1783. IEEE, 2010.
- [31] Ying Liu, Meiping Wu, Xiaoping Hu, and Hongwei Xie. Research on geomagnetic matching method. In *Industrial Electronics and Applications, 2007. ICIEA 2007. 2nd IEEE Conference on*, pages 2707–2711. IEEE, 2007.
- [32] Kyle Kauffman and John Raquet. Navigation via h-field signature map correlation and ins integration. In *Radar Conference, 2014 IEEE*, pages 1390–1395. IEEE, 2014.
- [33] Mingyong Liu, Hong Li, and Kun Liu. Geomagnetic navigation of auv without a priori magnetic map. In *OCEANS 2014-TAIPEI*, pages 1–5. IEEE, 2014.

- [34] Francisco Curado Teixeira and António Pascoal. Magnetic navigation and tracking of underwater vehicles. *IFAC Proceedings Volumes*, 46(33):239–244, 2013.
- [35] Vladimir Djapic, Wenjie Dong, Adi Bulsara, and Greg Anderson. Challenges in underwater navigation: Exploring magnetic sensors anomaly sensing and navigation. In *Sensors Applications Symposium (SAS), 2015 IEEE*, pages 1–6. IEEE, 2015.
- [36] Manon Kok, Niklas Wahlström, Thomas B Schön, and Fredrik Gustafsson. Mems-based inertial navigation based on a magnetic field map. In *Acoustics, Speech and Signal Processing (ICASSP), 2013 IEEE International Conference on*, pages 6466–6470. IEEE, 2013.
- [37] You Li, Yuan Zhuang, Haiyu Lan, Peng Zhang, Xiaoji Niu, and Naser El-Sheimy. Self-contained indoor pedestrian navigation using smartphone sensors and magnetic features. *IEEE Sensors Journal*, 16(19):7173–7182, 2016.
- [38] Arno Solin, Simo Särkkä, Juho Kannala, and Esa Rahtu. Terrain navigation in the magnetic landscape: Particle filtering for indoor positioning. In *Navigation Conference (ENC), 2016 European*, pages 1–9. IEEE, 2016.
- [39] Daniel DiFrancesco, Andy Grierson, Dan Kaputa, and Thomas Meyer. Gravity gradiometer systems—advances and challenges. *Geophysical Prospecting*, 57(4):615–623, 2009.
- [40] Minoru Shinohara, Tomoaki Yamada, Toru Kanazawa, Kazutake Uehira, Hiroshi Fujimoto, Takuya Ishihara, Akito Araya, Kokichi Iizasa, and Satoshi Tsukioka. Development of an underwater gravimeter and the first observation by using autonomous underwater vehicle. In *Underwater Technology Symposium (UT), 2013 IEEE International*, pages 1–6. IEEE, 2013.
- [41] Juan Li, XinQian Bian, Xiaocheng Shi, and Zheng Qin. Simulation system of gravity aided navigation for autonomous underwater vehicle. In *Mechatronics and Automation, 2007. ICMA 2007. International Conference on*, pages 238–242. IEEE, 2007.
- [42] Christopher N Roman. *Self consistent bathymetric mapping from robotic vehicles in the deep ocean*. PhD thesis, Massachusetts Institute of Technology, 2005.
- [43] Ryan Eustice, Oscar Pizarro, and Hanumant Singh. Visually augmented navigation in an unstructured environment using a delayed state history. In *Robotics and Automation, 2004. Proceedings. ICRA'04. 2004 IEEE International Conference on*, volume 1, pages 25–32. IEEE, 2004.

- [44] O Hegrenses, Oddvar Hallingstad, and Bjørn Jalving. Comparison of mathematical models for the hugin 4500 auv based on experimental data. In *Underwater Technology and Workshop on Scientific Use of Submarine Cables and Related Technologies, 2007. Symposium on*, pages 558–567. IEEE, 2007.
- [45] Øyvind Hegrenæs and Oddvar Hallingstad. Model-aided ins with sea current estimation for robust underwater navigation. *Oceanic Engineering, IEEE Journal of*, 36(2):316–337, 2011.
- [46] Wilford E Schmidt and Eric Siegel. Free descent and on bottom adcm measurements in the puerto rico trench, 19.77° n, 67.40° w. *Deep Sea Research Part I: Oceanographic Research Papers*, 58(9):970–977, 2011.
- [47] Nelson G Hogg and Daniel E Frye. Performance of a new generation of acoustic current meters. *Journal of physical oceanography*, 37(2):148–161, 2007.
- [48] Alan D Chave. On the theory of electromagnetic induction in the earth by ocean currents. *Journal of Geophysical Research: Solid Earth (1978–2012)*, 88(B4):3531–3542, 1983.
- [49] Zoltan B Szuts. Using motionally-induced electric signals to indirectly measure ocean velocity: Instrumental and theoretical developments. *Progress in Oceanography*, 96(1):108–127, 2012.
- [50] Kenneth Gade. Navlab, a generic simulation and post-processing tool for navigation. *Modeling, identification and control*, 26(3):135, 2005.
- [51] Wilford Schmidt. Personal communication.
- [52] Warren Flenniken. *Modeling inertial measurement units and analyzing the effect of their errors in navigation applications*. PhD thesis, 2005.
- [53] Walter T Higgins. A comparison of complementary and kalman filtering. *IEEE Transactions on Aerospace and Electronic Systems*, (3):321–325, 1975.
- [54] Ken Shoemake. Animating rotation with quaternion curves. In *ACM SIGGRAPH computer graphics*, volume 19, pages 245–254. ACM, 1985.
- [55] Ioannis M Rekleitis. A particle filter tutorial for mobile robot localization. *Centre for Intelligent Machines, McGill University*, 3480, 2004.
- [56] Jeremiah A Shockley. Ground vehicle navigation using magnetic field variation. Technical report, DTIC Document, 2012.

- [57] Jun S Liu, Rong Chen, and Tanya Logvinenko. A theoretical framework for sequential importance sampling with resampling. In *Sequential Monte Carlo methods in practice*, pages 225–246. Springer, 2001.
- [58] Irma Shamatava, Gregory Schultz, and Fridon Shubitidze. Predicting earth magnetic anomalies from measured emag2 data. In *Direct and Inverse Problems of Electromagnetic and Acoustic Wave Theory (DIPED), 2016 XXIst International Seminar/Workshop on*, pages 127–130. IEEE, 2016.
- [59] Aaron Canciani and John Raquet. Airborne magnetic anomaly navigation. *IEEE Transactions on Aerospace and Electronic Systems*, 2017.
- [60] Stefan Maus, U Barckhausen, H Berkenbosch, N Bournas, J Brozena, V Childers, F Dostaler, JD Fairhead, C Finn, RRB Von Frese, et al. Emag2: A 2–arc min resolution earth magnetic anomaly grid compiled from satellite, airborne, and marine magnetic measurements. *Geochemistry, Geophysics, Geosystems*, 10(8), 2009.
- [61] Kyle Kauffman, John Raquet, Yu Morton, and Dmitriy Garmatyuk. Real-time uwb-ofdm radar-based navigation in unknown terrain. *IEEE Transactions on Aerospace and Electronic Systems*, 49(3):1453–1466, 2013.